UNIVERSITÀ
DI PAVIA

UNIVERSITÁ DEGLI STUDI DI PAVIA
Ph.D. School in Electronics, Computer Science and Electrical Engineering
Faculty of Engineering

THE VARIATIONAL MESHLESS METHOD FOR THE SOLUTION OF ELECTROMAGNETIC EIGENPROBLEMS

Doctoral Thesis of

Vincenzo LOMBARDI

Supervisor: Prof. Luca PERREGRINI

CYCLE XXXII
2016-2019

To my daughter, Cloe

Contents

Chapter 1

Introduction

The meshless method [1] is encountered in in various kind of applications. In particular it is used in the solution of mechanical problems [2], imaging [3], fluid dynamics [4], solution of partial differential equations in 2D [5, 6].

In the last decade this tool started to gain the attention also of the electromagnetic community and has been applied to various kind of problems such as time domain simulations [7, 8, 9, 10, 11, 12, 13], boundary problems [14], microwave imaging [15, 16, 17], and 2D bounded problems [18, 19, 20, 21, 22, 23].

The interest about the meshless method is increasing because this technique presents some advantages compared to the most traditional ones like finite element (FEM) or finite difference method [24]. The mesh generation is, in fact, a time and memory consuming process and this is unwanted in particular in real time simulations when frequent re-meshing steps are required. This is in particular true in the cases in which the basis functions are defined over triangular element pairs like the Rao-Wilton-Glisson (RWG) [25]. Another important feature of the meshless method is that it is based on a particular kind of basis functions (i.e. the radial basis functions) that can approximate the solution in a more accurate way than the low order polynomials used in the FEM [26].

In general the problems encountered in the microwave engineering can be divided in two families: those which bring to an inversion problem (e.g. imaging, inverse scattering, boundary problems) and those which bring to an eigenproblem (e.g. propagation inside a waveguide or resonant modes inside a cavity).

The aim of this thesis is the application of the meshless method to the second family. In particular various cases are taken into account: (1) the 2D scalar problem of finding the modes inside a shielded waveguide filled with an homogeneous material, (2) the 2D vector problem of finding the dispersion

diagram of the modes propagating inside a shielded waveguide filled with an inhomogeneous material, and (3) the 3D vector problem of finding the resonant modes inside shielded cavity filled with an inhomogeneous material.

However the meshless method presents some numerical limitations when is applied, in its original form, to the electromagnetic simulations that generate eigenproblems [19]. These limitations are, in brief, the low accuracy on the calculations of the first TE modes of a waveguide filled with a homogeneous material and the strong dependence of the solutions on the position of the collocation points [27], the non-symmetric nature of the built matrices that brings to the ill-conditioning of the problem [28, 29].

To overcome all these issues the variational technique has been applied in conjunction with the meshless method permitting to develop a new numerical tool that can handle all the cases listed before in a reliable way obtaining, in all the reported simulations, an high number of modes with a relative low number of unknowns.

This method has been called Variational Meshless Method (VMM).

This manuscript is organized as follows:

- Chapter 2 gives a brief introduction about the meshless method. In order to present this technique, the interpolation problem inside a bounded domain has been taken into account. Various considerations about the stability and the choice of the collocation points have been reported.

- Chapter 3 shows some limitations of the classical technique (such as the strong dependence of the solution on the position of the collocation points and the relative poor accuracy in the computation of the first TE modes of a waveguide) and proposes a very simple and no time consuming expedient which consists a slightingly different definition of the employed radial basis functions to improve the results.

- Chapter 4 presents the VMM for the 2D scalar problem of finding the eigenmodes inside an hollow waveguide shielded by a perfect conductor. it also proposes an automatic refinement technique which permits to handle also complicated geometries such as sharp corners.

- Chapter 5 presents the MM-VMM which is the mode matching technique in conjunction with the VMM and seems a promising technique for optimization problems.

- Chapter 6 presents the VMM for the 2D vector problem of finding the dispersion diagram of the modes inside an inhomogeneous waveguide shielded by a perfect conductor.
- Chapter 7 presents the exploitation of symmetries in the case of 2D vector problems.
- Chapter 8 presents the VMM for the 3D vector problem of finding the resonant modes inside an inhomogeneous cavity shielded by a perfect conductor.
- Chapter 9 gives some conclusions about this work.

All the numerical results reported in this manuscript are obtained on a computer with an Intel(R) Core(TM) i7-6700 CPU @ 3.40 GHz (8 CPUs), 3.4 GHz and 16 GB of RAM, by running a Matlab scripts.

All this activity is based on published works. A list of the publications updated at the moment of the submission of this manuscript is given in Appendix A.

Bibliography

[1] G. E. Fasshauer, *Meshfree approximation methods with MATLAB*, Vol. 6, Chicago,: CRC Press, 2003.

[2] G. R. Liu, *Meshfree methods: moving beyond the finite element method*, Boca Raton,: World Scientific, 2007.

[3] M. S. Tong and C. X. Yang, "A Meshless Method of Solving Inverse Scattering Problems for Imaging Dielectric Objects," *IEEE Trans. Geosci. Remote Sens*, Vol. 54, No. 2, pp. 990- 999, Feb. 2016.

[4] Y. Yang Y, S.B. Wen "A new high accuracy meshfree method to directly simulate fluid dynamics and heat transfer of weakly compressible fluids," *INT J HEAT MASS TRAN*, Vol. 123, No. 1, pp. 25-39, Aug.. 2018.

[5] R. B. Platte and T. A. Driscoll, "Computing eigenmodes of elliptic operators using radial basis functions," *Computers & mathematics with applications*, Vol. 48, No. 3, pp. 561-576, Mar./Apr. 2004.

[6] E. Larsson and B. Fornberg, "A numerical study of some radial basis function based solution methods for elliptic PDEs," *Computers & Mathematics with Applications*, Vol. 46, No. 5 pp. 891–902, Sep. 2003.

[7] Y. Yu and Z. Chen, "A 3-D radial point interpolation method for meshless time-domain modeling," *IEEE Trans. Microw. Theory Techn.*, Vol. 57, No. 8, pp. 2015–2020, Aug. 2009.

[8] Y. Yu and Z. Chen, "Towards the development of an unconditionally stable time-domain meshless method," *IEEE Trans. Microw. Theory Techn.*, Vol. 58, No. 3, pp. 578–586, Mar. 2010.

[9] S. Yang, Z. Chen, Y. Yu, and S. Ponomarenko, "A divergence free meshless method based on the vector basis function for transient electromagnetic analysis," *IEEE Trans. Microw. Theory Techn.*, Vol. 62, No. 7, pp. 1409–1415, Jul. 2014.

[10] S. Yang, Z. Chen, Y. Yu, and S. Ponomarenko, "On the numerical dispersion of the radial point interpolation meshless method," *IEEE Microw. Compon. Lett*, Vol. 24, No. 10, pp. 653–655, Oct. 2014

[11] T. Kaufmann, C. Fumeaux, and R. Vahldieck, "The meshless radial point interpolation method for time-domain electromagnetics," in *IEEE MTT-S Int. Microw. Symp. Dig.*, Atlanta, GA, 2008, pp. 61-64

[12] X. Chen, Z. Chen, Y. Yu, and D. Su, "An unconditionally stable radial point interpolation meshless method with Laguerre polynomials," *IEEE Trans. Antennas Propag.*, Vol. 59, No. 10, pp. 3756-3763, Oct. 2011.

[13] T. Kaufmann, C. Engström, C. Fumeaux, and R. Vahldieck, "Eigenvalue analysis and longtime stability of resonant structures for the meshless radial point interpolation method in time domain," *IEEE Trans. Microw. Theory Techn.*, Vol. 58, No. 12, pp. 3399–3408, Dec. 2010.

[14] J.-W. Lee and J.-T. Chen, "A semianalytical approach for a nonconfocal suspended strip in an elliptical waveguide," *IEEE Trans. Microw. Theory Techn.*, Vol. 60, No. 12, pp. 3642–3655, Dec. 2012.

[15] W. L. Nicomedes, R. C. Mesquita, and F. J. d. S. Moreira, ''The meshless local Petrov-Galerkin method in two-dimensional electromagnetic wave analysis," *IEEE Trans. Antennas Propag.*, Vol. 60, No. 4, pp. 1957-1968, Apr. 2012.

[16] M. S. Tong and W. C. Chew, "A novel meshless scheme for solving surface integral equations with flat integral domains," *IEEE Trans. Antennas Propag.*, Vol. 60, No. 7, pp. 3285-3293, Jul. 2012.

[17] A. Afsari and M. Movahhedi, "An adaptive radial point interpolation meshless method for simulation of electromagnetic and optical fields," *IEEE Trans. Magn.*, Vol. 50, No. 7, pp. 1–8, Jul. 2014.

[18] A. Afsari, A. M. Abbosh, and Y. Rahmat-Samii, "Modified Born iterative method in medical electromagnetic tomography using magnetic field fluctuation contrast source operator," *IEEE Trans. Microw. Theory Techn.* Vol. 67 , no. 1, pp. 454-463, Jan. 2019.

[19] S. J. Lai and B. Z. Wang, "Solving Helmholtz equation by meshless radial basis functions method," *Prog. Electromagn. Res. B*, Vol. 24, pp. 351–367, 2010.

[20] P. Kowalczyk and M. Mrozowski, "Mesh-free approach to Hemholtz equation based on radial basis functions," in *15th Int. Conf. Microwaves, Radar and Wireless Communications*, Vol. 2, No. 17-19, pp. 702–705, May 2004.

[21] T. Kaufmann, C. Engstrröm, and C. Fumeaux, "Characterization of an adaptive refinement algorithm for a meshless eigenvalue solver based on radial basis functions," in *IEEE Electromagn. Compat. Symp. (EMC)*, Melbourne, 2010.

[22] T. Kaufmann, C. Engstrröm, and C. Fumeaux, "Adaptive meshless methods in electromagnetic modeling: a gradient-based refinement strategy," in *41th European Microwave Conference (EuMC2011)*, Manchester, UK, Oct 12-14, 2011.

[23] J. Yu and H. Zhang, "Solving waveguide eigenvalue problem by using radial basis function method," in *IEEE World Automation Congress*, Hawaii, HI, 2008, pp. 1–5.

[24] M. N. O. Sadiku, *Numerical techniques in Electromagnetic*, 2nd ed., CRC press, 2011.

[25] S. M. Rao, D. R. Wilton, and A. W. Glisson, "Electromagnetic scattering by surfaces of arbitrary shape," *IEEE Trans. Antennas Propag.*, Vol. 30, No. 3, pp. 409–418, May 1982.

[26] J. M. Jin, *The Finite Element Method in Electromagnetics*, John Wiley & Sons, 2015.

[27] V. Lombardi, M. Bozzi, and L. Perregrini, "An Improved Meshless Method for Waveguide Eigenvalue Problems," Vol. 27, No. 12, pp. 1047–1049, Dec. 2017

[28] V. Lombardi, M. Bozzi, and L. Perregrini, "A novel variational meshless method with radial basis functions for waveguide eigenvalue problems," *IEEE Trans. Microw. Theory Techn.*, Vol. 66, No. 8, pp. 3714-3723, Aug. 2018

[29] J. H. Wilkinson, *The algebraic eigenvalue problem*, Vol. 87, Oxford: Clarendon Press, 1965.

Chapter 2

Meshfree Methods

2.1 Introduction

During the last decades the meshfree methods [1] have gained the attention of the scientific community. These powerful modeling tools can be applied in various kind of problems [2]:

- scattering data modeling
- the solution of partial differential equations
- non-uniform sampling
- mathematical finance
- computer graphics
- learning theory, neural networks and data mining
- optimization

All the listed applications depend on the ability of approximating a known or unknown function. For this reason most of the literature about the meshless methods is focused on the interpolation problems. This introductory chapter is therefore dedicated to the Scattered Data Interpolation Problem.

2.2 Scattered Data Interpolation Problem

The Scattered Data interpolation Problem is defined as follows[2]:

Scattered Data Interpolation *Given a data set* $(\boldsymbol{x}_j, y_j)$, $j = 1, \ldots, N$, *with* $\boldsymbol{x}_j \in \mathbb{R}^s$, $y_j \in \mathbb{R}$, *find a function* f *such that* $f(\boldsymbol{x}_j) = y_j$, $j = 1, \ldots, N$.

The basic idea beyond the meshfree methods is to approximate an unknown or known function f with a "similar" one which is called $\widetilde{f}$ through the linear combination of some particular basis functions each radial respect to their own center. The word "similar" will have a different meaning depending on the problem under study. These particular functions are defined in the following manner [3]:

Radial (Basis) Function *For a kernel* $\Phi : \mathbb{R}^s \times \mathbb{R}^s \to \mathbb{R}$ *with input vectors* $\boldsymbol{x}_j = [(x_j)_1, (x_j)_2, \ldots, (x_j)_s]^T$, $\boldsymbol{x}_i = [(x_i)_1, (x_i)_2, \ldots, (x_i)_s]^T$, *and a* $\phi(\cdot) : [0, \infty) \to \mathbb{R}$, Φ *is a radial (basis) function (RBF) if can be defined as* $\Phi(\boldsymbol{x}_j, \boldsymbol{x}_i) = \phi(r)$ *where* $r = \|\boldsymbol{x}_j - \boldsymbol{x}_i\|_2$ *is the Euclidean distance.*

The generic $\boldsymbol{x}_i$ vectors are called s-dimensional collocation points (CPs), while $\boldsymbol{x}_j$ are the observation points (OPs). Others norms can be used, but from now on in this work the Euclidean norm will only be considered.

The RBF-approximation $\widetilde{f}(\boldsymbol{x_j})$ of the generic function $f(\boldsymbol{x_j})$ can therefore be written as [3]

$$\widetilde{f}(\boldsymbol{x_j}) = \sum_{i=1}^{N} a_i \phi(\|\boldsymbol{x}_j - \boldsymbol{x}_i\|_2) \tag{2.1}$$

The interpolation problem is then built by imposing the Point Matching condition [8] resulting in a matrix linear problem:

$$\boldsymbol{A}\boldsymbol{a} = \boldsymbol{y} \tag{2.2}$$

where $\boldsymbol{a} = [a_1, a_2, \ldots, a_N]^T$ is the vector of the unknown coefficients, $\boldsymbol{y} = [y_1, y_2, \ldots, y_N]^T$ is the vector of the sampled values, $y_j = \widetilde{f}(\boldsymbol{x_j})$, and the interpolation matrix $\boldsymbol{A}$ has been introduced

$$\boldsymbol{A} = \begin{bmatrix} \phi(\|\boldsymbol{x}_1 - \boldsymbol{x}_1\|_2) & \ldots & \phi(\|\boldsymbol{x}_1 - \boldsymbol{x}_N\|_2) \\ \vdots & \ddots & \vdots \\ \phi(\|\boldsymbol{x}_N - \boldsymbol{x}_1\|_2) & \ldots & \phi(\|\boldsymbol{x}_N - \boldsymbol{x}_N\|_2) \end{bmatrix} \tag{2.3}$$

Note that if the CPs coincide with the OPs, $\{\boldsymbol{x}_j | j = 1 \ldots N\} = \{\boldsymbol{x}_i | i = 1 \ldots N\}$, the matrix $\boldsymbol{A}$ is symmetric. It is also real if we are dealing with real quantities. The interpolation will have thus a solution if the matrix $\boldsymbol{A}$ can be inverted. This can be guaranteed if $\boldsymbol{A}$ is a strictly positive defined matrix[2]

Table 2.1: Examples of SPD RBFs

Name	**Expression**
Gaussian	$\phi(r) = e^{-cr^2}$
Inverse Multi Quadratic	$\phi(r) = \frac{1}{\sqrt{1+cr^2}}$
C^0 Matérn	$\phi(r) = e^{-\sqrt{c}r}$
C^2 Matérn	$\phi(r) = e^{-\sqrt{c}r}(1+\sqrt{c}r)$
C^4 Matérn	$\phi(r) = e^{-\sqrt{c}r}(3+3\sqrt{c}r+cr^2)$
Truncated Power Function (if $\sqrt{c}r < 1$, 0 otherwise)	$\phi(r) = (1-\sqrt{c}r)_+^l$ where $l \geq \frac{s}{2}+1$

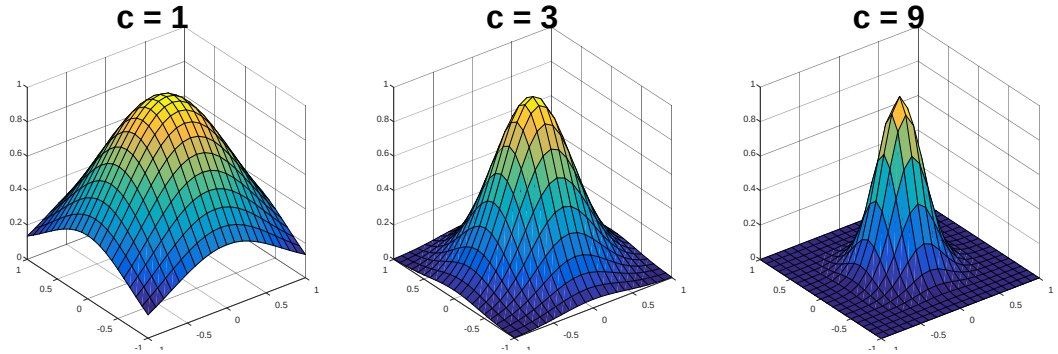

Figure 2.1: Plot of the Gaussian RBF for three different values of the shape parameter c.

Strictly Positive Defined Matrix *A real symmetric matrix* $\boldsymbol{A}$ *of dimension* $N \times N$ *is called strictly positive defined if for every non-zero vector* $\boldsymbol{c}$ *of dimension* $N \times 1$

$$\boldsymbol{c}^T \boldsymbol{A}\boldsymbol{c} > 0. \tag{2.4}$$

This depends on choice of an appropriate set of RBFs. The functions which permit to satisfy the (2.4) are called *strictly positive defined (SPD)* . There are kinds of SPD RBFs in the literature [2, 3, 5]. In Table 2.1 some examples are reported. Note that all the expressions reported depend on a value c that is called *shape parameter*. For high values of c the RBFs will be spiky, while for low values the function will be flatter. In Fig. 2.1 this effect is shown in the case of the Gaussian RBF. The choice of c is one of the most critical aspect of a meshless method since both the achievable precision and

the well conditioning of the problem (2.2) depend on it. Another important aspect that has effects on the precision and well-conditioning of (2.2) are the positions $\boldsymbol{x}_i$ and $\boldsymbol{x}_j$.

2.2.1 Considerations about the position of $\boldsymbol{x}_i$ and $\boldsymbol{x}_j$

Consider the general case in which the following interpolation has to be computed

$$\widetilde{g}(\boldsymbol{x}) = \sum_{i=1}^{N} b_i B_i(\boldsymbol{x}) \tag{2.5}$$

This is equivalent to a matrix problem $\boldsymbol{K}\boldsymbol{b} = \boldsymbol{g}$ where the B_i are called basis functions(not necessary radial). In this case the following definition can be given [2]:

Haar Space *Let the finite-dimensional linear function space $\mathcal{B} \subset \mathcal{C}(\mathbb{R}^s)$ have a basis $\{B_1, \ldots, B_N\}$. Then $\mathcal{B}$ in an **Haar Space** on $\mathbb{R}^s$ if*

$$det(\boldsymbol{K}) \neq 0 \tag{2.6}$$

for any distinct set of points $\boldsymbol{x}_1, \ldots, \boldsymbol{x}_N \in \mathbb{R}^s$. Here, $\boldsymbol{K}$ is the matrix with entries $K_{i,j} = B_j(\boldsymbol{x}_i)$.

The Mairhuber-Curtis theorem [6] states that it is not possible to fix in advance the set of basis functions to interpolate an arbitrary scattered data for multivariate problems($s \geq 2$). This is the reason why the polynomial interpolation is not suitable for large data set in multi-dimensional spaces.

To build a well-posed scattered interpolation problem, when dealing with RBFs, it is mandatory to find a set of RBFs that can guarantee the (2.6). We just know the answer: if the point matching technique is applied in conjunction with the SPD RBFs the problem is invertible and will have a unique solution. For this reason the natural choice for $\boldsymbol{x}_i$ will be the [7]

$$\textit{Point Matching Method: } \boldsymbol{x}_i = \boldsymbol{x}_j.$$

Depending on the problem to handle, the positions of the scattered data $\boldsymbol{x}_j$ could be given or eligible. In this last case some considerations can be made about both the *precision* and the *accuracy*.

In order to evaluate the error between the interpolant $\widetilde{f}(\boldsymbol{p}_j)$ and the data values $f(\boldsymbol{p}_j)$ on the evaluation points $\boldsymbol{p}_j$ with $j = 1, \ldots, P$, two measures can be used:

the *root-mean-square error* ($RMSE$)

$$RMSE := \sqrt{\frac{1}{P}\sum_{j=1}^{P}\left[\widetilde{f}(\boldsymbol{p}_j) - f(\boldsymbol{p}_j)\right]^2} = \frac{1}{\sqrt{P}}\|\widetilde{f} - f\|_2 \tag{2.7}$$

and the *sup norm* (i.e. the maximum value of the error)

$$\|\widetilde{f} - f\|_\infty := \sup_{x\in\mathbb{R}}(|\widetilde{f}(x) - f(x)|) \tag{2.8}$$

For special cases of infinitely smooth RBF such as Gaussian, the $RMSE$ can be estimated and some maximum bound can be found for this error [2]. In order to obtain this estimation the *fill distance* $h_{\chi,\Omega}$ can be used. It is defined as follows

$$h_{\chi,\Omega} = \sup_{\boldsymbol{x}\in\Omega}\min_{\boldsymbol{x}_i\in\chi}\|\boldsymbol{x} - \boldsymbol{x}_i\|_2 \tag{2.9}$$

where χ is the set of the CPs. Note that $h_{\chi,\Omega}$ indicates how well the data in fill out the domain Ω. A reasonable choice of the shape parameter c seems to be the *stationary approach* which consists in keeping constant the product $c\ h_{\chi\Omega}^2$ (see Table 2.1). This means that the shape parameter is chosen in order to respect the following thumb rule

$$c = \frac{c_0}{h_{\chi,\Omega}^2} \tag{2.10}$$

where c_0 is a proper constant. The convergence of the Gaussian RBF with respect to the pair c and $h_{\chi\Omega}$ has been studied by Madych in [8] and an analytical expression of the error bound has been given

$$|\widetilde{f}(\boldsymbol{x}) - f(\boldsymbol{x})| \leq C\lambda^{1/(\sqrt{c}h_{\chi,\Omega})} \tag{2.11}$$

where C is a proper constant value, while $\lambda < 1$. This relation is actually true provided that f is in the *Native Space* of the Gaussian Kernel. The Native space is defined as in [9]:

Native Space *If a symmetric strictly positive definite function* $\Phi : \Omega\times\Omega \to \mathbb{R}$ *is the reproducing kernel of a real Hilbert space* $\mathcal{H}$ *of real valued functions on* Ω*, then* $\mathcal{H}$ *is the native space for* Ω*.*

Thanks to (2.11) it is possible to state that, in the the case of the stationary approach (2.10), the error can be minimized by reducing $h_{\chi,\Omega}$. This is of

course intuitive, but do not help to define a "good" choice of $\boldsymbol{x}_j$. In order to achieve this result, another definition is needed.

The *separation distance* is

$$q_\chi = \frac{1}{2}\min_{i\neq j}\|\boldsymbol{x}_i - \boldsymbol{x}_j\|_2 \tag{2.12}$$

The problem (2.2) brings to the inversion of the matrix $\boldsymbol{A}$. It is well known in the literature [10] that the condition number of $\boldsymbol{A}$ respect to the inversion problem can be easily computed if the matrix is positive defined. In this case in fact

$$cond_2(\boldsymbol{A}) = \|\boldsymbol{A}\|_2\|\boldsymbol{A}^{-1}\|_2 = \frac{\lambda_{max}}{\lambda_{min}} \tag{2.13}$$

where λ_{max} and λ_{min} are respectively the maximum and minimum eigenvalue of $\boldsymbol{A}$. If, in (2.1) and (2.2), $\phi(\cdot)$ is positive defined the upper bound of λ_{max} is given by [11]

$$\lambda_{max} \leq N\phi(0) \tag{2.14}$$

while the lower bound of λ_{min} depends on the RBF in use. In the case of Gaussian RBFs it is possible to write [11]

$$\lambda_{min} \geq C_s(\sqrt{2c})^{-s}e^{-40.7s^2/cq_\chi^2}q_\chi^{-s} \tag{2.15}$$

where s is the dimension of the problem and C_s is a proper constant. As can be seen in (2.13) and (2.15), the conditioning of the problem (2.2) can be improved increasing q_χ. If c and $h_{\chi,\Omega}$ are thus fixed based on the considerations about the precision, q_χ must be kept as higher as possible [12].

For this reason, defining the *uniformity* as

$$\rho_{\chi,\Omega} = \frac{q_\chi}{h_{\chi,\Omega}} \tag{2.16}$$

the conditioning of the problem will be better when $\rho_{\chi,\Omega} \approx 1$ *i.e when the points are nearly equispaced.*

2.2.2 Considerations about the Shape Parameter and its choice

As said before, the choice of the shape parameter is critical in the meshless method. This is due to the fact that although the accuracy improves decreasing c, this value can not be arbitrarily small because of the stability

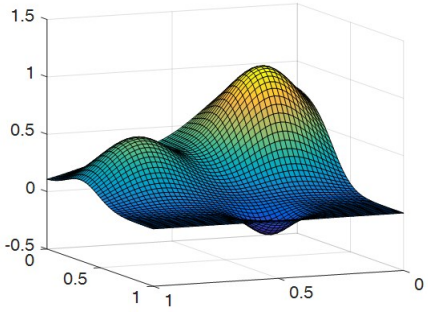

Figure 2.2: Plot of the Franke's function over the unit square.

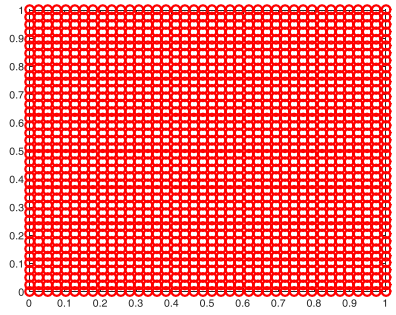

Figure 2.3: Evaluation points used to calculate the error of the interpolation of the Franke's function in the cases under study.

of the numerical computation. In order to study this effect, consider the interpolation, inside the domain $[0,1] \times [0,1]$, of the Franke's function [13]

$$\begin{aligned} f(x,y) = &+ \frac{3}{4} e^{-1/4((9x-2)^2+(9y-2)^2)} + \frac{3}{4} e^{-(1/49)(9x+1)^2-(1/10)(9y+1)^2} \\ &+ \frac{1}{2} e^{-1/4((9x-7)^2+(9y-3)^2)} - \frac{1}{5} e^{-(9x-4)^2-(9y-7)^2} \end{aligned} \tag{2.17}$$

The graph of this function is shown in Fig. 2.2. The interpolation performances are evaluated in the case of 81, 289, and 1089 CPs. While the $RMSE$ and the maximum error are calculated over the grid consisting of 1600 evaluation points $\boldsymbol{p}_j$ shown in Fig. 2.3 (see (2.7) and (2.8)). Calling the floating-point relative accuracy used by Matlab *eps*, the CPs, the $RMSE$ and maximum error, and the condition number of the interpolation matrix $\boldsymbol{A}$ compared to a arbitrary threshold of $1/(10\ eps)$ are shown for the case of 81, 289, and 1081 CPs respectively in Fig. 2.4, Fig. 2.5, and Fig. 2.6.

In Tab. 2.2, the best scenarios with respect to the $RMSE$, using Gaussian RBFs, are reported.

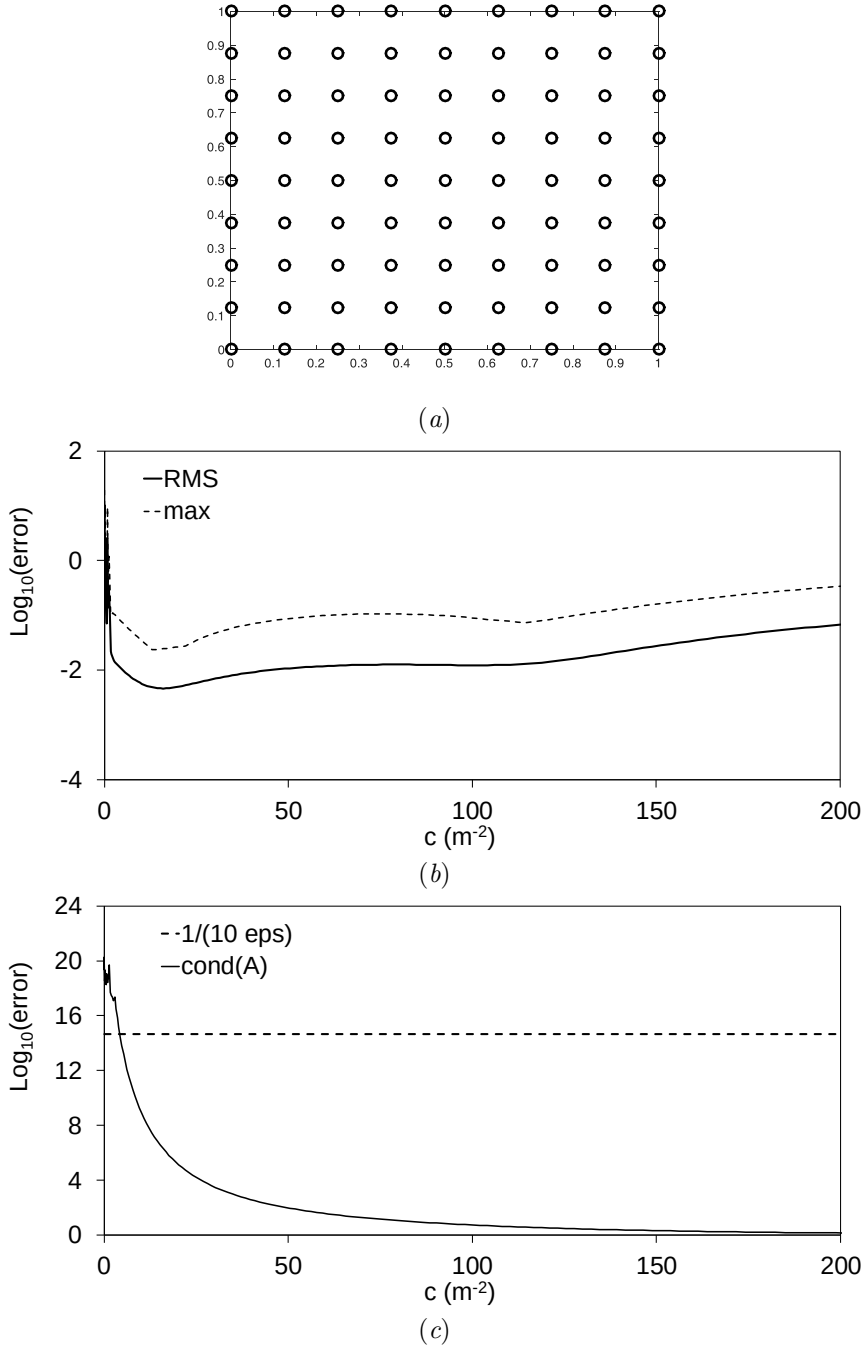

Figure 2.4: Interpolation of the Franke's function with 81 CPs: (a) CPs. (b) $RMSE$ and max error; (c) condition number of the interpolation matrix $\boldsymbol{A}$ compared with $1/(10\ eps)$.

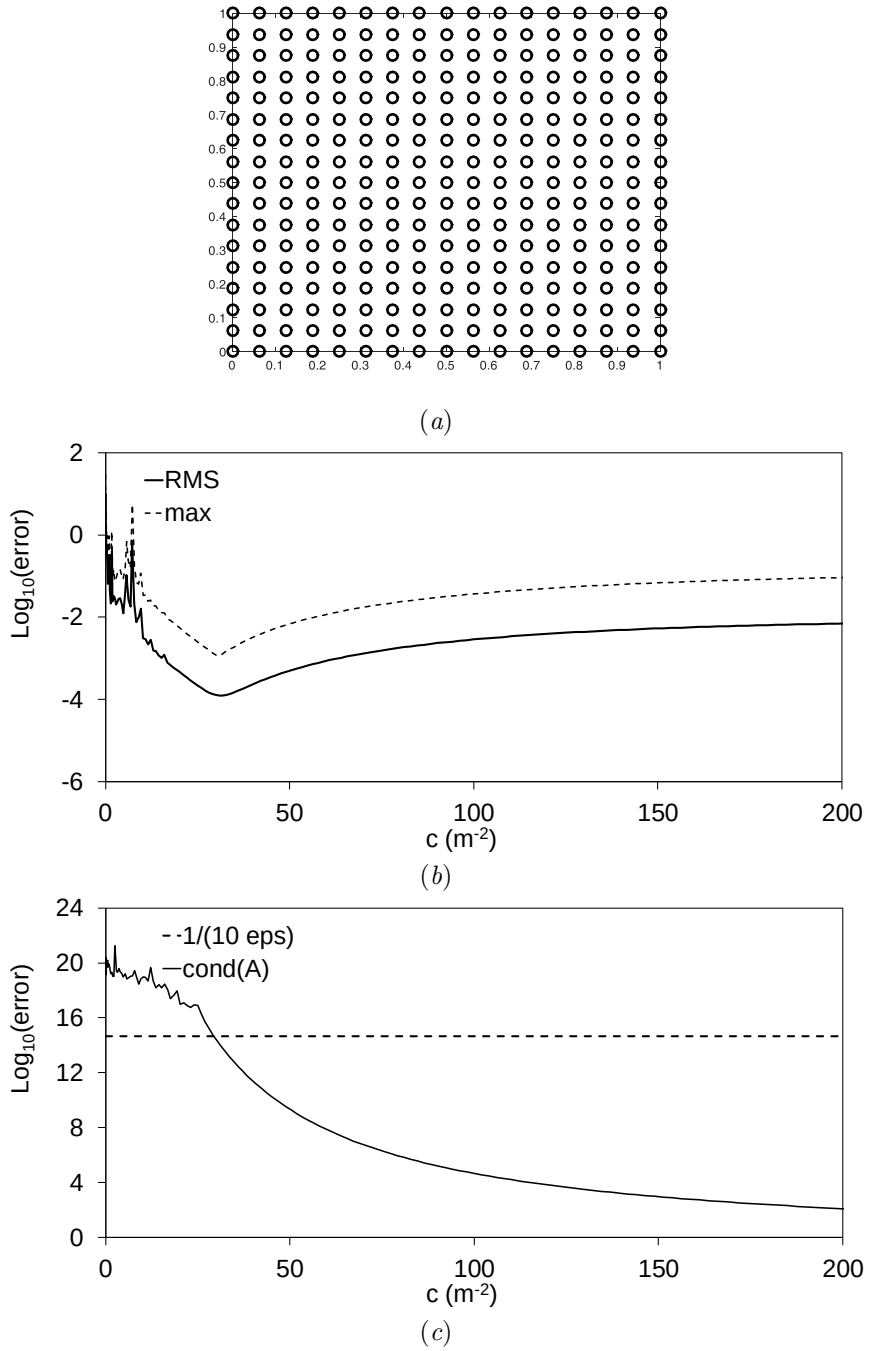

Figure 2.5: Interpolation of the Franke's function with 289 CPs: (a) CPs. (b) $RMSE$ and max error; (c) condition number of the interpolation matrix $\boldsymbol{A}$ compared with $1/(10\ eps)$.

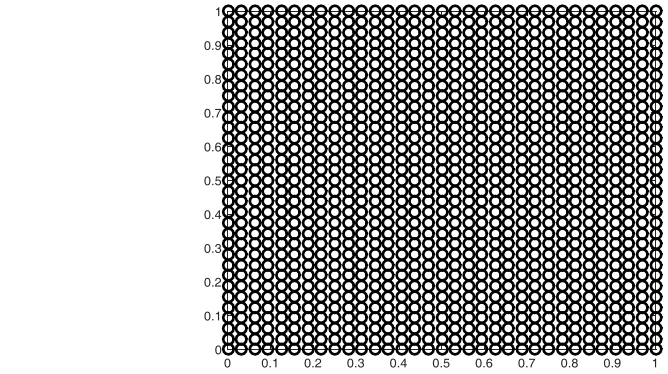

(a)

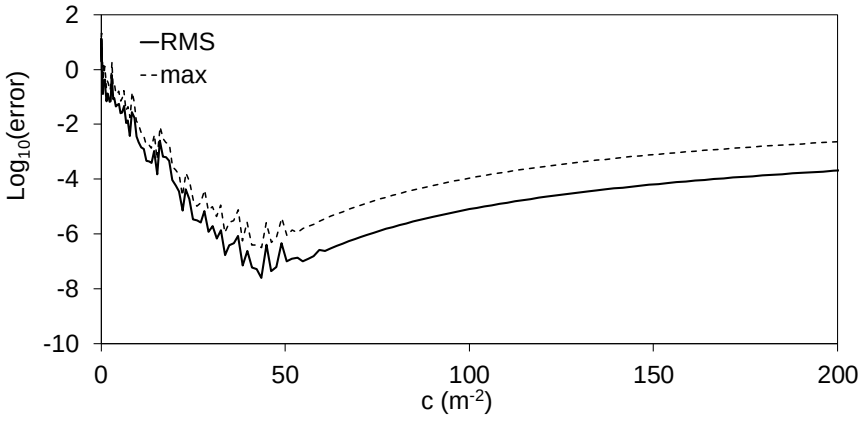

(b)

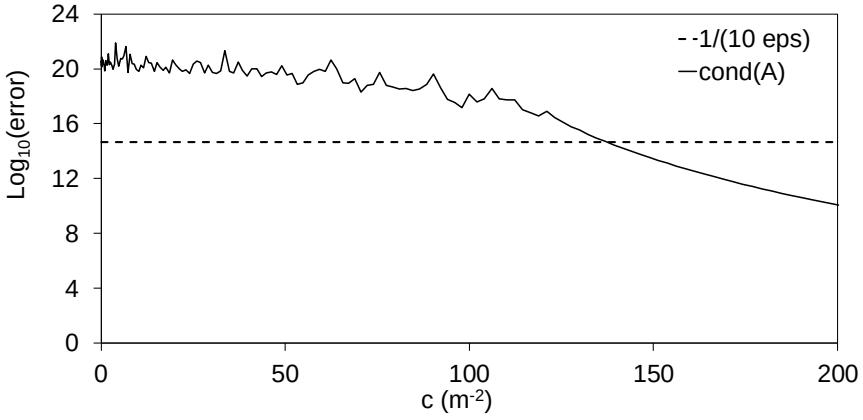

(c)

Figure 2.6: Interpolation of the Franke's function with 1089 CPs: (a) CPs. (b) $RMSE$ and max error; (c) condition number of the interpolation matrix $\boldsymbol{A}$ compared with $1/(10\ eps)$.

Table 2.2: Best scenarios with respect to the lower $RMSE$ error in the cases under test. The Gaussian RBFs have been used.

#CPs	c (m^{-2})	$RMSE$ error	max error	$cond_2(A)$
81	16.00	0.0046	0.0245	2.0309E+06
289	31.36	1.2374E-04	0.0012	8.5033E+13
1089	43.56	2.4761E-08	3.1330E-07	2.8024E+19

As can be noted, in the case of 1089 CPs the minimum error is achieved in a ill-conditioning region in fact in this case the condition number of the matrix $\boldsymbol{A}$ is equal to $2.8024E + 19$. This phenomenon is quite common in the case of an "high" number of CPs and is related to the trade-off principles of the RBFs-interpolation procedures [2].

Various algorithms have been developed in order to calculate the optimal shape parameter c. The most common are:

- The Contour-Padé Algorithm [14]. This method is limited to a relative small number of unknowns.
- trial and error strategy [2, p. 142]. This method is the most simple and consists in the evaluation of the error between the function to interpolate and its interpolation. Of course this is possible only when the function to interpolate is known and for this reason in a limited number of applications
- Use of the power function as Indicator [2, p. 142].
- Leave One Out Cross Validation (LOOCV) presented by Rippa in [15] and analyzed in the next subsection.

LOOCV

The LOOCV finds the optimal shape parameter c by minimizing the (least-square) error for a fit of data based on an interpolant for which one of the CPs is left out. In particular, consider the test function $f(\boldsymbol{x})$, calling $f_k = f(\boldsymbol{x}_k)$ the generic data. Suppose that the set of data has N elements $\{f_1, \ldots, f_N\}$, Constructing the radial basis function interpolant $P_{f,k}$

$$P_{f,k}(\boldsymbol{x}) = \sum_{i=1, i\neq k}^{N} a_{i,k}\phi(\|\boldsymbol{x} - \boldsymbol{x}_i\|_2) \tag{2.18}$$

such that

$$P_{f,k}(\boldsymbol{x}_j) = f_j \quad \text{with} \quad j = 1, \ldots, k-1, k+1, \ldots, N \tag{2.19}$$

After this, the error at the point $(\boldsymbol{x}_k)$ is calculated

$$E_k = f_k - P_{f,k}(\boldsymbol{x}_k) \tag{2.20}$$

Then the quality of fit is measured by finding the superior value inside the entries of $E = [E_1, \ldots, E_N]^T$. The optimal shape parameter c is that one that minimize such measure. This method is quite slow, in fact, it has a complexity of $\mathcal{O}(N^4)$. An other important limitation of this method is that it is not trivial the choice of the test function to use. It is in fact important to highlight that that a proper test function should be chosen taking into account the nature of the solutions that are expected. Of course this is not always possible.

To illustrate this important aspect, let us consider the case in which the optimal shape parameter has to be computed inside the 2D unitary square $[0, 1] \times [0, 1]$. and the cases with 25, 81, and 289 CPs as shown in Fig. 2.7(a). The LOOCV is before executed using the Franke's function (2.17) giving the results shown in Fig. 2.7(b), and then using the $sinc(x, y) = sinc(x)sinc(y)$ function obtaining those shown in Fig. 2.7(c). As can be seen by comparing the Fig. 2.7(b) and the Fig. 2.7(c) the chosen test function is chosen can significantly change the optimal shape parameter.

2.3 Example of Interpolation Problem

In order to evaluate the efficiency and accuracy of the presented theory an electrostatic problems with a known analytical solution is taken into account. Consider the problem shown in Fig. 2.8(a) where three sides of the domain are maintained at zero potential, while the upper side is kept at $10V$. The potential inside the domain is the solution of the Laplace equation under a proper boundary condition and has the following expression [8]:

$$V(x, y) = \frac{40}{\pi} \sum_{k=1}^{\infty} \frac{sin\frac{(2k-1)\pi x}{a} sinh\frac{(2k-1)\pi y}{a}}{(2k-1)sinh\frac{(2k-1)\pi b}{a}} \tag{2.21}$$

In the following the unitary rectangle will be considered as domain ($a = 1$m

and $b = 1\text{m}$). The graph of the solution is shown in Fig. 2.8(b). The simulation was run with the 256 CPs shown in Fig. 2.9(a). While the results were evaluated in the 961 evaluation points in Fig. 2.9(b). In Tab. 2.3 three cases are considered. The first is that one in which the simulation is conducted by choosing the shape parameter given by the LOOCV algorithm and using the *sinc* as test function. The second one is the case in which the simulation is conducted by choosing the shape parameter given by the LOOCV algorithm and using the expected solution as test function (see Fig. 2.8(b)). The last case is the result of the simulation run with the best shape parameter (which minimizes the $RMSE$). In this example it is possible to appreciate the importance of choosing a "good" c.

Table 2.3: Simulation results of the problem in Fig. 2.8. Three cases are considered: (1) the shape parameter is fond with the LOOCV and the *sinc* function as test. (2) the shape parameter is fond with the LOOCV and the expected function as test, and (3) the best shape parameter that minimizes the $RMES$ has been chosen

Case	c (m^{-2})	$RMSE$ error	max error	$cond_2(A)$
1	2.9	8.424549E-01	4.50	2.76E+18
2	6.3	2.042970E-01	2.34	1.52E+20
3	9.8	8.897187E-02	1.84	4.18E+18

2.4 Conclusion

In this chapter a brief introduction about the meshless method has been given. In order to present this technique the interpolation problem inside a bounded domain has been taken into account. This is actually the kind of problem in which the Meshless Method and the radial basis functions are more extensivelly used. Various aspects have been shown. In particular various considerations about the precision, stability, and the choice of the collocation points have been reported. For more details about this topic the reader is addressed to the references at the end of this chapter.

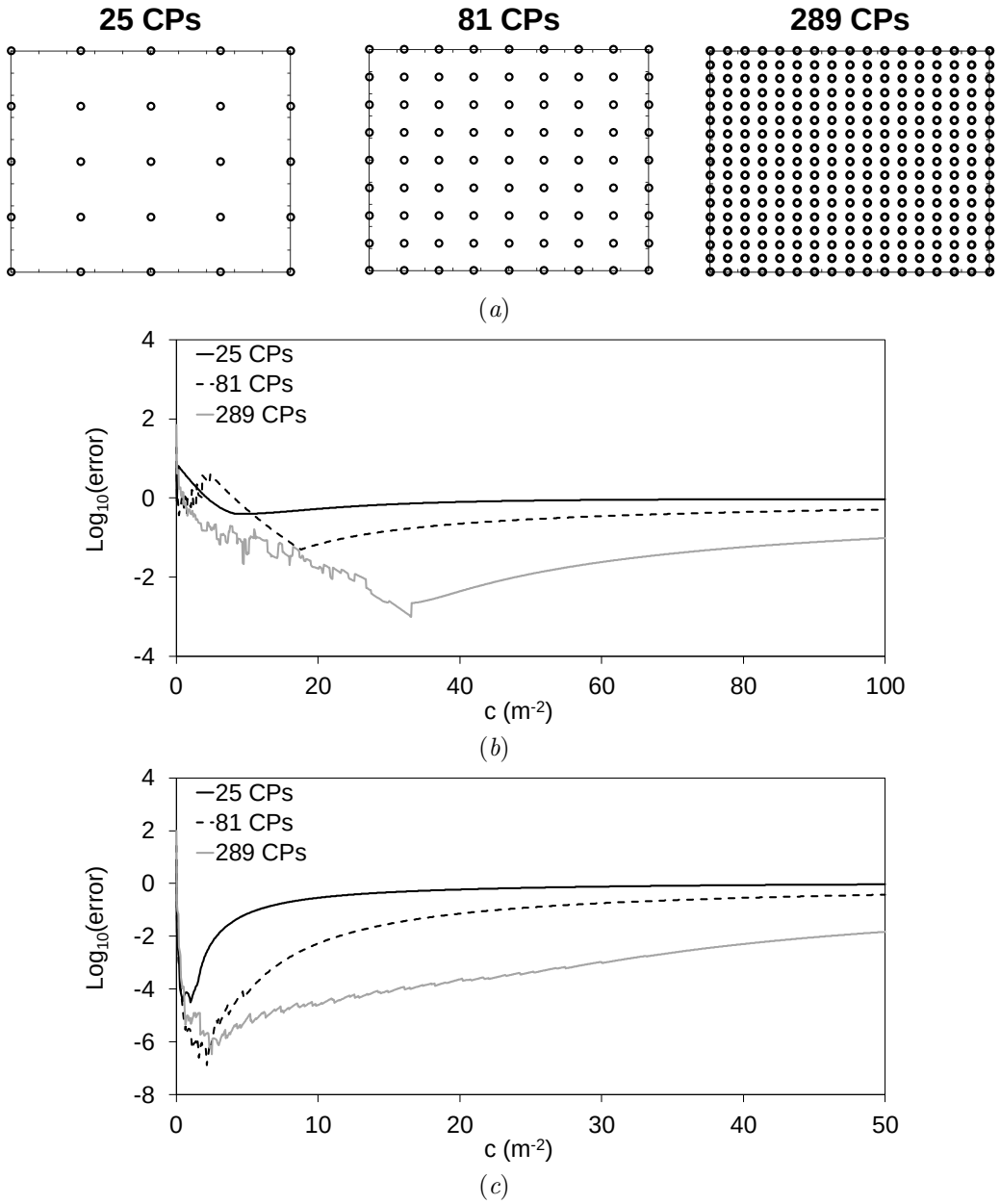

Figure 2.7: LOOCV execution over the 2D unitary square $[0,1] \times [0,1]$: (a) three configurations taken into account: 25, 81, and 289 CPs (b) result in the case of Franke's test function; (c) result in the case of *sinc* test function.

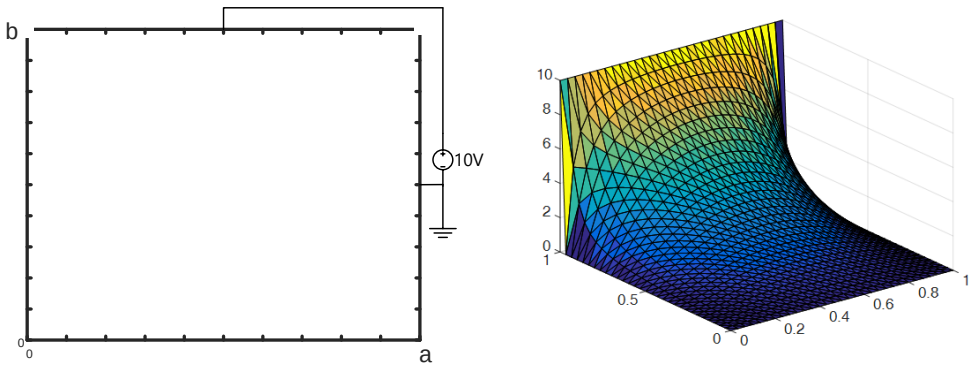

(a) (b)

Figure 2.8: Example of Interpolation problem: (a) Cross section of the rectangular conducting boundary, with an insulating gap between the upper side and the other three (b) Shape of the theoretical solution inside the domain under study.

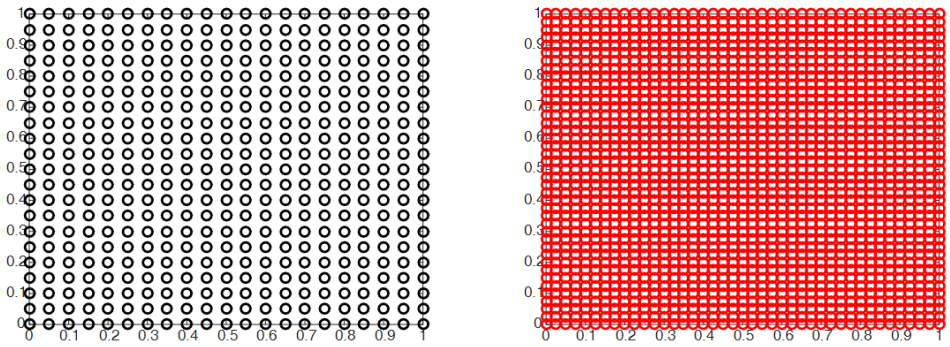

(a) (b)

Figure 2.9: Example of Interpolation problem: (a) Collocation points used during the simulation (b) Evaluation points.

Bibliography

[1] G. R. Liu, *Meshfree methods: moving beyond the finite element method*, Boca Raton,: World Scientific, 2007.

[2] G. E. Fasshauer, *Meshfree approximation methods with MATLAB*, Vol. 6, Chicago,: CRC Press, 2003.

[3] M. Mongillo, "Choosing basis functions and shape parameters for radial basis function methods," *SIAM Undergraduate Research Online*, Vol. 4, pp. 190–209, 2011.

[4] M. N. O. Sadiku, *Numerical techniques in Electromagnetic*, 2nd ed., CRC press, 2011.

[5] B. Fornberg and C. Piret, "On choosing a radial basis function and a shape parameter when solving a convective PDE on a sphere," *J. Comput. Phys.*, Vol. 227,No. 5, pp. 2758-2780, 2008.

[6] J.C. Mairhuber, "On Haar's theorem concerning Chebychev approximation problems having unique solutions," *Proceedings of the American Mathematical Society*, Vol. 7,No. 4, pp. 609-615., 1956.

[7] Y. Q. Zhang, G. C. Wan, K. Yang, and M. S. Tong, "On the point-matching method for solving electromagnetic radiation problems," *2013 IEEE Antennas and Propagation Society International Symposium (APSURSI)*, Orlando, FL, 2013, pp. 1526-1527.

[8] W.R. Madych, "Error estimates for interpolation by generalized splines," *In Curves and surfaces (Academic Press)*, Vol. 7,No. 4, pp. 297-306., 1991.

[9] R. Schaback, "Native Hilbert spaces for radial basis functions I.," *New Developments in Approximation Theory*, Birkhäuser, Basel, pp. 255-282., 1999.

[10] J. H. Wilkinson, *The algebraic eigenvalue problem*, Vol. 87, Oxford: Clarendon Press, 1965.

[11] R. Schaback, "Multivariate interpolation and approximation by translates of a basis function," *Proceedings of the American Mathematical Society*, Vol. 6, pp. 491-514, 1995.

[12] S. De Marchi, R. Schaback, and H. Wendland, "Near-optimal data-independent point locations for radial basis function interpolation," *Advances in Computational Mathematics*, Vol. 23, pp. 317-330, 2005.

[13] R. Franke, "A critical comparison of some methods for interpolation of scattered data," *Naval Postgraduate School Tech.Rep*, NPS-53-79-003, Mar. 1979.

[14] B. Fornberg and G. Wright "Stable computation of multiquadric interpolants for all values of the shape parameter," *Computers & Mathematics with Applications*, Vol. 48,No. 5-6, pp. 853-867., Sep. 2004.

[15] S. Rippa "An algorithm for selecting a good value for the parameter c in radial basis function interpolation," *Advances in Computational Mathematics*, Vol. 11,No. 2-3, pp. 193-210., Nov. 1999.

Chapter 3

Considerations about the Classical Approach

3.1 Introduction

In the previous chapter the meshless method and the RBFs have been presented in the special case of the interpolation problem. Another application of them will be presented in this chapter: the solution of partial differential equations (PDEs) with a proper boundary condition. The presentation will be focused on the electromagnetic problems and in particular on the case of the propagation of the electromagnetic field inside an hollow waveguide. In the literature there are various kind of examples of solution of PDEs (see for instance [1, 2, 3, 4, 5, 6]). In [4] a very efficient algorithm is presented for the solution of elliptic PDEs. It has been later applied the the case of the electromagnetic propagation inside an homogeneous shielded waveguide by Lai in [7]. In this work the problem of finding the eigenmodes inside the domain has been reduced to a generic eigenproblem by using the point matching technique [7, 8] for both the PDE and the boundary condition as suggested by Kansa. The resulting matrix problem is computed very quickly, but it presents some drawbacks such as the singularity of the mass matrix, the non symmetric nature of the matrices, and thus the ill-conditioning of the resulting problem [9]. Moreover the solution found though this technique suffers a strong dependence on the position of the collocation points [10] and, even worse, a relative bed precision in the calculation of the first TE modes [2] that are encountered by applying the Neumann Condition [11]. In [10] a very simple approach has been proposed to mitigate these last two problems without cost of time and memory. Most of this chapter is therefore based on

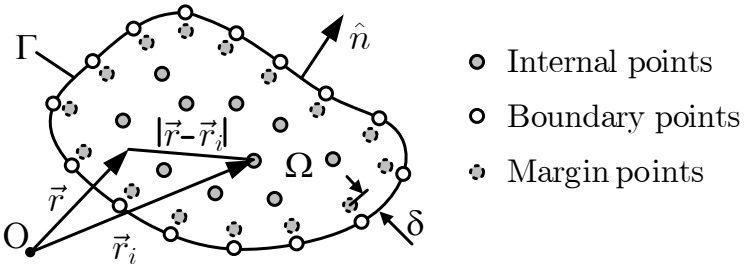

Figure 3.1: © 2017 IEEE–Cross-section of a generic metallic waveguide with the different sets of collocation points used to define the RBFs.

[10] and will reuse extensively the material of that work.

3.2 Outline of the Theory

Consider the cross section Ω of an infinite long waveguide shielded by a perfect conductor and filled by an homogeneous media (in this chapter the vacuum will be considered) and represented in Fig. 3.1 where Γ is the boundary. In this case the electromagnetic field inside the structure can be represented through an infinite set of TE and TM modes [11], which are respectively the transversal electric and magnetic modes. These kind field configurations will be the solution of the Helmholtz scalar equation and a proper boundary condition given by the operator B, in particular

$$\begin{cases} \nabla^2\Phi(\vec{r}) + k^2\Phi(\vec{r}) = 0 & \vec{r} \in \Omega \\ B\left[\Phi(\vec{r})\right] = 0 & \vec{r} \in \Gamma \end{cases} \tag{3.1}$$

where k is the wavenumber, $\Phi(\vec{r})$ is the generic Hertz-Debye potential [11], $\vec{r}$ is the generic observation point inside the domain under study, and the operator B can the Dirichlet boundary condition in the case of the TM modes and the Neumann boundary condition for the TE modes:

$$B\left[\Phi(\vec{r})\right] = \begin{cases} \Phi(\vec{r}) = 0 & \text{for TM modes} \\ \dfrac{\partial\Phi(\vec{r})}{\partial n} = 0 & \text{for TE modes} \end{cases} \tag{3.2}$$

where $\hat{n}$ is the outward normal unit vector on the boundary Γ (Fig. 3.1).

To discretize the problem (3.1), the RBF approximation is used and in particular $\Phi(\vec{r})$ can be described as follows

$$\Phi(\vec{r}) = \sum_{i=1}^{N} a_i \phi_i(\vec{r}) \tag{3.3}$$

where a_i are unknown coefficients, and the i-th RBF has been introduced

$$\phi_i = \phi(\|\vec{r} - \vec{r}_i\|_2) \tag{3.4}$$

Recalling the Chap. 2, every ϕ_i is centered in its own center $\vec{r}_i$ called collocation point CP (Fig. 3.1). N is the total number of the CPs defined over the domain. In particular, $N = L + M$ where L is the number of the CPs defined in inside the domain (with index $i = 1, \ldots, L$) and M is the number of CPs defined on Γ (with index $i = L + 1, \ldots, N$). The definition of some point exactly on the boundary is not a trivial choice since the classical approach under study in this chapter is essentially a point matching technique which explicitly requires the imposition of the boundary condition. As seen in Chap. 2, there are various kind of RBFs, the work presented in this manuscript is conducted by using the Gaussian type

$$\phi_i(\vec{r}) = e^{-c|\vec{r}-\vec{r}_i|^2} \tag{3.5}$$

where the shape parameter c is defined in order to work with the stationary approach (see Chap. 2) and in particular as is done in [12]

$$c = \frac{1}{\alpha h^2} \tag{3.6}$$

where α is a parameter typically selected by using preconditioning algorithms like the LOOCV introduced in the Chap. 2 and h is the fill distance between the collocation points and approximated as suggested in [12]

$$h \approx \frac{\sqrt{A_\Omega}}{\sqrt{N} - 1} \tag{3.7}$$

where A_Ω is the cross-section area. By substituting (3.3) in (3.1), and applying a point-matching technique in the collocation points, (2.1) becomes

$$\begin{cases} \sum_{i=1}^{N} a_i \left[\nabla^2 \phi_i(\vec{r}_j) + k^2 \phi_i(\vec{r}_j)\right] = 0 & j = 1, \ldots, L \\ \sum_{i=1}^{N} a_i B\left[\phi_i(\vec{r}_j)\right] = 0 & j = L+1, \ldots, N \end{cases} \tag{3.8}$$

In the case of TE modes in particular

$$B\left[\phi_i(\vec{r}_j)\right] = \frac{\partial \phi_i(\vec{r}_j)}{\partial n} \tag{3.9}$$

Note that the derivative of the RBFs is known analytically. This permits a straightforward implementation of the algorithm. The system of equations (3.8) permits to assemble a matrix eigenproblem that can be solved numerically.

$$\boldsymbol{A}\boldsymbol{a} - k^2\boldsymbol{B}\boldsymbol{a} = \boldsymbol{0} \tag{3.10}$$

where the matrices $\boldsymbol{A}$ and $\boldsymbol{B}$ are $N \times N$ real matrices. By solving (3.10) the cutoff wavenumbers k_m and of the corresponding eigenvectors $\boldsymbol{a}_m = [a_{m,1}, a_{m,2}, \ldots, a_{m,N}]$ can be computed. Recall that the generic eigenvector $\boldsymbol{a}_m$ allows to calculate the modal scalar potential through (3.3).

3.3 Classical Approach: State of Art

To evaluate the efficiency and the reliability of the method various simulations have been carried out in the standard case of a WR90 hollow waveguide, which has a rectangular cross-section with dimensions 22.86 mm × 10.16 mm. All the analysis in this section and the next one is focused on the evaluation of the first 40 TE modes. Since this is the most critical case as explained in Sec. 3.1.

In all the reported cases the simulations were run with $N = 196$ CPs and in particular with $L = 144$ internal CPs in Ω and $M = 52$ boundary CPs on Γ. As one of the aim of the study (reported in [10]) was to make considerations on the dependence of the solution on the position of the CPs, and since the Meshless Method should be reliable also in the case of a non-structured grid of CPs, the first case evaluated was the one of a random distribution (with a uniform statistic). The result is presented in Fig. 3.2 where the obtained distribution of CPs and the resulting error over the computed wavenumbers respect to the analytical solution are shown. In particular this error is defined as

$$\textit{Relative Error} = \frac{|k_c - k_t|}{k_t} \tag{3.11}$$

where k_c is the computed eigenvalue by using the meshless method and k_t is the theoretical wavenumber.

By using (**??**) the average distance $h = 1.172$ mm is obtained. The choice of the parameter α has been made by using the LOOCV algorithm. This gave

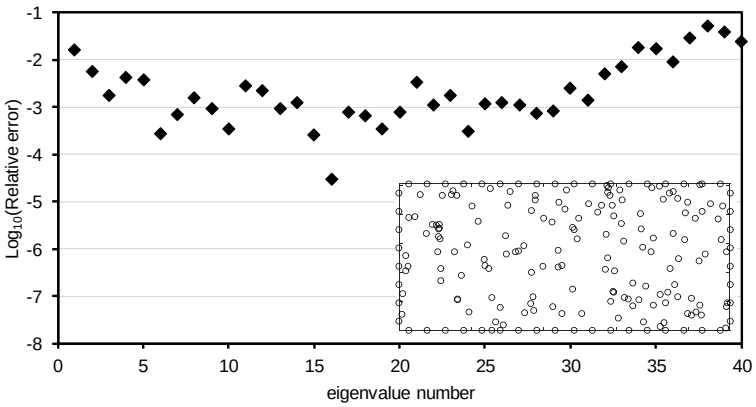

Figure 3.2: © 2017 IEEE– Relative error in the calculation of the cutoff frequencies of the first 40 TE modes of a WR90 rectangular waveguide using $N = 196$ Gaussian RBFs ($L = 144$, $M = 52$), $h = 1.172$ mm, and $\alpha = 8$ and a random distribution of the internal points.

an optimum value of $\alpha = 8$. As expected by Palette in [2], the error over the first TE mode is not the lower obtained in all the computed spectrum. Actually, it is, in this case, larger than 1%. Moreover, increasing the number of CPs does not improve this behavior. This is of course a problem issue when designing a waveguide, since in this case, the first modes are the most important. This problem was already highlighted in [2], where a possible countermeasure was proposed, relying on the placement of some internal collocation points closer to the boundary points (margin points placed at distance $\delta < h$ from the boundary, see Fig. 3.1). In fact, the poor accuracy shown in Fig. 3.2, seems due to the limited number of internal CPs close to the boundary. However, to simplify the procedure, a regular grid was adopted in [2], thus reducing the flexibility of the meshless method. The resulting error and the obtained grid is shown in Fig. 3.3 but , as can be seen, the behavior of the algorithm has not significant differences respect to the previous case. Finally, the case of a random grid, but with the use of the margin points, was evaluated and reported in Fig. 3.4. Also in this occasion there were not an improvement on the calculation of the first TE modes.

3.4 Possible Improvement

As seen in the previous section, the theory presented in 3.2 does not permit to achieve a certain level of accuracy and in particular seems to show a significant dependence of the solution on the position of the CPs. The

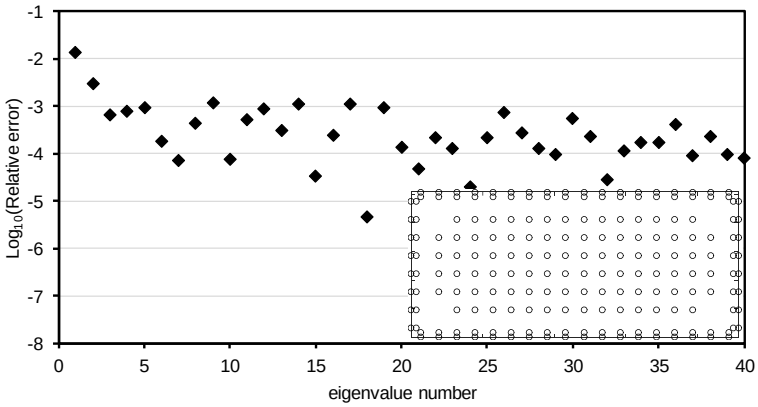

Figure 3.3: © 2017 IEEE– Relative error in the calculation of the cutoff frequencies of the first 40 TE modes of a WR90 rectangular waveguide using $N = 196$Gaussian RBFs ($L = 144$, $M = 52$), $h = 1.172$ mm, and $\alpha = 8$ and a regular distribution of the internal points with margin points ($\delta = h/2$).

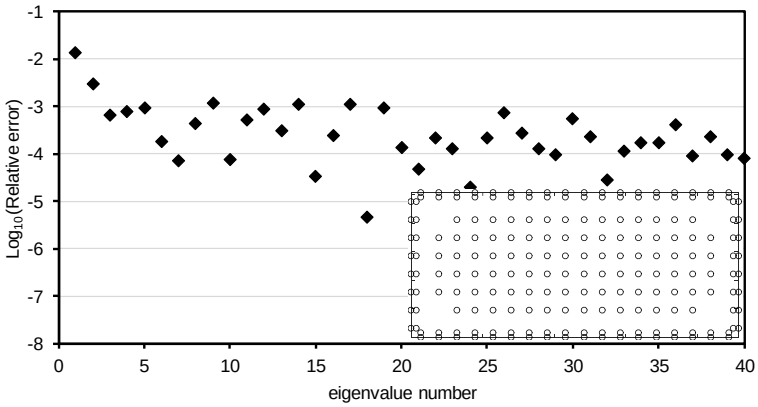

Figure 3.4: © 2017 IEEE– Relative error in the calculation of the cutoff frequencies of the first 40 TE modes of a WR90 rectangular waveguide using $N = 196$ Gaussian RBFs ($L = 144$, $M = 52$), $h = 1.172$ mm, and $\alpha = 8$ and a quasi-random distribution of the internal points with margin points ($\delta = h/2$).

core of this thesis is the development of a novel technique that overcomes all these issues and improves the numerical stability by using the meshless method in conjunction with the variational technique [8]. However the classical approach of Sec. 3.2 can be significantly improved by implementing a slightly different definition of the RBFs employed to discretize the problem. It is possible to note, in fact, that all the RBFs are defined using a common shape parameter c. This can cause a certain correlation between them (in

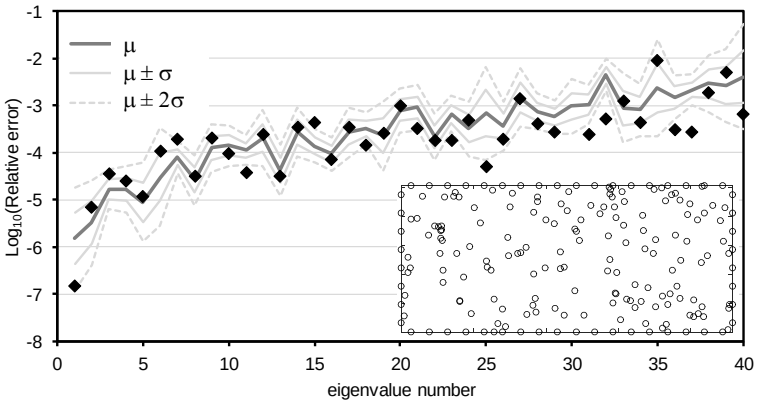

Figure 3.5: © 2017 IEEE– Error in the calculation of the modes by adopting the proposed randomization of the shape parameter of the Gaussian RBFs, assuming $0 < \xi_i < 1$ in (3.12) with the same random distribution as in Fig. 3.2. 2000 simulations have been performed, and the markers represent the results for a specific set of ξ_i, whereas the lines represents the mean value, the mean value plus/minus the variance, and the mean value plus/minus two times the variance.

particular in the case of a random grid) and thus can increase the linear dependence of some raws inside the matrices $\boldsymbol{A}$ and $\boldsymbol{B}$ of (3.10). For this reason, in [10], this new definition is proposed

$$\phi_i(\vec{r}) = e^{-c_i|\vec{r}-\vec{r}_i|^2} \quad \text{with } c_i = \xi_i c \tag{3.12}$$

where ξ_i is a parameter generated for each RBF with a uniform distribution in the interval $(0, 1)$. The same simulations of the previous section (with the same distribution of CPs) have been than run using (3.12) instead of (3.5). The obtained results are shown in Fig. 3.5 for the case of a random grid, in Fig. 3.6 for the case of a uniform grid, and in Fig. 3.7 for the case of a random grid with the use of the margin CPs. In all these figure it is possible to find the position of the CPs, the results for a particular simulation and the statistical considerations. About this last aspect, in particular, 2000 simulations have been run generating for the same CPs configuration a new set of values ξ_i each time. The mean computed error μ for every wavenumber is shown, in conjunction with the intervals $\mu \pm \sigma$ where σ is the variance. As can be found out, for every configuration of CPs there is a significantly improvement on the accuracy of the first computed modes and no change for the others. Note, in particular, that, the expedient shown in this section, does not increase the computation time of the simulation since there is no

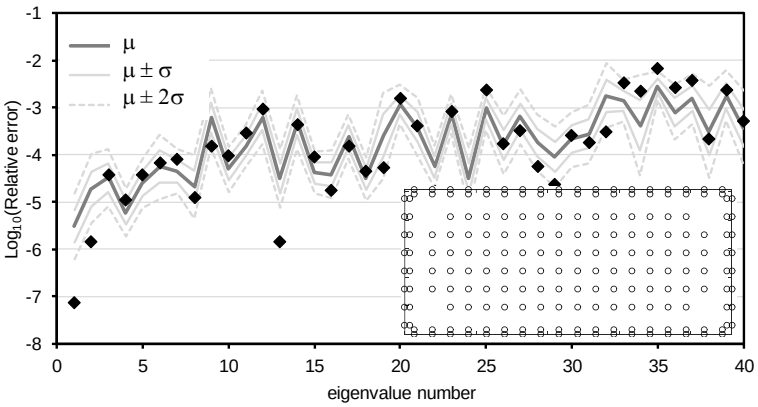

Figure 3.6: © 2017 IEEE– Error in the calculation of the modes by adopting the proposed randomization of the shape parameter of the Gaussian RBFs, assuming $0 < \xi_i < 1$ in (3.12) with the same uniform distribution as in Fig. 3.3. 2000 simulations have been performed, and the markers represent the results for a specific set of ξ_i, whereas the lines represents the mean value, the mean value plus/minus the variance, and the mean value plus/minus two times the variance.

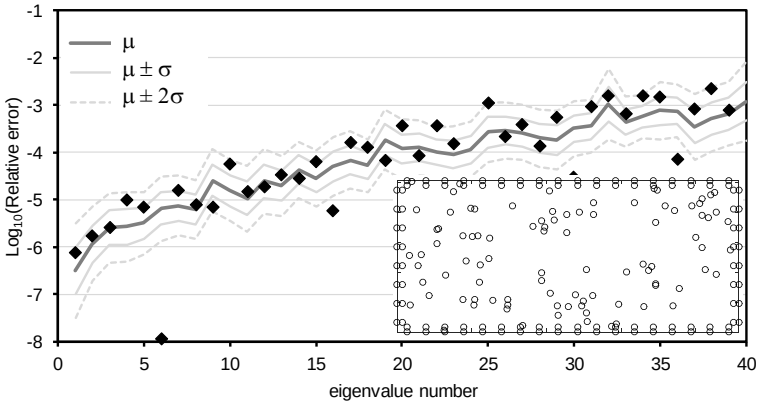

Figure 3.7: © 2017 IEEE– Error in the calculation of the modes by adopting the proposed randomization of the shape parameter of the Gaussian RBFs, assuming $0 < \xi_i < 1$ in (3.12) with the same quasi-random distribution as in Fig. 3.4. 2000 simulations have been performed, and the markers represent the results for a specific set of ξ_i, whereas the lines represents the mean value, the mean value plus/minus the variance, and the mean value plus/minus two times the variance.

variation on the dimension of $\boldsymbol{A}$ and $\boldsymbol{B}$. Moreover in this case also the totally random grid gives relative good results.

3.5 Conclusion

In this chapter the classical approach, to apply the meshless method, has been presented. Some limitations known in the literature have been shown focusing on an electromagnetic problem. In particular, it has been shown that the this classical technique exhibits a strong dependence of the solution on the position of the CPs and a relative poor accuracy in the computation of the first TE modes of a waveguide. A very simple and no time consuming improvement has been proposed, by using a slightingly different definition of the employed RBFs. The obtained results outperform those given by the classical approach and are obtained relaxing all kind of requirement on the regularity of the grid where the CPs are defined.

Bibliography

[1] E. Larsson and B. Fornberg, "A numerical study of some radial basis function based solution methods for elliptic PDEs," *Computers & Mathematics with Applications*, Vol. 46, No. 5 pp. 891–902, Sep. 2003.

[2] R. B. Platte and T. A. Driscoll, "Computing eigenmodes of elliptic operators using radial basis functions," *Computers & mathematics with applications*, Vol. 48, No. 3, pp. 561-576, 2004.

[3] S. De Marchi, A. Martinez, E. Perrocchione, and M. Rossini, "RBF-based partition of unity methods for elliptic PDEs: Adaptivity and stability issues via variably scaled kernels," *J Sci Comput.*, Vol. 79, No. 1, pp. 321-344, Apr. 2019.

[4] E. J. Kansa, "A scattered data approximation scheme with applications to computational fluid-dynamics–II solutions to parabolic, hyperbolic and elliptic partial differential equations," *Computers & mathematics with applications*, Vol. 19, No. 8-9, pp. 147-161, Jan. 1990.

[5] C. Franke and R. Schaback, "Solving partial differential equations by collocation using radial basis functions," *Appl. Math. Comput.*, Vol. 93, No. 1, pp. 73-82, Jul. 1998.

[6] R. L. Hardy, "Multiquadric equations of topography and other irregular surfaces," *J. Geophys. Res.*, Vol. 76, No. 8, pp. 1905-1915, Mar. 1971.

[7] S. J. Lai and B. Z. Wang, "Solving Helmholtz equation by meshless radial basis functions method," *Progress In Electromagnetics Research B*, Vol. 24, pp. 351–367, 2010

[8] M. N. O. Sadiku, *Numerical techniques in Electromagnetic*, 2nd ed., CRC press, 2011.

[9] J. H. Wilkinson, *The algebraic eigenvalue problem*, Vol. 87, Oxford: Clarendon Press, 1965.

[10] V. Lombardi, M. Bozzi, and L. Perregrini, "An Improved Meshless Method for Waveguide Eigenvalue Problems," Vol. 27, No. 12, pp. 1047–1049, Dec. 2017

[11] R. E. Collin, *Field Theory of Guided Waves*, IEEE Press, 2nd ed., Piscataway (NJ), USA, 1991.

[12] T. Kaufmann, C. Engström, C. Fumeaux, and R. Vahldieck, "Eigenvalue analysis and longtime stability of resonant structures for the meshless radial point interpolation method in time domain," *IEEE Trans. Microw. Theory Techn.*, Vol. 58, No. 12, pp. 3399–3408, Dec. 2010.

Chapter 4

The Variational Meshless Method for Homogeneous Waveguides

4.1 Introduction

In the previous chapter a very simple expedient has been proposed to improve the accuracy in the calculation of the first TE modes inside a hollow shielded waveguide. The theory presented there presents in any case some numerical limitations as the resulting eigenproblem is built with non-symmetric and singular matrices [1]. This leads to a ill-conditioned problem (see [2] for reference). Another limitation associated to this aspect is that a low degree of accuracy can be achieved in the calculation of the eigenvectors. For this reason the Point Matching technique fails when dealing with very general geometries where the field presents more rapid variations (e.g. in proximity of sharp corners).

To tackle this limitations, in [3] the variational meshless method (VMM) has been presented which combines the meshless method with the variational technique. As will be shown this method permits the computation of an high number of modes with a relative limited number of unknowns and an appreciable precision.

Moreover, in this work an automatic refinement technique was presented to improve the accuracy of the solution in presence of complicated geometries. As will be shown this can be done without the manual intervention of the user and keeping the eigenproblem numerical stable also after an arbitrarily number of refinement cycles.

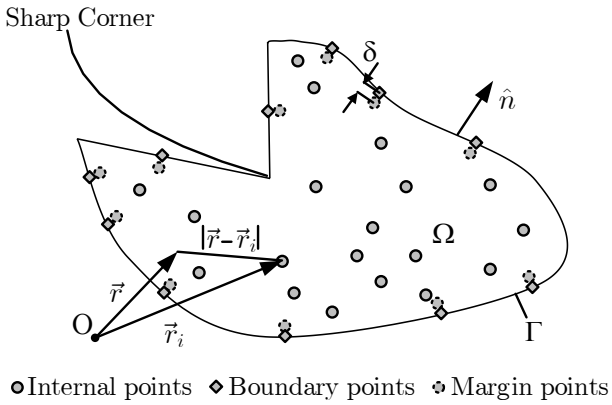

Figure 4.1: © 2018 IEEE– Cross-section of a generic metallic waveguide with the different sets of collocation points used to define the RBFs.

An other important aspect to highlight is that the present theory will permit to start the simulation without the need of a time consuming preconditioning step as generally happens in all the previous works published in the literature [4, 15].

In this chapter the VMM and the automatic refinement technique are presented, therefore most of this chapter is based on [3] and will reuse extensively the material of that work.

4.2 The Meshless Variational Approach with RBFs

In Fig. 4.1 the generic hollow waveguide shielded with a perfect conductor is shown where Ω is the cross section, while Γ is the boundary. In this case the electromagnetic field can be completely represented through 2 set of solutions which are called TE and TM modes and are subjected of the Helmholtz equation [5]

$$\nabla^2\Phi(\vec{r}) + k^2\Phi(\vec{r}) = 0 \qquad \vec{r} \in \Omega \tag{4.1}$$

with a proper boundary condition (BC): the Neumann BC for the first set and the Dirichlet BC for the second one, leading to

$$\frac{\partial\Phi(\vec{r})}{\partial n} = 0 \qquad \vec{r} \in \Gamma, \text{ for TE modes} \tag{4.2}$$

$$\Phi(\vec{r}) = 0 \qquad \vec{r} \in \Gamma, \text{ for TMmodes} \tag{4.3}$$

where Φ is the Hertz-Debye potential, $k = \omega\sqrt{\mu\epsilon}$ is the wavenumber, ω is the angular frequency, ϵ and μ are the electric permittivity and the magnetic permeability of the medium, respectively, $\vec{r}$ is the generic observation point, and $\hat{n}$ is the outward normal unit vector to the boundary (Fig. 4.1).

Equation (4.1) has an equivalent variational formulation (see [7] for reference), for this reason can be found by extremizing the following functional

$$I(\Phi) = \frac{1}{2}\int_{\Omega} \nabla\Phi \cdot \nabla\Phi - k^2\Phi^2 \, dS \tag{4.4}$$

under (4.2) in the case of TE modes or (4.3) in the case of the TM ones. The basic idea of the VMM is to apply the RBF approximation (see Chap. 2) to the variational problem of (4.4) and thus to write the unknown potential as

$$\Phi(\vec{r}) = \mathbf{\Phi}^T(\vec{r}) \; \boldsymbol{a} \tag{4.5}$$

where $\mathbf{\Phi}(\vec{r}) = [\phi_1(\vec{r}), \phi_2(\vec{r}), .., \phi_N(\vec{r})]^T$ is built with the RBFs evaluated in the point $\vec{r}$ and $\boldsymbol{a} = [a_1, a_2, .., a_N]^T$ is composed by the unknown coefficients a_i. As in the previous chapter, N CPs, are defined and in particular L are the internal collocation points (ICPs) that lie within Ω, and $M = N - L$ are boundary collocation points (BCPs) that lie on Γ (see Fig. 4.1). In particular, the ICPs are with indexes $j = 1, \ldots, L$ while the BCPs are with indexes with $j = L + 1, \ldots, N$.

The RBF used from now on are defined as in the previous chapter

$$\phi_i(\vec{r}) = e^{-c_i|\vec{r}-\vec{r}_i|^2} \tag{4.6}$$

where the shape parameter c_i is defined as in [9]

$$c_i = \frac{\xi_i}{\sigma h^2} \; , \tag{4.7}$$

ξ_i is a scalar value generated randomly within a normal distribution in the interval $(0, 1)$ for every CP, h is the average distance which can be computed as in (3.7), and σ is a parameter typically selected by using preconditioning algorithms, like the leave-one-out cross validation (LOOCV) algorithm [4]. As will be shown in Sec. 4.4 this step can be avoided by setting $\sigma = 1$.

Sometime, as explained in [10, 11], to improve the accuracy and reduce the dependence of the solution on the position of the ICPs some CP are added in proximity of the boundary and in particular close to every BCP but translated $\delta = h/2$ toward the inner side and thus in the direction $-\hat{n}$, where $\hat{n}$ is the normal outgoing unit vector on the contour Γ (see Fig. 4.1). This points are called margin collocation points (MCPs).

4.2.1 TE Modes

The case of the TE modes is the simpler as in this case the BC must not be imposed explicitly since the Neumann BC is a *natural* property of the functional (4.4). See [12] for reference. On substitution of (4.5) in (4.4), the functional $I(\Phi)$ becomes a function of the coefficients $\boldsymbol{a}$

$$I(\boldsymbol{a}) = \frac{1}{2}\left[\boldsymbol{a}^{\boldsymbol{T}}(\boldsymbol{X}+\boldsymbol{Y})\boldsymbol{a} - k^2\boldsymbol{a}^{\boldsymbol{T}}\boldsymbol{Z}\boldsymbol{a}\right] \tag{4.8}$$

where the entries of the matrices $\boldsymbol{X}$, $\boldsymbol{Y}$, and $\boldsymbol{Z}$ are

$$\begin{aligned} X_{ij} &= \int_\Omega \frac{\partial\phi_i(r)}{\partial x}\frac{\partial\phi_j(r)}{\partial x}\,dS \\ Y_{ij} &= \int_\Omega \frac{\partial\phi_i(r)}{\partial y}\frac{\partial\phi_j(r)}{\partial y}\,dS \\ Z_{ij} &= \int_\Omega \phi_i(r)\phi_j(r)\,dS \end{aligned} \tag{4.9}$$

thus the extremization of the functional $I(\boldsymbol{a})$, can be enforced by deriving, respect to the vector $\boldsymbol{a}$, its expression as follows

$$\frac{\partial I(\boldsymbol{a})}{\partial \boldsymbol{a}} = \boldsymbol{0}\ . \tag{4.10}$$

This permits to obtain the following equation where the matrices $\boldsymbol{A}$ and $\boldsymbol{B}$ are introduced

$$\underbrace{(\boldsymbol{X}+\boldsymbol{Y})}_{\boldsymbol{A}}\boldsymbol{a} - k^2\underbrace{\boldsymbol{Z}}_{\boldsymbol{B}}\boldsymbol{a} = \boldsymbol{0} \tag{4.11}$$

For this reason the TE eigenmodes can be computed by solving the following eigenproblem

$$\boldsymbol{A}\boldsymbol{a} - k^2\boldsymbol{B}\boldsymbol{a} = \boldsymbol{0} \tag{4.12}$$

with dimension $N \times N$ (i.e., the total number of CPs), and $\boldsymbol{A}$ and $\boldsymbol{B}$ always real, symmetric, and non-singular.

4.2.2 TM Modes

When computing the TM modes, instead, the BC must be explicitly enforced, as the Dirichlet BC is an *essential* condition in the case of the problem (4.4). See [12] for reference. Reminding that the BCPs are indexed from $L+1$ to N, the Dirichlet BC can be rewritten as

$$\boldsymbol{\Phi}^T(\vec{r}_j)\boldsymbol{a} = \boldsymbol{0} \qquad \text{for } j = L+1,\ldots,N \tag{4.13}$$

By partitioning the vector of the unknowns as follows

$$\boldsymbol{a} = \begin{bmatrix} \boldsymbol{x} \\ \boldsymbol{b} \end{bmatrix} \tag{4.14}$$

where $\boldsymbol{x} = [a_1, a_2, .., a_L]^T$ and $\boldsymbol{b} = [a_{L+1}, a_{L+2}, .., a_N]^T$, equation (4.13) becomes

$$\begin{bmatrix} \boldsymbol{M} & \boldsymbol{N} \end{bmatrix} \begin{bmatrix} \boldsymbol{x} \\ \boldsymbol{b} \end{bmatrix} = \boldsymbol{0} \tag{4.15}$$

where the matrices $\boldsymbol{M}$ and $\boldsymbol{N}$ have been introduced

$$\boldsymbol{M} = \begin{bmatrix} \phi_1(r_{L+1}) & \dots & \phi_L(r_{L+1}) \\ \vdots & \ddots & \vdots \\ \phi_1(r_N) & \dots & \phi_L(r_N) \end{bmatrix} \boldsymbol{N} = \begin{bmatrix} \phi_{L+1}(r_{L+1}) & \dots & \phi_N(r_{L+1}) \\ \vdots & \ddots & \vdots \\ \phi_{L+1}(r_N) & \dots & \phi_N(r_N) \end{bmatrix} \tag{4.16}$$

By defining the embedding matrix $\boldsymbol{E}$

$$\boldsymbol{E} = \begin{bmatrix} \boldsymbol{I} \\ -\boldsymbol{N}^{-1}\boldsymbol{M} \end{bmatrix} \tag{4.17}$$

where $\boldsymbol{I}$ is the $L \times L$ identity matrix, the unknown vector $\boldsymbol{a}$ can be written as a function of $\boldsymbol{x}$

$$\boldsymbol{a} = \boldsymbol{E}\ \boldsymbol{x} \tag{4.18}$$

Note that (4.17) and (4.18) correspond to a change of base.

By embedding the Dirichlet BC (4.18) into the expression(4.8), it is possible to write the functional $I(\Phi)$ as a function of $\boldsymbol{x}$

$$I(\boldsymbol{x}) = \frac{1}{2}\left[\boldsymbol{x}^T\boldsymbol{E}^T(\boldsymbol{X}+\boldsymbol{Y})\boldsymbol{E}\boldsymbol{x} - k^2\boldsymbol{x}^T\boldsymbol{E}^T\boldsymbol{Z}\boldsymbol{E}\boldsymbol{x}\right] \tag{4.19}$$

Deriving, then, equation (4.19) respect to the $\boldsymbol{x}$ to extremize the functional the eigenproblem correspondent to the TM modes is obtained which leads to

$$\underbrace{\boldsymbol{E}^T(\boldsymbol{X}+\boldsymbol{Y})\boldsymbol{E}}_{\boldsymbol{A}}\boldsymbol{x} - k^2\underbrace{\boldsymbol{E}^T\boldsymbol{Z}\boldsymbol{E}}_{\boldsymbol{B}}\boldsymbol{x} = \boldsymbol{0} \tag{4.20}$$

Note that the size of the problem (4.20) has a reduced size respect to the case of the TE modes and in particular $L \times L$.

Briefly the TM modes can be computed by solving the following eigenproblem

$$\boldsymbol{A}\boldsymbol{x} - k^2\boldsymbol{B}\boldsymbol{x} = \boldsymbol{0} \tag{4.21}$$

with dimension $L \times L$ (i.e., the total number of ICPs), where $\boldsymbol{a} = \boldsymbol{E}\ \boldsymbol{x}$ and $\boldsymbol{A}$ and $\boldsymbol{B}$ are always real, symmetric, and non-singular.

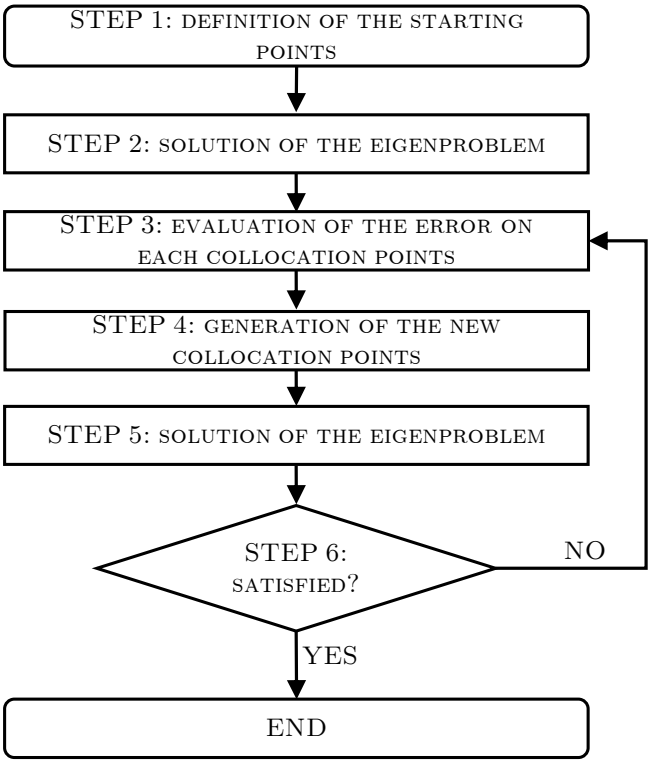

Figure 4.2: © 2018 IEEE–Flowchart of the procedure for the automatic iterative refining algorithm.

4.3 Adaptive Refinement of the Collocation Points

It is well-known in literature that the presence of sharp corners inside the cross-section can originate problems about the convergence of the solution. This aspect has been studied and a series representation of the TE and TM potentials around the singularities have been found(see [13, 14]). In this work this procedure has not been used since its purpose is to demonstrate that the meshless method permits an automatic refinement that does not need the manual intervention over the grid definition. Some articles can be found in the literature that suggest how generate a software based refinement(see [15, 16]). These methods are a good starting point, but present some limitations to point out: *i*) they do not analyze the case of sharp corners; *ii*) they do not explain how to compute the shape parameter and leave this task to the LOOCV algorithm that is time consuming and increases the computational

complexity; *iii*) some of them suggest to minimize a residual error function that depends at least on two parameters that give a weight to the error over the BC (e.g. Neumann) and the one over the Helmholtz equation. The choice of these parameters is suggested on the base of the experimental results obtained, but it is not clear how a change over these values can affect the precision of the algorithm; *iv*) when evaluating the error over Helmholtz and BC equation they do not explain which eigenvalues take into account. The algorithm, presented in this section, has the same steps than [15, 16] but with a different implementation. A qualitative description of it is shown in Fig. 4.2.

4.3.1 Local Definition of the RBFs' Parameters

In [15, 16] the shape parameter is a global value (common to all the RBFs defined over the whole simulated area). This seems not intuitive, as the cross-section under study will present some regions with a more rapid variation of the expected solution. Moreover a generic automatic refinement technique would generate new CPs in proximity of certain regions instead of others. For this reason different density of CPs is expected in different parts of the domain. A global definition of the shape parameter, even if recalculated at every step by the LOOCV algorithms, seems thus questionable.

One of the main contributions of [3] is that, starting from these considerations, it defines a slightly different family of RBFs

$$\phi_i(\vec{r}) = e^{-\chi_i|\vec{r}-\vec{r}_i|^2} \tag{4.22}$$

where, for the i-th RBF, local shape parameter χ_i is

$$\chi_i = \frac{1}{\sigma\lambda_i^2} \tag{4.23}$$

Note that in equation (4.23) a local length λ_i is used instead of the global parameter h, as in the case of (4.7). λ_i will be used during the refinement and its significance will be clear later.

4.3.2 Automatic Refinement Algorithm

The presented algorithm is based on the same steps as [15, 16], but some steps have a different and more general implementation. The procedure is shown in Fig. 4.2, and is discussed in detail as follows:

• *Step 1: Generate the starting CPs and* c_i

For all the CPs, $\lambda_i = h$ where h is found by using (3.7) and $\chi_i = c_i$ where c_i is computed with (4.7) by setting $\sigma = 1$. This choice permits to compute the initial solution without the need of a preconditioning step.

• *Step 2: Find the Starting Solution*
By using the using (4.11) and the (4.20) for the TM and TE modes respectively, the set of the eigenvalues k_m and eigenvectors $\boldsymbol{a}_m = [a_{m,1}, a_{m,2}, \ldots, a_{m,N}]^T$ is found for every m-th mode.

• *Step 3: Evaluation of the error on each CP*
It is well-known that on every ICP, and for every BCP the Helmholtz equation must be satisfied. Moreover, on the BCPs also the the boundary condition is required. So for every j-th CP a total error $\mathcal{E}_j$ is calculated

$$\mathcal{E}_j = \mathcal{H}_j + \begin{cases} \mathcal{B}_j & \text{if } j > L \quad \text{(Boundary Points)} \\ 0 & \text{if } j \leq L \quad \text{(Internal Points)} \end{cases} \tag{4.24}$$

where $\mathcal{H}_j$ is a contribution taking into account the error over the Helmholtz equation (for both the ICPs and the BCPs), while $\mathcal{B}_j$ does it for the boundary condition (for the BCPs).

Consider the case in which the user is interested in evaluating, with a certain degree of accuracy, the first Q modes. In that case it is possible to define $\mathcal{H}_j$ through the following summation

$$\mathcal{H}_j = \sum_{m=1}^{Q} \frac{e^{\mathcal{H}}_{m,j}}{\underset{j}{\text{mean}}\{e^{\mathcal{H}}_{m,j}\}} \qquad j = 1, \ldots, N \tag{4.25}$$

where the contribution of the single eigenmode has been introduced

$$e^{\mathcal{H}}_{m,j} = \left| \sum_{i=1}^{N} a_{m,i} \left[\nabla^2 \phi_i(\rho_j) + k_m^2 \phi_i(\rho_j) \right] \right| \tag{4.26}$$

Note that, to normalize the various contributions in(4.25), every value $e^{\mathcal{H}}_{m,j}$ is weighted by a factor $1/\underset{j}{\text{mean}}\{e^{\mathcal{H}}_{m,j}\}$.

A similar policy has been used to define $\mathcal{B}_j$

$$\mathcal{B}_j = \sum_{m=1}^{Q} \frac{e^{\mathcal{B}}_{m,j}}{\underset{j}{\text{mean}}\{e^{\mathcal{B}}_{m,j}\}} \qquad j = L+1, \ldots, N \tag{4.27}$$

where

$$e^{\mathcal{B}}_{m,j} = \begin{cases} \left| \sum_{i=1}^{N} a_{m,i} \dfrac{\partial \phi_i}{\partial n}(\rho_j) \right| & \text{(TE modes)} \\ \left| \sum_{i=1}^{N} a_{m,i} \phi_i(\rho_j) \right| & \text{(TM modes)} \end{cases} \tag{4.28}$$

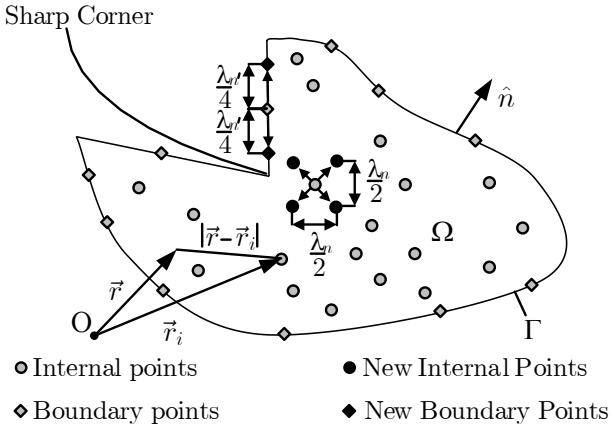

Figure 4.3: © 2018 IEEE–Generation of the new CPs: four new ICPs are generated starting from the n-th ICP, and two new BCPs are generated starting from the n'-th BCP.

Moreover, note that the values $\nabla^2\phi_i(\rho_j)$, $\phi_i(\rho_j)$, and $\frac{\partial\phi_i}{\partial n}(\rho_j)$ can be calculated ones for all at the beginning of the refinement algorithm. They are in fact constant values that do not depend on the solution. Ones they are calculated they can be stored and used at every cycle just reading the memory.

• *Step 4: Generation of the New CPs* From the previous steps, for every CP the total error $\mathcal{E}_j$ is obtained. The refinment procedure is applied to all the CPs which satisfy the following relation

$$\mathcal{E}_j > \alpha \max_i\{\mathcal{E}_i\} \tag{4.29}$$

where $\alpha = 0.5$. The choice of α arbitrary, but has effects on the performance of the algorithm. In particular high values of this parameter will imply the need of more cycles to achieve the wanted level of accuracy, while a low value will make each cycle slower.

Consider the case in which the n'-th BCP satisfies the (4.29). Starting from it, two new boundary collocation points (NBCPs) are generated $\lambda_{n'}/4$ far from it along the direction tangential to the boundary line (see Fig. 4.3). Remember that every point must be associated to a local length and a local shape parameter. In particular if the n'-th boundary point has a local length $\lambda_{n'}$ and a local shape parameter $\chi_{n'}$ it generates two NBCPs with $\lambda = \lambda_{n'}/2$ and $c = 4\ \chi_{n'}$. If, instead, the n-th CP, which satisfy the relation (4.29), is an ICP with a local length λ_n and a local shape parameter χ_n, four NICPs with $\lambda = \lambda_n/2$ and $c = 4\ \chi_n$ are generated from it (see Fig. 4.3). All the new collocation points NCPs (where NCP = NICP ∪ NBCP) wich are generated

outside the domain Ω are discarded. All NCPs are added to the grid, while the CPs correspondent to the added NCPs are eliminated.

• *Step 5: Solution of the eigenproblem.* Same as step 2. This is the most time consuming part as it happens in all the the other methods in which an adaptive procedure can adopted (see [17] for the case of FEM).

• *Step 6: Convergence check*
Calling $k_m^{(p)}$ the wavenumber of the m-th mode at the p-th step ($p = 0$ corresponds to the initial solution) it is possible to compute

$$\mathcal{K}_m^{(p)} = \frac{\left| k_m^{(p)} - k_m^{(p-1)} \right|}{k_m^{(p)}} \tag{4.30}$$

The solution is considered converged when

$$K^{(p)} = \frac{1}{Q} \sum_{m=1}^{Q} \mathcal{K}_m^{(p)} < \beta \ . \tag{4.31}$$

$K^{(p)}$ is called convergence index at the p-th step, while β is a parameter that must be less than 1. Some consideration about its choice will be done in Sec. 4.4.

4.4 Numerical Results

All the simulations described in the following subsections have been conducted with a fixed value of $\sigma = 1$ in (4.7). This demonstrates that no preconditioning is needed, reducing the computation time.

To validate the efficiency and the accuracy of the VMM the results given by this method have been compared with the theoretical values. When no analytical solution was available, instead, the comparison has been done with the results given by ANSYS HFSS as independent validation. HFSS is a commercial software based FEM (see [17]).

4.4.1 Rectangular Waveguide

In this section the proposed algorithm is verified by simulating a WR90 waveguide (rectangular cross-section with dimensions 22.86×10.16 mm^2). Defining $N = 248$ CPs as in Fig. 4.4, the whole simulation requires about 0.47 s to find the TE modes with the result presented in Fig.4.5(a), where the error over the frequency respect the analytical solution is shown in a logarithmic scale. For the TM modes and, again, 248 collocation points the

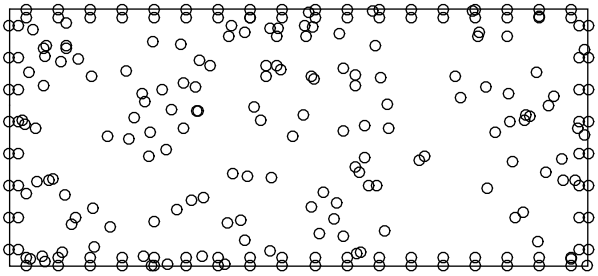

Figure 4.4: © 2018 IEEE–WR90 rectangular waveguide (22.86×10.16 mm^2) and the collocation points used for the analysis by the variational meshless method. Note that the CPs are defined randomly inside the domain (with a uniform distribution) and equidistributed on the boundary.

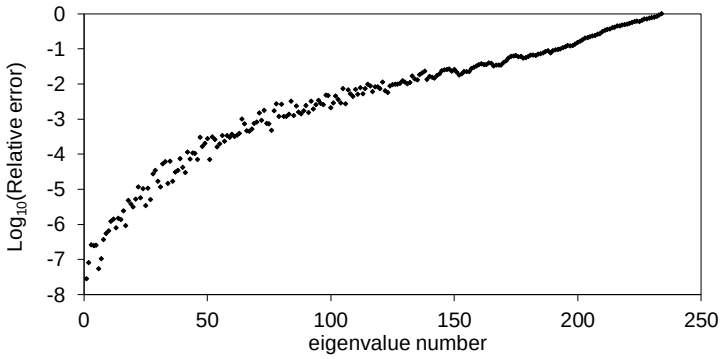

(a)

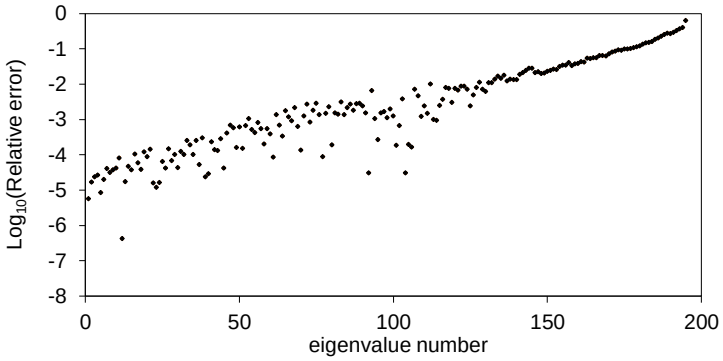

(b)

Figure 4.5: © 2018 IEEE– Error in the calculation of the cut-off frequency of a WR90 rectangular waveguide by the variational meshless method with 248 collocation points: (a) TE modes; (b) TM modes.

simulation time is approximately 0.47 s. and the obtained result is shown in Fig. 4.5(b).

Table 4.1: © 2018 IEEE–Error in the Calculation of the Cutoff Frequencies of the First 5 TE and 5 TM Modes of a WR90 Rectangular Waveguide

Mode	**Analytical** f_c (GHz)	**Meshless Method** f_c (GHz)	**Relative Error** (%)
TE_{10}	6.561679790	6.561679977	0.0000029
TE_{20}	13.123359580	13.123360632	0.0000080
TE_{01}	14.763779527	14.763783394	0.0000262
TE_{11}	16.156262798	16.156266743	0.0000244
TE_{30}	19.685039370	19.685044402	0.0000256
TM_{11}	16.156262798	16.156126299	0.0008449
TM_{21}	19.753271946	19.752746249	0.0002661
TM_{31}	24.606299212	24.605428787	0.0003537
TM_{41}	30.114107202	30.112613561	0.0004960
TM_{12}	30.247849269	30.247498959	0.0001158

Note that 50 TE and 50 TM modes are calculated with an error lower than 0.1%. 121 TE and 112 TM modes were calculated with an accuracy better than 1%, and more than 180 TE and 160 TM modes were calculated with a precision better than 5%. To appreciate the accuracy of the VMM, in Table 4.1 the numerical results are repeated for the first 5 TE and TM modes.

The port-only simulation of the same structure conducted with HFSS required 502 triangles on wave port, and 30 s of total time, to compute just 25 modes between TE and TM.

Note furthermore that in general the number of the TM-modes computed is lower than that of the TE-Modes. This is due to the embedding procedure of (4.20) that reduces the dimension of the eigenproblem from N to L.

To evaluate the precision of the shaping of the obtained potentials a correlation matrix $\boldsymbol{C}$ has been created with indexes m and n, in which it is calculated the integral over the cross section of the product between the m-th potential obtained with the VMM $\Phi_m(x, y)$ and the n-th theoretical potential obtained with the analytical formulas $\Phi_n^A(x, y)$.

$$C_{mn} = \left| \int_\Omega \Phi_m(x, y)\, \Phi_n^A(x, y)\, dS \right| \tag{4.32}$$

The results for the first 5 TE and TM modes are reported in Tab. 4.2. By noting that the desired values should be 1 on the diagonal and 0 otherwise

Table 4.2: © 2018 IEEE–Correlation matrices of the first 5 TE and 5 TM modes of a WR90 rectangular waveguide.

Mode	$\mathbf{TE}_{01}$	$\mathbf{TE}_{20}$	$\mathbf{TE}_{01}$	$\mathbf{TE}_{11}$	$\mathbf{TE}_{30}$
$\mathbf{TE}_{01}$	1	1.6E-07	2.4E-08	1.0E-08	5.9E-08
$\mathbf{TE}_{20}$	1.6E-07	1	3.3E-07	1.5E-07	5.4E-08
$\mathbf{TE}_{01}$	2.4E-08	3.3E-07	1	2.0E-07	3.3E-08
$\mathbf{TE}_{11}$	1.0E-08	1.5E-07	2.0E-07	1	3.8E-07
$\mathbf{TE}_{30}$	5.9E-08	5.4E-08	3.3E-08	3.8E-07	1

Mode	$\mathbf{TM}_{11}$	$\mathbf{TM}_{21}$	$\mathbf{TM}_{31}$	$\mathbf{TM}_{41}$	$\mathbf{TM}_{12}$
$\mathbf{TM}_{11}$	1	6.4E-06	2.1E-06	1.6E-05	8.3E-07
$\mathbf{TM}_{21}$	6.4E-06	1	4.3E-06	3.6E-06	8.7E-06
$\mathbf{TM}_{31}$	2.1E-06	4.3E-06	1	1.7E-05	3.9E-06
$\mathbf{TM}_{41}$	1.5E-05	3.5E-06	1.7E-05	1	1.3E-05
$\mathbf{TM}_{12}$	7.9E-07	8.7E-06	4.0E-06	1.3E-05	1

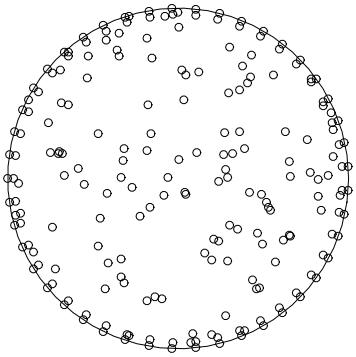

Figure 4.6: © 2018 IEEE– WC25 circular waveguide (radius = 3.175 mm) and the collocation points used for the analysis by the variational meshless method. Note that the CPs are defined randomly inside the domain (with a uniform distribution) and equidistributed on the boundary.

the reader can appreciate a the accuracy of the proposed method. The order of accuracy on the evaluated entries of the correlation matrix over the first 5 TE modes is in the order of $10^{-8} - 10^{-7}$. While for the first 5 TM modes the precision ranges between 10^{-7} and 10^{-5}. The second case has a slightly lower accuracy. It is interesting to note that this level of precision has been achieved with a completely random grid of the ICPs (generated with a uniform distribution).

4.4.2 Circular Waveguide

In this section the proposed algorithm is verified by simulating a WC25 waveguide (circular cross-section with a radius of 3.17 5mm) shown in Fig. 4.6.

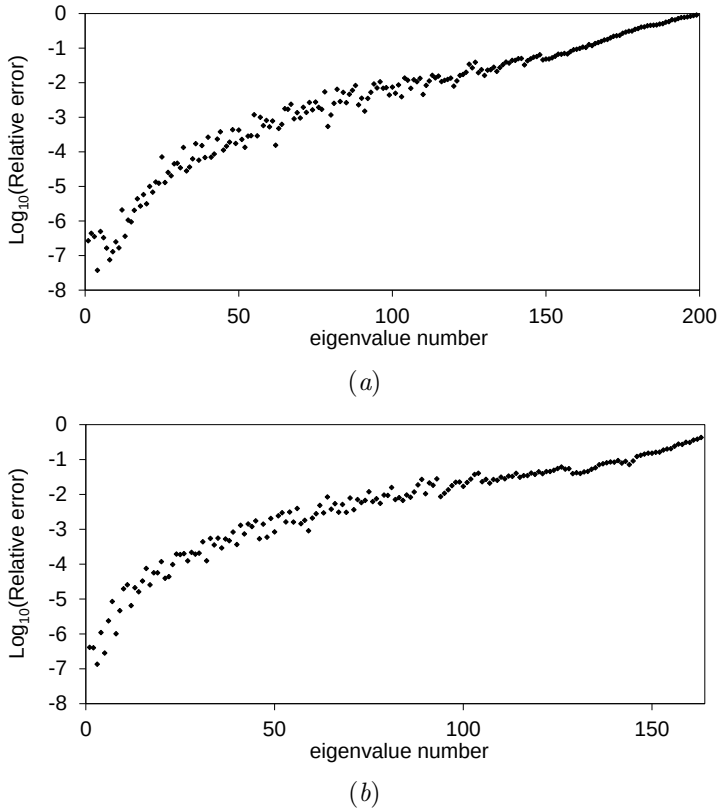

Figure 4.7: © 2018 IEEE– Error in the calculation of the cut-off frequency of a WC25 circular waveguide by the variational meshless method with 210 collocation points: (a) TE modes; (b) TM modes.

The simulation was run on a circular waveguide with an equivalent radius of 3.180166 mm. This is done to avoid the systematic error due to the discretized representation of arcs through a set of nodes. This resize guarantees the same area for the circular domain and the approximated 45-edges polygonal one.

Defining $N = 210$ CPs ($L = 165$ ICPs and $M = 45$ BCPs) as in Fig. 4.6, the whole simulation requires about 0.37 s to find the TE modes with the result presented in Fig.4.7(a). For the TM modes and, again, 210 CPs the simulation time is approximately 0.37 s. and the obtained result is shown in Fig. 4.7(b). It is noted that 105 TE-modes and 82 TM-modes are calculated with an error below 1%. To appreciate the accuracy of the VMM, in Table 4.3 the numerical results are repeated for the first 5 TE and TM modes.

The port-only simulation of the same structure conducted with HFSS required 502 triangles on the wave port, and 60 s of total time, to compute

Table 4.3: © 2018 IEEE–Error in the Calculation of the Cutoff Frequencies of the First 5 TE and 5 TM Modes of a WC25 Circular Waveguide

Mode	**Analytical** f_c (GHz)	**Meshless Method** f_c (GHz)	**Relative Error** (%)
TE_{11}	27.688204719	27.6881968900	0.000028
TE_{11}	27.688204719	27.6881972677	0.000027
TE_{21}	45.930416173	45.9303958628	0.000044
TE_{21}	45.930416173	45.9303998489	0.000035
TE_{01}	57.622199595	57.6222017549	0.000004
TM_{01}	36.164397617	36.1643806256	0.000047
TM_{11}	57.622199587	57.6221758132	0.000041
TM_{11}	57.622199587	57.6221765391	0.000040
TM_{21}	77.230835451	77.2308249923	0.000013
TM_{21}	77.230835451	77.2309199130	0.000109

just 25 modes between TE and TM.

4.4.3 Three-Quarter Circular Waveguide

To test the efficiency of the automatic refinement procedure a third example is considered with a sharp corner. This is the case of the three-quarter

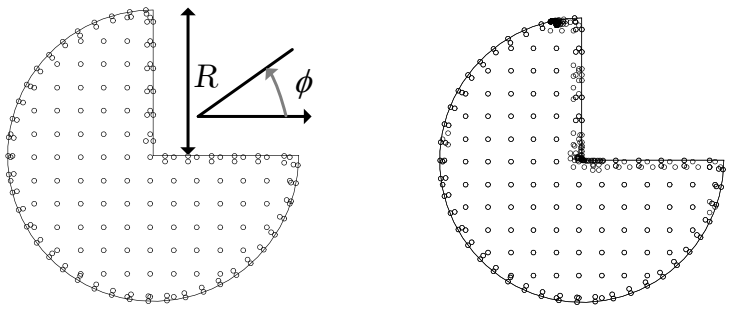

(*a*) (*b*)

Figure 4.8: © 2018 IEEE–Three-quarter circular waveguide ($R = 3.175$ mm) and the collocation points used for the analysis by the variational meshless method. (*a*) Initial configuration with 196 CPs (step 0 of the refinement process). (*b*) Final configuration with 368 CPs (step 9 of the refinement process).

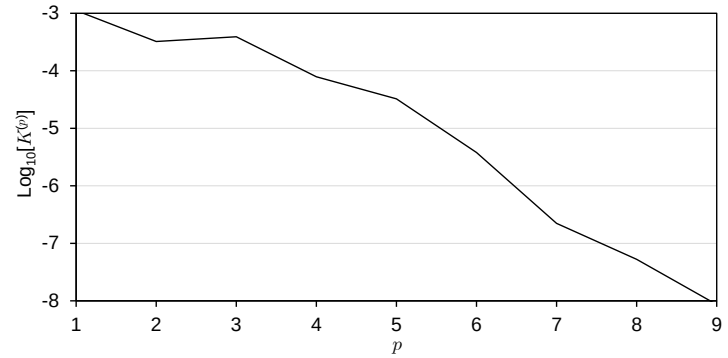

(a)

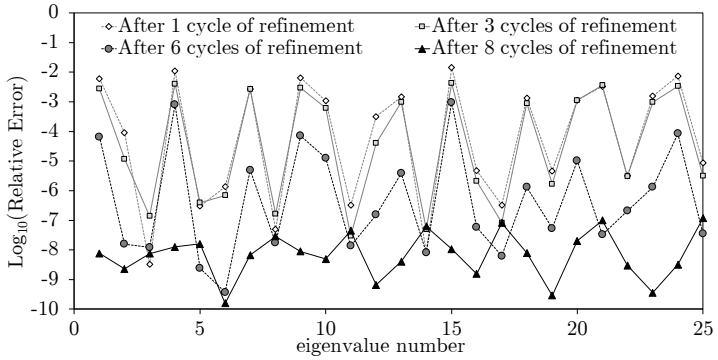

(b)

Figure 4.9: © 2018 IEEE– The refinement process for the analysis of the three-quarter circular waveguide: (*a*) Convergence parameter $K^{(p)}$ vs the refinement step p; (*b*) Evolution of the error of the first 25 modes during the refinement process. The error is calculated considering the values of the step 9 as a reference.

circular waveguide in Fig. 4.8.

The starting grid used to compute the initial solution is shown in Fig. 4.8(*a*) and consists of 196 CPs. After nine refinement cycle the algorithm produced the final grid with 368 CPs shown in Fig. 4.8(*b*). Note that, as expected, the region with higher density of CPs at the end of the refinement is in the proximity of the sharp corner.

The convergence parameter $K^{(p)}$ of equation (4.31) was evaluated on the first $Q = 25$ modes and its variation during the refinement steps is shown in Fig. 4.9(*a*).

In Fig. 4.9(*b*), instead, the error of the first 25 eigenvalues computed during various steps respect to those computed at the 9-th is shown. As can be noted there is an effective convergence. To evaluate the accuracy of the computed modes, their values are reported in Table 4.4 and compared when

Table 4.4: © 2018 IEEE–Cutoff Frequencies f_c After Five Steps of Refinement for the Three-Quarter Circular Waveguide. When Available, the Analytical Results are Used to Calculate the Errors, and the HFSS Results are Given for Comparison.

#	**WC25**	**Meshless Method**		**HFSS**	
	f_c (GHz)	f_c (GHz)	Error %	f_c (GHz)	Error %
1	—	21.0710	—	21.0600	—
2	—	33.9280	—	33.9500	—
3	45.8980 (TE_{21})	45.8967	0.0030	45.9250	0.0586
6	57.5837 (TE_{01})	57.5817	0.0034	57.6125	0.0499
10	77.1785 (TM_{21})	77.1885	0.0128	77.2200	0.0537
11	79.9106 (TE_{41})	79.9073	0.0042	79.9530	0.0530
16	100.779 (TE_{22})	100.777	0.0030	100.835	0.0547
19	105.429 (TE_{02})	105.429	0.0009	105.487	0.0551
32	139.495 (TE_{42})	139.492	0.0022	—	—
34	144.980 (TE_{81})	144.973	0.0046	—	—

possible with the analytical solution. It is noted, in fact, that the modes of a circular waveguide with the same radius and satisfying the electric wall condition at $\phi = 0$ and $\phi = \pi/2$ have the same cutoff frequencies and modal field patterns as their correspondent solutions in the three-quarter waveguide (see Fig. 4.8). All the results were, in any case, compared also with those given by ANSYS HFSS after a port-only simulation with 477 triangles that lasted 40 s of total time to determine 25 modes. Note, in Table 4.4, that after 5 refinement cycles the maximum error over the first 25 modes is achieved in the case of the 10-th mode and is about 0.0128% while $K^{(5)}$ is below 10^{-4}. This suggests that the equation (4.31) is a reasonable policy to evaluate the convergence of the algorithm and that a value of β ranging from 10^{-3} to 10^{-4} can be a good choice.

The VMM required 16 s to compute the initial solution, and to run 5 refinement cycles. After this simulation time, more than 400 modes between TE and TM were computed. The computation time for nine refinement steps was, instead, 50 s.

4.4.4 Double-Ridge Waveguide

The fourth example is the case of the double-ridge waveguide in Fig. 4.10.

The starting grid used to compute the initial solution is shown in Fig. 4.10(a) and consists of 228 CPs. After nine refinement cycle the algorithm produced

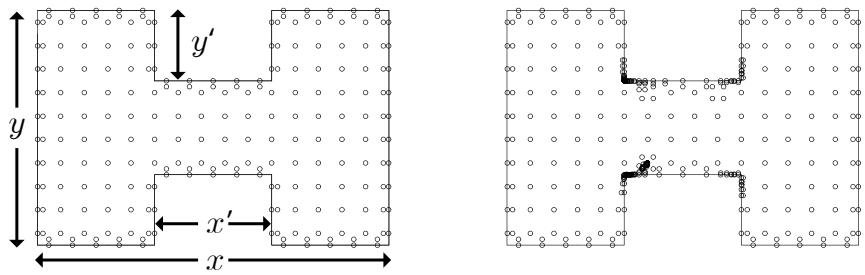

(a) (b)

Figure 4.10: © 2018 IEEE–Double ridge waveguide ($x = 30$ mm, $y = 20$ mm, $x' = 10$ mm, and $y' = 6$ mm) and the collocation points used for the analysis by the variational meshless method. (a) Initial configuration with 228 CPs (step 0 of the refinement process). (b) Final configuration with 469 CPs (step 9 of the refinement process).

the final grid with 469 CPs shown in Fig. 4.8(b). Note that, as expected, the regions with higher density of CPs at the end of the refinement are those in the proximity of the sharp corners.

The convergence parameter $K^{(p)}$ of equation (4.31) was evaluated on the first $Q = 25$ modes and its variation during the refinement steps is shown in Fig. 4.11(a).

Fig. 4.11(b) shows, instead, the error of the first 25 eigenvalues, computed during the various steps, respect to those computed at the 9-th. As can be noted there is an effective convergence of the solutions.

In this case no analytical solution is available. For this reason only the results given by ANSYS HFSS can be used as an interdependent validation. The commercial software was run with a port-only simulation that lasted 57 s and needed 307 triangles on the input port to find all the 25 modes that the program could compute. The comparison between HFSS and the VMM is reported in Tab. 4.5. After the third refinement cycle the difference between the two methods was lower than 0.5% for all the 25 modes taken into account. Note that the results of HFSS cannot be considered as an exact reference, as it clearly resulted from Table 4.4.

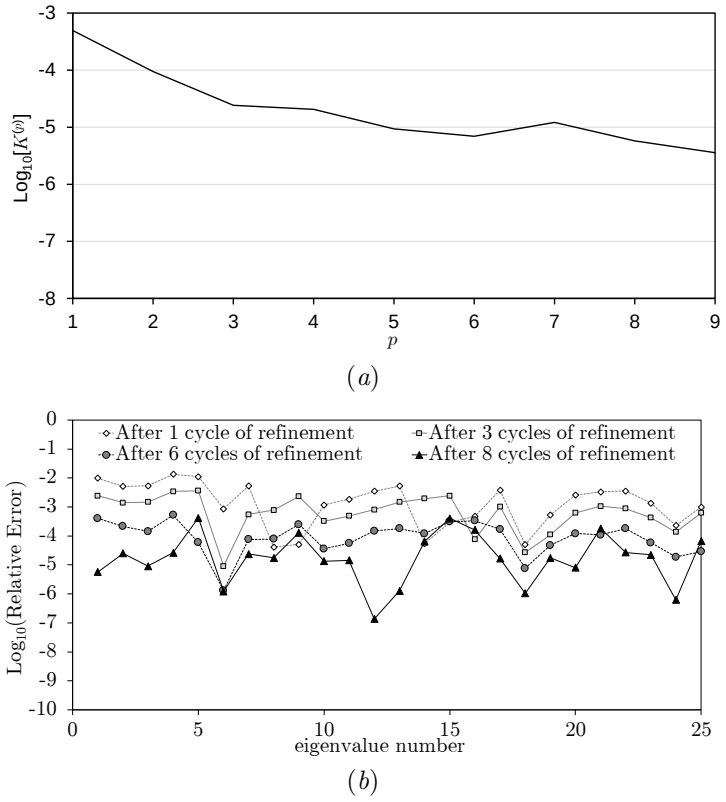

Figure 4.11: © 2018 IEEE– The refinement process for the analysis of the double-ridge waveguide: (a) Convergence parameter $K^{(p)}$ vs the refinement step p; (b) Evolution of the error of the first 25 modes during the refinement process. The error is calculated considering the values of the step 9 as a reference.

The VMM lasted 16 s to define the geometry, calculate the initial solution and run nine refinement cycles. While it required only 2.9 s to simulate until the third cycle.

Table 4.5: © 2018 IEEE–Cutoff Frequencies of the Double-Ridge Waveguide Calculated by the Variational Meshless Method (After Three Refinement Steps) and by HFSS.

#	**Meshless** (GHz)	**HFSS** (GHz)	**Diff.** (%)	#	**Meshless** (GHz)	**HFSS** (GHz)	**Diff.** (%)
1	3.357	3.344	0.39	14	20.942	20.930	0.06
2	7.832	7.814	0.23	15	20.988	20.990	0.01
3	7.854	7.835	0.24	16	20.992	20.990	0.01
4	9.825	9.777	0.49	17	21.062	21.020	0.20
5	14.925	14.940	0.10	18	22.639	22.620	0.08
6	15.000	14.980	0.13	19	22.913	22.880	0.14
7	15.082	15.060	0.15	20	23.603	23.560	0.18
8	15.114	15.090	0.16	21	24.161	24.130	0.13
9	15.189	15.200	0.07	22	26.303	26.250	0.20
10	16.914	16.890	0.14	23	26.391	26.360	0.12
11	17.010	16.980	0.18	24	26.673	26.660	0.05
12	17.635	17.600	0.20	25	27.490	27.500	0.04
13	20.215	20.160	0.27				

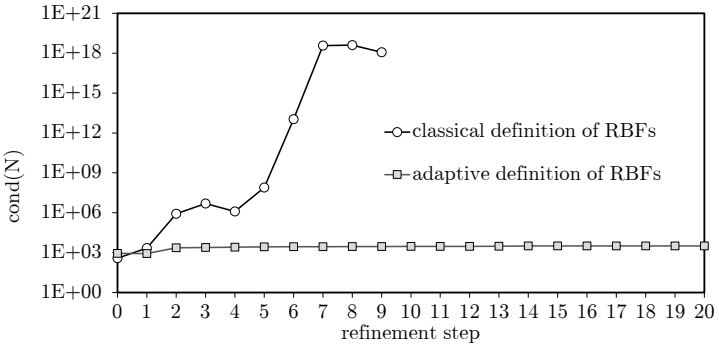

Figure 4.12: © 2018 IEEE– Condition number of N with respect to the inversion vs the refinement step.

4.4.5 Study of the Numerical Stability of the Algorithm

Equations (4.22) and (4.23) give a slightly different definition of the RBFs respect to the classical one. This is done through the local shape parameter χ_i and the local length λ_i.

Thanks to this, the stability of the algorithm during the refinement procedure is improved. In fact, the RBFs centered on the NCPs are stretched

respect to those that generated them. For this reason, when adding new CPs, no correlation occurs due to the proximity of the new defined RBFs and in the various matrices presented in Sec. 4.2.1, Sec. 4.2.2 no similar raws and columns appear.

To appreciate this aspect, the method has been run in the case of the double-ridge waveguide (Fig. 4.10), both using the classical definition of RBFs (3.7)-(4.6) as well as their adaptive definition given by (4.22)-(4.23). The condition number of matrix $\boldsymbol{N}$ with respect to the inversion, computed in (4.17), has been calculated at every refinement step by using the command `cond(`$\boldsymbol{N}$`)` in Matlab.

In Fig. 4.12 the results given by both the adaptive and classical approach are given.

It can be noted that after seven refinement cycles the classical approach exceeds a condition number of 10^{16} and stops working after nine cycles because of the ill-conditioning of $\boldsymbol{N}$. The adaptive approach, instead, permits to keep the condition number constant and thus the problem well-conditioned after an arbitrarily number of cycles and the program never stops running.

This is an interesting result as, at best of our knowledge, in the literature are not found other cases in which after increasing the number of RBFs, the condition number remains constant.

4.5 Conclusion

In this chapter a novel method, wich uses the meshless method in conjunction with the variational technique, has been presented.

All the details of the theory have been given and various examples were used to appreciate its accuracy and the reliability.

An automatic refinement technique was also developed and validated. It is based on a new definition of the RBFs that permits to keep the problem well-conditioned after an arbitrarily number of cycles.

The VMM appears a promising technique to compute an high number of modes with a limited number of unknowns.

In the Chap. 5 an example of application of the VMM is presented. In particular, the the method is used in conjunction to the mode matching technique [18] which can take advantage of the flexibility and the accuracy that the VMM permits.

Bibliography

[1] S. J. Lai and B. Z. Wang, "Solving Helmholtz equation by meshless radial basis functions method," *Progress in Electromagnetics Research B*, Vol. 24, pp. 351–367, 2010.

[2] J. H. Wilkinson, *The algebraic eigenvalue problem*, Vol. 87, Oxford: Clarendon Press, 1965.

[3] V. Lombardi, M. Bozzi, and L. Perregrini, "A novel variational meshless method with radial basis functions for waveguide eigenvalue problems," *IEEE Trans. Microw. Theory Techn.*, Vol. 66, No. 8, pp. 3714-3723, Aug. 2018

[4] M. Mongillo, "Choosing basis functions and shape parameters for radial basis function methods," *SIAM Undergraduate Research Online*, Vol. 4, pp. 190–209, 2011.

[5] T. Kaufmann, C. Engstrröm, and C. Fumeaux, "Adaptive meshless methods in electromagnetic modeling: a gradient-based refinement strategy," in *41th European Microwave Conference (EuMC2011)*, Manchester, UK, Oct 12-14, 2011.

[6] R. E. Collin, *Field Theory of Guided Waves*, 2nd ed., Piscataway, NJ, USA: IEEE Press, 1991.

[7] M. N. O. Sadiku, *Numerical techniques in Electromagnetic*, 2nd ed., CRC press, 2011.

[8] T. Kaufmann, C. Engström, C. Fumeaux, and R. Vahldieck, "Eigenvalue analysis and longtime stability of resonant structures for the meshless radial point interpolation method in time domain," *IEEE Trans. Microw. Theory Techn.*, Vol. 58, No. 12, pp. 3399–3408, Dec. 2010.

[9] V. Lombardi, M. Bozzi, and L. Perregrini, "An Improved Meshless Method for Waveguide Eigenvalue Problems," Vol. 27, No. 12, pp. 1047–1049, Dec. 2017

[10] R. B. Platte and T. A. Driscoll, "Computing eigenmodes of elliptic operators using radial basis functions," *Computers & mathematics with applications*, Vol. 48, No. 3, pp. 561-576, Mar./Apr. 2004.

[11] B. Fornberg, T. A. Driscoll, G. Wrights. and R. Charles, "Observations on the behavior of radial basis function approximations near boundaries," *Computers & Mathematics with Applications*, Vol. 43, No. 3, pp. 473–490, Feb.–Mar 2002.

[12] J. M. Jin, *The Finite Element Method in Electromagnetics*, John Wiley & Sons, 2015.

[13] J. P. Webb, "Finite element analysis of dispersion in waveguides with sharp metal edges," *IEEE Trans. Microw. Theory Techn.*, Vol. 36, No. 12, pp. 1819-1824, Dec. 1988.

[14] M. Bressan and P. Gamba, "Analytical expressions of field singularities at the edge of four right wedges," *IEEE Microwave and Guided Wave Letters*, Vol. 4, No. 1, pp. 3–5, Jan. 1994

[15] T. Kaufmann, C. Engstrröm, and C. Fumeaux, "Adaptive meshless methods in electromagnetic modeling: a gradient-based refinement strategy," in *41th European Microwave Conference (EuMC2011)*, Manchester, UK, Oct 12-14, 2011.

[16] T. Kaufmann, C. Engstrröm, and C. Fumeaux, "Characterization of an adaptive refinement algorithm for a meshless eigenvalue solver based on radial basis functions," in *IEEE Electromagnetic Compatibility Symposium (EMC)*, Melbourne, 2010.

[17] J. Lee, D. Sun and Z. J. Cendes, "Full-wave analysis of dielectric waveguides using tangential vector finite elements," in *IEEE Trans. Microw. Theory Techn.*, Vol. 39, No. 8, pp. 1262-1271, Aug. 1991.

[18] G. Conciauro, M. Guglielmi, and R. Sorrentino, *Advanced Modal Analysis*, John Wiley & Sons LTD, 2000.

Chapter 5

Mode Matching with Variational Meshless Method

5.1 Introduction

As shown in Chap. 3, the VMM appears a useful technique to compute a high number of modes with a relative number of unknowns. Moreover, the new definition of the shape parameter proposed in [1] permits to define the CPs without particular requirements on the spatial regularity. All these advantages seem useful when the VMM is used in conjunction with the mode matching technique (MM) [2, 3] when, in particular, tens or hundreds of modes, computed with an high level of accuracy, are required to calculate the coupling coefficients between two different cross-sections.

In this chapter the theory behind the use of the VMM in conjunction with the MM (MM-VMM) is presented for the particular case of the step junction between two waveguides with different cross-sections.

The theory and the results reported in in the following pages were presented in [4], therefore most of this chapter is based on that paper and will reuse extensively the material of that work.

5.2 Coupling Coefficients Calculation by the Variational Meshless Method

Consider the case of the step junction between two waveguides with different cross-sections and shown in Fig. 5.1.

Inside the q-th waveguide the electromagnetic field is the sum of various

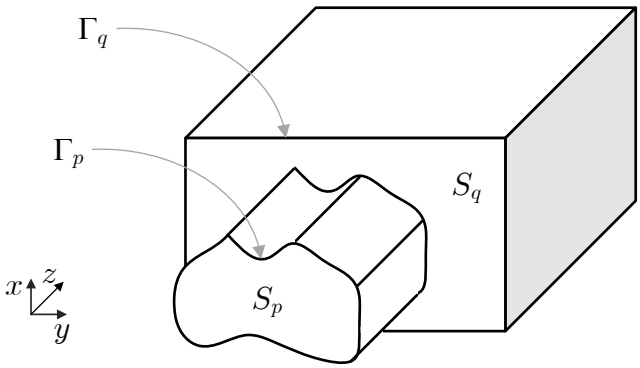

Figure 5.1: © 2019 IEEE– Generic step junction between two hollow waveguides of different cross-section.

contributions given by the solution of the Helmholtz equation with a proper boundary condition (BC) which can be the Neumann BC for the TE modes and the Dirichlet BC for the TM modes [5]

$$\begin{cases} \nabla^2\Phi^{(q)}(\vec{r}) + {k^{(q)}}^2\Phi^{(q)}(\vec{r}) = 0 & \vec{r} \in S_q \\ \dfrac{\partial\Phi^{(q)}(\vec{r})}{\partial n} = 0 \qquad \text{(for TE modes)} & \vec{r} \in \Gamma_q \\ \Phi^{(q)}(\vec{r}) = 0 \qquad \text{(for TM modes)} & \vec{r} \in \Gamma_q \end{cases} \tag{5.1}$$

where S_q and Γ_q are the cross section and the contour of the qth waveguide, respectively (Fig. 5.1), $\hat{n}$ is the outward normal on Γ_q, and $k^{(q)}$ is the wavenumber.

The starting point is the solution of (5.1) by using the VMM presented in [6] and Chap.4. In that case the unknown field patterns $\Phi^{(q)}$ are discretized by using the RBFs as follows

$$\Phi^{(q)}(\vec{r}) = \sum_{i=1}^{N_q} a_i^{(q)} \phi_i^{(q)}(\vec{r}) \tag{5.2}$$

where $\phi_i^{(q)}(\vec{r})$ are the RBFs as defined in [1], $a_i^{(q)}$ is a set of unknown coefficients, and N_q is the number of CPs lying on S_q.

Recall that the VMM solves (5.1) by extremizing the following functional [6]

$$I(\Phi) = \frac{1}{2}\int_{\Omega} \nabla\Phi \cdot \nabla\Phi - k^2\Phi^2 \, dS_q \tag{5.3}$$

This brings to the following matrix eigenproblem

$$\left(\boldsymbol{A}^{(q)} - {\boldsymbol{K}^{(q)}}^2 \boldsymbol{B}^{(q)}\right) \boldsymbol{a}^{(q)} = \boldsymbol{0} \tag{5.4}$$

where $\boldsymbol{A}^{(q)}$ and $\boldsymbol{B}^{(q)}$ are real and symmetric matrices, the diagonal matrix $\boldsymbol{K}^{(q)} = \text{diag}\{k_1^{(q)}, k_2^{(q)}, \ldots, k_{N_q}^{(q)}\}$ has the unknown wavenumbers as entries, and the mth column of $\boldsymbol{a}^{(q)}$, namely $\boldsymbol{a}_m^{(q)} = \left[a_{1,m}^{(q)}, a_{2,m}^{(q)}, \ldots, a_{N_q,m}^{(q)}\right]^T$, is the eigenvector correspondent to $k_m^{(q)}$.

In [3] it is explained how to find, from the solution of (5.4) (i.e., the cut-off wavenumbers $k_m^{(q)}$ and the potentials $\Phi_m^{(q)}(\vec{r})$), the propagation constants β_m of the propagating modes, the attenuation constant α_m of the modes under cut-off, the modal admittances $Y_{c,m}$, and the electric modal fields

$$\vec{e}_m^{(q)} = \begin{cases} \left(\partial_x \Phi_m^{(q)} \hat{x} + \partial_y \Phi_m^{(q)} \hat{y}\right) \times \hat{z} & \text{for TE modes} \\ \left(\partial_x \Phi_m^{(q)} \hat{x} + \partial_y \Phi_m^{(q)} \hat{y}\right) & \text{for TM modes} \end{cases} \tag{5.5}$$

When calculating the admittance and the scattering matrix of a step junction between the qth waveguide with the pth one, as explained in [3, Sec. 3.5 & 3.7], the evaluation of the coupling matrix $\boldsymbol{W}^{(p,q)}$ is required. This quantity has a dimension that varies with the number of modes taken into account in both the waveguides and its entries are

$$\begin{aligned} W_{m,n}^{(p,q)} &= \int_{S_p \cap S_q} \vec{e}_m^{(p)} \vec{e}_n^{(q)} dS \\ &= \begin{cases} C_{m,n}^{x,x} + C_{m,n}^{y,y} & \text{TM mode – TM mode} \\ C_{m,n}^{x,y} - C_{m,n}^{y,x} & \text{TM mode – TE mode} \\ C_{m,n}^{y,y} + C_{m,n}^{x,x} & \text{TE mode – TE mode} \\ C_{m,n}^{y,x} - C_{m,n}^{x,y} & \text{TE mode – TM mode} \end{cases} \end{aligned} \tag{5.6}$$

in which

$$\begin{aligned} C_{m,n}^{\tau,\mu} &= \int_{S_p \cap S_q} \partial_\tau \Phi_m^{(p)} \partial_\mu \Phi_n^{(q)} dS \\ &= \sum_{i=1}^{N_p} \sum_{j=1}^{N_q} a_{i,m}^{(p)} a_{j,n}^{(q)} \int_{S_1 \cap S_2} \partial_\tau \phi_i^{(p)} \partial_\mu \phi_j^{(q)} dS \end{aligned} \tag{5.7}$$

and where ∂_τ stands for partial derivative with respect to the variable $\tau = \{x, y\}$, and N_p and N_q are the number of CPs of the pth and the qth waveguide, respectively. Note that the derivative of the RBFs are known analytically and can be, for this reason, easily computed (see [7]).

5.3 Numerical Results

To validate the efficiency and the accuracy of the MM-VMM the results given by this method have been compared with those obtained by ANSYS HFSS as independent validation.

5.3.1 Step Junction Between Two Rectangular Waveguides

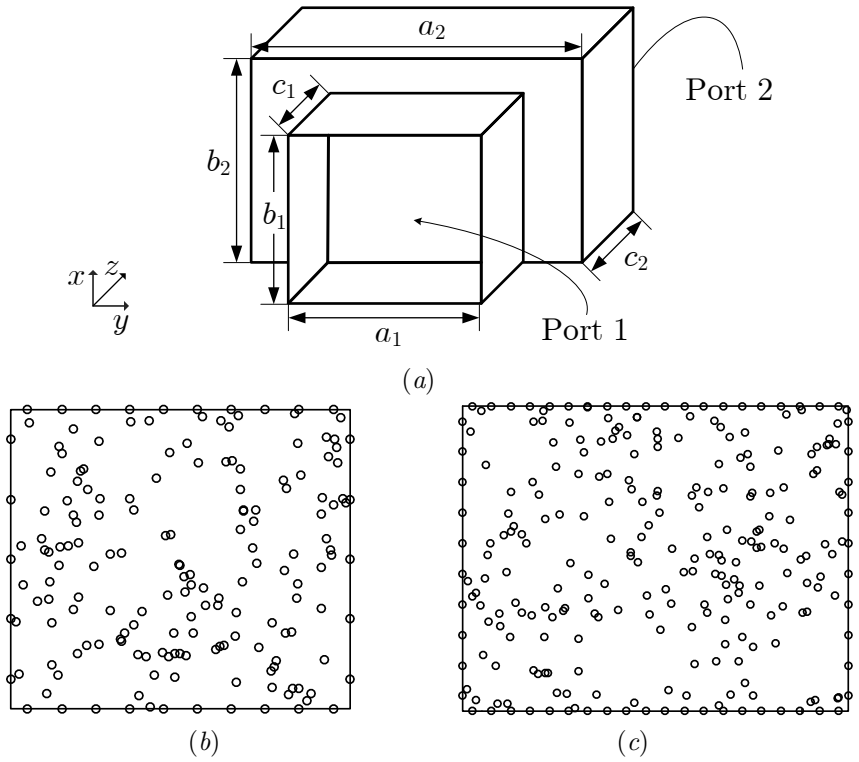

Figure 5.2: © 2019 IEEE– Step junction between two rectangular waveguides: (a) Domain under study ($a_1 = 15.8$ mm, $b_1 = 7.9$ mm, $c_1 = 15.8$ mm, $a_2 = 22.9$ mm, $b_2 = 10.2$ mm, $c_2 = 22.9$ mm); (b) Position of the CPs in the small rectangular cross-section; (c) Position of the CPs in the big rectangular cross-section.

Consider the step junction in Fig. 5.2(a) between two different rectangular waveguides. This example is taken from the literature [8].

First of all the VMM has been applied to the two waveguides separately and then the MM technique has been used to evaluate the whole response of the topology. The code used 174 CPs (i.e., 174 unknowns) on the small

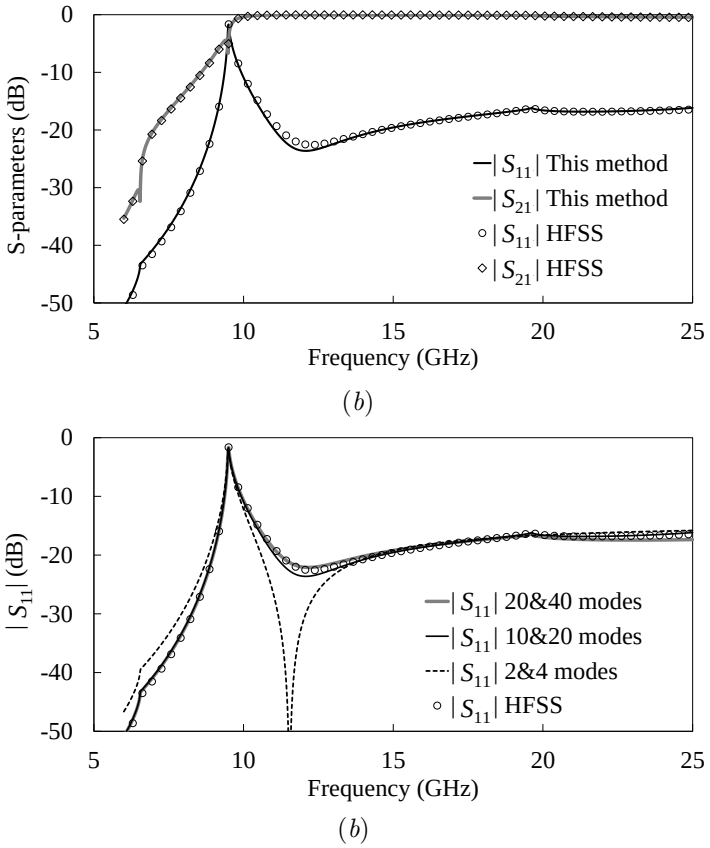

Figure 5.3: © 2019 IEEE– Step junction between two rectangular waveguides: (a) Comparison between HFSS and this method in the evaluation of $|S_{11}|$ and $|S_{21}|$; (b) Convergence analysis of the MM-VMM when varying the number of modes considered in the two waveguides;

waveguide, and 260 CPs on the big one. See Fig. 5.2(b) and Fig. 5.2(c) respectively. The VMM did not need to refine the solution through any refinement technique (see [6]).

In Fig. 5.3(a) the obtained response in frequency of the S parameters is shown. The simulation was run by considering 10 modes on the small waveguide and 20 modes on the larger one and 951 points in frequency (ranging from 6 GHz to 25 GHz) were evaluated.

The simulation lasted 1.51 s to compute the modal fields and the coupling coefficients, and 0.47 s to compute the cascade for all the frequency points.

In Fig. 5.3(a) there is also a comparison between the results obtained with the MM-VMM and those given by ANSYS HFSS after a simulation that needed 30536 tetrahedra, 309 triangles on the input port and 356 triangles on the output one.

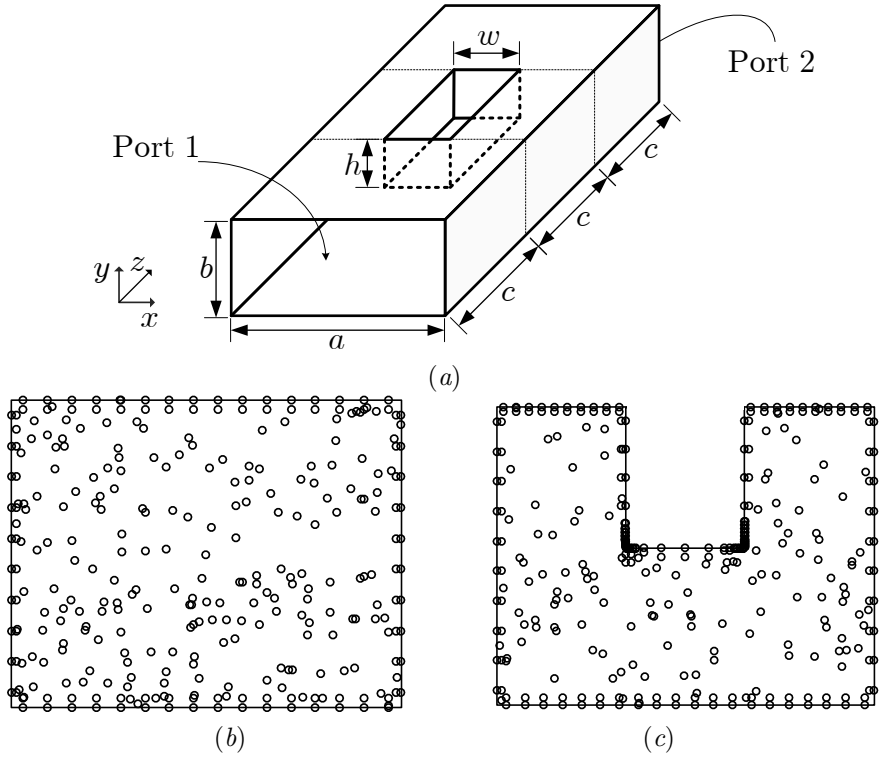

Figure 5.4: © 2019 IEEE– Waveguide component comprising two step junctions between a rectangular and a ridge waveguide: (*a*) Domain under study (a = 19.05 mm, b = 9.525 mm, c = 20 mm, w = 6 mm, h = 4.5 mm); (*b*) Position of the CPs in the rectangular cross-section; (*c*) Position of the CPs in the ridge cross-section after the automatic refinement.

In Fig. 5.3(a) a convergence study is reported which plots the obtained S_{11} taking into account different numbers of modes in both the waveguides. Note that 10&20 modes seem enough to consider the method convergent.

5.3.2 Step Junction Discontinuity in a Rectangular Waveguide

Consider the topology shown in Fig. 5.4(a) and presented in [9]. It consists in the cascade of two rectangular and a ridge waveguides .

Both the input and output rectangular waveguides were analyzed by using 304 randomly distributed CPs [as shown in Fig. 5.4(b)]. The ridge, instead, was analyzed by using the automatic refinement technique presented in [6] because of the presence of two sharp corners. Starting from 281 CPs, after 4

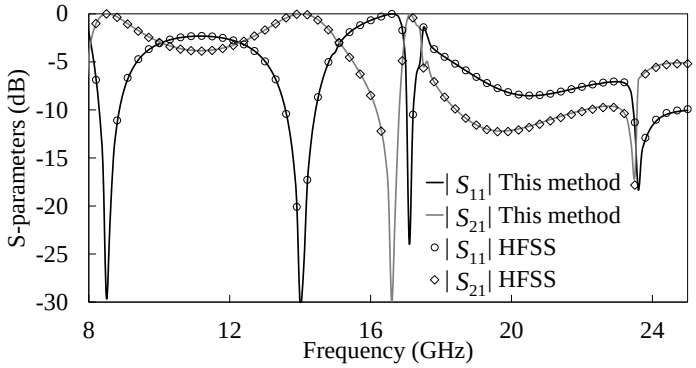

Figure 5.5: © 2019 IEEE– Comparison between HFSS and this method in the evaluation of the $|S_{11}|$ and $|S_{21}|$ in the case of Fig. 5.4.

cycles of refinement, the procedure led to the 341 CPs shown in Fig. 5.4(c), with an higher density of the CPs in proximity of the critical region where the potential presents more rapid variations.

In Fig. 5.5 the frequency obtained response of the S parameters is shown. The simulation was run by considering 97 modes on the rectangular waveguides and 82 modes on the ridge one and 201 points in frequency (ranging from 8 GHz to 25 GHz) were evaluated.

The simulation lasted 8.01 s to compute the modal fields and the coupling coefficients, and 4.57 s to compute the cascade for all the frequency points.

In Fig. 5.5 there is also a comparison between the results obtained with the MM-VMM and those given by ANSYS HFSS after a simulation that needed 40367 tetrahedra, 319 triangles on the input and 328 triangles on the output port.

5.4 Conclusion

In this chapter the VMM has been used in conjunction with the MM technique (MM-VMM). This last one can take advantage of the flexibility that the VMM permits in the definition of the CPs and the high number of modes that it can compute with a limited number of unknowns. Two examples were used to demonstrate the efficiency and the accuracy of the method.

Bibliography

[1] V. Lombardi, M. Bozzi, and L. Perregrini, "An improved meshless method for waveguide eigenvalue problems," *IEEE Microw. Compon. Lett.*, Vol. 27, No. 12, pp. 1047–1049, Dec. 2017

[2] F. Alessandri, G. Bartolucci, and R. Sorrentino, "Admittance matrix formulation of waveguide discontinuity problems: Computer-aided design of branch guide directional couplers," *IEEE Trans. Microw. Theory Techn.*, Vol. 36, pp. 394-403, Feb. 1988.

[3] G. Conciauro, M. Guglielmi, and R. Sorrentino, *Advanced Modal Analysis*, John Wiley & Sons LTD, 2000.

[4] V. Lombardi, M. Bozzi, and L. Perregrini, "Mode Matching Analysis of Waveguide Components Exploiting the Variational Meshless Method," *IEEE Microw. Compon. Lett.*, Vol. 29, No. 10, pp. 631-633, Oct. 2019

[5] R. E. Collin, *Field Theory of Guided Waves*, 2nd ed., Piscataway, NJ, USA: IEEE Press, 1991.

[6] V. Lombardi, M. Bozzi, and L. Perregrini, "A novel variational meshless method with radial basis functions for waveguide eigenvalue problems," *IEEE Trans. Microw. Theory Techn.*, Vol. 66, No. 8, pp. 3714-3723, Aug. 2018

[7] G. E. Fasshauer, *Meshfree approximation methods with MATLAB*, Vol. 6, Chicago,: World Scientific, 2007.

[8] K. Ise, K. Inoue and M. Koshiba, "Three-dimensional finite-element method with edge elements for electromagnetic waveguide discontinuities," *IEEE Trans. Microw. Theory Techn.*, Vol. 39, No. 8, pp. 1289-1295, Aug. 1991

[9] D. Arena, M. Ludovico, G. Manara and A. Monorchio, "Analysis of waveguide discontinuities using edge elements in a hybrid mode matching/finite elements approach," *IEEE Microw. Compon. Lett.*, Vol. 11, No. 9, pp. 379-381, Sept. 2001

Chapter 6

The Variational Meshless Method for Inhomogeneous Waveguides

6.1 Introduction

In the previous chapter, VMM [1] has been presented and applied to the eigenmode analysis of a shielded waveguide with a general shape and filled with a homogeneous media. In this case it is possible to represent the electromagnetic field as a combination of TE and TM modes, and the simulation is reduced to the solution of two scalar problems (one for the TE modes and the other for the TM ones) [2]. In particular the analysis consists in the solution of the scalar Helmholtz equation with a proper BC.

In this chapter a different problem will be considered and its treatment will need an extension of the theory. It is the evaluation of the dispersion diagram of the modes propagating inside a shielded waveguide filled with an inhomogeneous media.

As explained in [3], in fact, this will require the solution of a vector problem and in particular the Vector Helmholtz equation with a proper BC.

When dealing with this kind of problem it is possible to use the magnetic field or the electric field as working variable. Both approaches are in principle equivalent. In this work the magnetic field is used to define the problem as this vector quantity is continuous inside the regions with inhomogeneous dielectrics.

In this chapter all the theory is presented and some implementation aspects are also discussed.

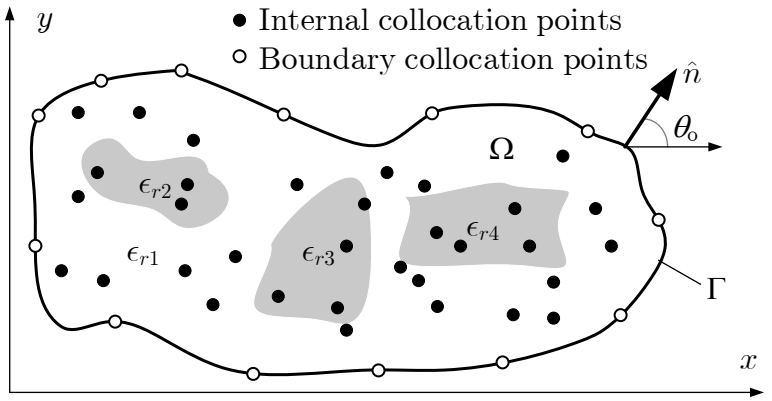

Figure 6.1: © 2019 IEEE– Geometry of the cross-section of an arbitrarily shaped waveguide including different dielectric materials. The CPs where the RBFs are centered are grouped into internal CPs and boundary CPs.

It will be possible to appreciate as, also in the case of the vector representation of the fields, the VMM requires a significantly lower number of unknowns than FEM to reach the same level of accuracy.

Some numerical results will be shown to validate the theory. The method can also be improved by exploiting the geometrical symmetries when possible. This aspect is analyzed in Chap. 7.

The theory and the results reported in in the following pages were presented in [4], therefore most of this chapter is based on that paper and will reuse extensively the material of that work.

6.2 Theory

6.2.1 Starting Problem

In Fig. 6.1 an inhomogeneous waveguide shielded by a perfect conductor and with cross-section Ω and boundary Γ is shown.

The aim of this work is the evaluation of the dispersion digram of the modes propagating inside it [2]. They will present a propagation along z which is the direction normal to the cross-section and can be written as $\vec{H}(x, y, z) = \vec{h}(x, y)\, \mathrm{e}^{-j\beta z}$ where j here is the imaginary unit (see [2] for instance).

The vector wave equation (i.e. the Helmholtz equation) can be imposed by assuming this dependence on the x,y, and z coordinates.

The dispersion diagram can be computed by setting the value of β and finding the wavenumber correspondent to each mode [3].

Beside the Helmholtz equation, both the divergence condition (DC) and the BC (which is the electric wall condition) must be imposed to avoid the computation of some spurious solution [3, 5]. For this reason the problem will be completely represented by the following set of equations

$$\nabla \times \left(\frac{1}{\epsilon_r} \nabla \times \vec{H}(x,y,z) \right) - k_0^2 \mu_r \vec{H}(x,y,z) = 0 \quad \text{in } \Omega \tag{6.1}$$

$$\nabla \cdot \vec{H} = 0 \quad \text{in } \Omega \tag{6.2}$$

$$\hat{n} \cdot \vec{H}(x,y,z) = 0 \quad \text{on } \Gamma \tag{6.3}$$

where $k_0 = 2\pi f \sqrt{\mu_0 \epsilon_0}$ is the wavenumber in vacuum, f is the frequency, μ_0 is the vacuum permeability, ϵ_0 is the vacuum permittivity, and $\hat{n}$ is the outward normal on Γ (see Fig. 6.1). As explained in [3], the problem (6.1) has an equivalent variational formulation

$$F(\vec{H}) = \frac{1}{2} \int_\Omega \left(\frac{1}{\epsilon_r} \nabla \times \vec{H} \cdot \nabla \times \vec{H} - k_0^2 \mu_r \vec{H} \cdot \vec{H} \right) d\Omega \tag{6.4}$$

and the solution to the equation (6.1) can be found by rendering stationary this functional. While the DC and the BC have to be enforced explicitly.

Note that adopting the electric field as working variable, also the normal component discontinuity should have been enforced at the material interfaces.

6.2.2 RBF Approximation

To discretize the problem the RBF approximation is used, as done in the previous chapter. In this case the vector magnetic field is decomposed as in [3]

$$\vec{H}(x,y,z) = \left[\hat{x} H^x(x,y) + \hat{y} H^y(x,y) + j \hat{z} H^z(x,y) \right] e^{-j\beta z} \ . \tag{6.5}$$

Note that that the z-component of the field is jH^z. This is done to keep the resulting eigenproblem real after all the algebric manipulations that are needed to complete this task.

Ones the CPs are defined (as in Fig. 6.1) every component of the magnetic field can be approximated by using the RBFs in a similar way than the previous chapter. In particular, by defining $h_i^\tau(x,y)$ the RBF centered in the i-th CP, with $\tau = x, y, z$, the component along the direction τ can be written as

$$H^\tau(x,y) = \sum_{i=1}^{N} a_i^\tau h_i^\tau(x,y) \tag{6.6}$$

Where N is the total number of CPs defined on the cross-section. Beside them, L are the ICPs and $M = N - L$ are the BCPs, as shown in Fig. 6.1.

The Gaussian RBFs are used as in the case of the homogeneous structures

$$h_i^\tau(x, y) = e^{-\xi_i^\tau c_i \left[(x-x_i)^2+(y-y_i)^2\right]} \tag{6.7}$$

where (x_i, y_i) is the position of the i-th CP and the shape parameter c_i is defined as in (4.7).

Note that the Gaussian RBFs (6.7) are C^∞, and this allows a simple treatment during their differentiation.

6.3 Numerical Implementation

6.3.1 Matrix Representation of the Variational Problem

Substituting (6.5) and (6.6) into (6.4), the following matrix expression is obtained

$$F(\boldsymbol{a}) = \frac{1}{2}\left[\boldsymbol{a}^T \boldsymbol{C} \boldsymbol{a} - k^2 \boldsymbol{a}^T \boldsymbol{T} \boldsymbol{a}\right] \tag{6.8}$$

where the unknown vector $\boldsymbol{a}$ has been introduced

$$\boldsymbol{a} = [a_1^x, a_2^x, \ldots, a_N^x, a_1^y, a_2^y, \ldots, a_N^y, a_1^z, a_2^z, \ldots, a_N^z]^T \tag{6.9}$$

and the matrices $\boldsymbol{C}$ and $\boldsymbol{T}$ can be partitioned as follows

$$\boldsymbol{C} = \begin{bmatrix} \boldsymbol{C}_{11} & \boldsymbol{C}_{12} & \boldsymbol{C}_{13} \\ \boldsymbol{C}_{12}^T & \boldsymbol{C}_{22} & \boldsymbol{C}_{23} \\ \boldsymbol{C}_{13}^T & \boldsymbol{C}_{23}^T & \boldsymbol{C}_{33} \end{bmatrix} \quad \boldsymbol{T} = \begin{bmatrix} \boldsymbol{T}_{11} & \boldsymbol{0} & \boldsymbol{0} \\ \boldsymbol{0} & \boldsymbol{T}_{22} & \boldsymbol{0} \\ \boldsymbol{0} & \boldsymbol{0} & \boldsymbol{T}_{33} \end{bmatrix} \tag{6.10}$$

All the matrices $\boldsymbol{C}_{\alpha\beta}$ and $\boldsymbol{T}_{\alpha\beta}$ in (6.10) are $N \times N$ and their entries are

$$\begin{aligned}
\boldsymbol{C}_{11}(i,j) &= + \int_\Omega \frac{1}{\epsilon_r} \frac{\partial h_j^x}{\partial y} \frac{\partial h_i^x}{\partial y} d\Omega + \beta^2 \int_\Omega \frac{1}{\epsilon_r} h_j^x h_i^x d\Omega \\
\boldsymbol{C}_{22}(i,j) &= + \int_\Omega \frac{1}{\epsilon_r} \frac{\partial h_j^y}{\partial x} \frac{\partial h_i^y}{\partial x} d\Omega + \beta^2 \int_\Omega \frac{1}{\epsilon_r} h_j^y h_i^y d\Omega \\
\boldsymbol{C}_{33}(i,j) &= + \int_\Omega \frac{1}{\epsilon_r} \left(\frac{\partial h_j^z}{\partial x} \frac{\partial h_i^z}{\partial x} + \frac{\partial h_j^z}{\partial y} \frac{\partial h_i^z}{\partial y} \right) d\Omega \\
\boldsymbol{C}_{12}(i,j) &= - \int_\Omega \frac{1}{\epsilon_r} \frac{\partial h_j^x}{\partial y} \frac{\partial h_i^y}{\partial x} d\Omega \\
\boldsymbol{C}_{13}(i,j) &= +\beta \int_\Omega \frac{1}{\epsilon_r} \frac{\partial h_j^z}{\partial x} h_i^x d\Omega \\
\boldsymbol{C}_{23}(i,j) &= +\beta \int_\Omega \frac{1}{\epsilon_r} \frac{\partial h_j^z}{\partial y} h_i^y d\Omega \\
\boldsymbol{T}_{11}(i,j) &= + \int_\Omega \mu_r h_j^x h_i^x d\Omega \\
\boldsymbol{T}_{22}(i,j) &= + \int_\Omega \mu_r h_j^y h_i^y d\Omega \\
\boldsymbol{T}_{33}(i,j) &= + \int_\Omega \mu_r h_j^z h_i^z d\Omega
\end{aligned} \tag{6.11}$$

Note that, thanks to the variational technique, the problem has been relaxed of one degree over the derivative order which is now less or equal to 1 instead of 2 as in the case of the Helmholtz equation (6.1). Moreover the derivative can be calculated analytically as the discretization is dealing with RBFs. In particular

$$\begin{aligned}
\frac{\partial h_i^\tau}{\partial x}(x,y) &= -2\xi_i^\tau c(x - x_i) h_i^\tau(x,y) \\
\frac{\partial h_i^\tau}{\partial y}(x,y) &= -2\xi_i^\tau c(y - y_i) h_i^\tau(x,y)
\end{aligned} \tag{6.12}$$

Note that that $\boldsymbol{C}$ *and* $\boldsymbol{T}$ *are real, symmetric, and nonsingular.* Moreover, there is not dependence on β in the case of the marix $\boldsymbol{T}$, while in the case of matrix $\boldsymbol{C}$ it is possible to write

$$\boldsymbol{C} = \boldsymbol{C}_0 + \beta \boldsymbol{C}_1 + \beta^2 \boldsymbol{C}_2 \tag{6.13}$$

where $\boldsymbol{C}_0$, $\boldsymbol{C}_1$, $\boldsymbol{C}_2$ are also β-independent.

6.3.2 Matrix Representation of the Divergence Condition

Substituting (6.5) and (6.6) into (6.2), the following matrix expression is derived

$$\nabla \cdot \vec{H} = \sum_{i=1}^{N} a_i^x \frac{\partial h_i^x}{\partial x} + \sum_{i=1}^{N} a_i^y \frac{\partial h_i^y}{\partial x} + \beta \sum_{i=1}^{N} a_i^z h_i^z \tag{6.14}$$

and applying the Method of Moments (MoM) and using h_j^z as test functions, this brings to

$$\boldsymbol{D}\boldsymbol{a} = \boldsymbol{0} \tag{6.15}$$

which can be partitioned as

$$\boldsymbol{D} = \begin{bmatrix} \boldsymbol{D}_{11} & \boldsymbol{D}_{12} & \boldsymbol{D}_{13} \end{bmatrix} \tag{6.16}$$

and the $\boldsymbol{D}_{\alpha\beta}$ are all $N \times N$ matrices with the following entries

$$\begin{aligned} \boldsymbol{D}_{11}(i,j) &= \int_\Omega h_j^z \, \frac{\partial h_i^x}{\partial x} d\Omega \\ \boldsymbol{D}_{12}(i,j) &= \int_\Omega h_j^z \, \frac{\partial h_i^y}{\partial y} d\Omega \\ \boldsymbol{D}_{13}(i,j) &= \beta \int_\Omega h_j^z \, h_i^z d\Omega \end{aligned} \tag{6.17}$$

Note that matrix $\boldsymbol{D}$ has dimension $N \times 3N$ and, thus, has a *nullity* of $2N$.

Also in this case it is possible to write $\boldsymbol{D}$ as a matrix polynomial of β

$$\boldsymbol{D} = \boldsymbol{D}_0 + \beta \boldsymbol{D}_1 \tag{6.18}$$

where $\boldsymbol{D}_0$, and $\boldsymbol{D}_1$ are both β-independent.

6.3.3 Matrix Representation of the Boundary Condition

Substituting (6.5) and (6.6) in (6.3), applying the MoM procedure on the boundary Γ, and using the h_j^z centered on the BCPs, as test functions, the following matrix equation is obtained

$$\boldsymbol{B}\boldsymbol{a} = \boldsymbol{0} \tag{6.19}$$

which can be partitioned as

$$\boldsymbol{B} = \begin{bmatrix} \boldsymbol{B}_{11} & \boldsymbol{B}_{12} & \boldsymbol{0} \end{bmatrix} \tag{6.20}$$

where $\mathbf{0}$ is the $M \times N$ null matrix and $\boldsymbol{B}_{\alpha\beta}$ are $M \times N$ matrices, and their expressions are

$$\begin{aligned} \boldsymbol{B}_{11}(i,j) &= \int_\Gamma \cos(\theta_o) \left[h_j^z(x_o, y_o) h_i^x(x_o, y_o) \right] dl \\ \boldsymbol{B}_{12}(i,j) &= \int_\Gamma \sin(\theta_o) \left[h_j^z(x_o, y_o) h_i^y(x_o, y_o) \right] dl \end{aligned} \tag{6.21}$$

where θ_o is the angle between $\hat{n}$ and $\hat{x}$ on the boundary observation point (x_o, y_o) as shown in Fig. 6.1. Note that the matrix $\boldsymbol{B}$ is β-independent.

6.3.4 Final Eigenproblem

Beside the equation (6.10), the DC and BC must be imposed. This reduces the degrees of freedom associated to the vector $\boldsymbol{a}$. This last one, in fact, must lie in the null space of $\boldsymbol{D}$ (see (6.15)). This implies that

$$\boldsymbol{a} = \boldsymbol{E}_D \boldsymbol{x} \tag{6.22}$$

where $\boldsymbol{x}$ is a $2N \times 1$ unknown vector and $\boldsymbol{E}_D$ is a $3N \times 2N$ matrix which is an orthonormal basis for the null space of $\boldsymbol{D}$ obtained with the singular value decomposition (SVD). Note that the computational complexity of the SVD, for an $n \times m$ matrix, is $\mathcal{O}\left(\min(nm^2, mn^2)\right)$ [6]. For this reason its application to the matrix $\boldsymbol{D}$ has a cost of $\mathcal{O}\left(3\ N^3\right)$.

The equation (6.22) can be substituted in (6.19) obtaining

$$\boldsymbol{x} = \boldsymbol{E}_B \boldsymbol{z} \tag{6.23}$$

where $\boldsymbol{z}$ is an unknown vector and $\boldsymbol{E}_B$ is an orthonormal basis for the null space of $\boldsymbol{B}\boldsymbol{E}_D$, also obtained with the SVD algorithm. The *rank* of $\boldsymbol{B}$ is M, the dimension of $\boldsymbol{E}_B$ is $2N \times (N + L)$, and $\boldsymbol{z}$ is an $(N + L) \times 1$ vector.

After combining (6.23) and (6.22) in (6.8) and extremizing the resulting expression by deriving respect to the unknown vector $\boldsymbol{z}$ (as was done in the previous chapter), the following eigensystem is obtained

$$\boldsymbol{C'}(\beta)\boldsymbol{z} = k_0^2 \boldsymbol{T'}(\beta)\boldsymbol{z} \tag{6.24}$$

in which the mass and stiffness matrices are

$$\begin{aligned} \boldsymbol{C'}(\beta) &= \boldsymbol{E}_B^T \boldsymbol{E}_D^T \boldsymbol{C} \boldsymbol{E}_D \boldsymbol{E}_B \\ \boldsymbol{T'}(\beta) &= \boldsymbol{E}_B^T \boldsymbol{E}_D^T \boldsymbol{T} \boldsymbol{E}_D \boldsymbol{E}_B \end{aligned} \tag{6.25}$$

The solution of (6.24) permits to find the vector $\boldsymbol{z}$ and, thus, the starting unknown through the following change of base

$$\boldsymbol{a} = (\boldsymbol{E}_D \boldsymbol{E}_B)\, \boldsymbol{z} \tag{6.26}$$

Note that $\boldsymbol{C'}$ and $\boldsymbol{T'}$ are real, symmetric, and nonsingular, thus leading to a well-conditioned eigenproblem [7] and that the dimension of the problem (6.24) is $(N + L) \times (N + L)$ instead of $3N \times 3N$.

Note that the matrices $\boldsymbol{C'}$ and $\boldsymbol{T'}$ are both dependent on β. As the aim of this work is to find the dispersion diagram of the generic i-th mode propagating in the waveguide under study, the pair $\{\beta, k_0^{(i)}\}$ (and, therefore, $\{\beta, \omega^{(i)}\}$ is the solution to find. For this reason the developed software will solve the problem (6.24) for various values of β.

6.3.5 Implementation of the Algorithm

In Fig. 6.2 the algorithm based on the theory of this section in shown. It has been implemented in a Matlab code that receives, as input, the geometry the properties of the materials and the Q values of β to evaluate which are ordered as $(\beta_1, \ldots, \beta_Q)$.

The steps are briefly summarized:

- the CPs are defined on the domain with a higher density in the regions with higher dielectric constant. More in detail, the definition of the average distance h in (3.7) is locally modified dividing it by a factor $\sqrt{\epsilon_r}$, and new CPs are added following the procedure described in [1];

- the β-independent matrices $\boldsymbol{T}$ and $\boldsymbol{B}$, $\boldsymbol{C}_0$, $\boldsymbol{C}_1$, $\boldsymbol{C}_2$, $\boldsymbol{D}_0$, and $\boldsymbol{D}_1$ are evaluated;

- a loop on the β values starts, generating the β-dependent matrices $\boldsymbol{C}$, $\boldsymbol{D}$, and $\boldsymbol{E}_D$ and than assembling the eigenproblem (6.24) through (6.25);

- the eigenproblem is solved computing the wavenumbers of the first modes for that particular value of β.

The β-loop stops when all the β values have been considered and the dispersion diagram is plotted.

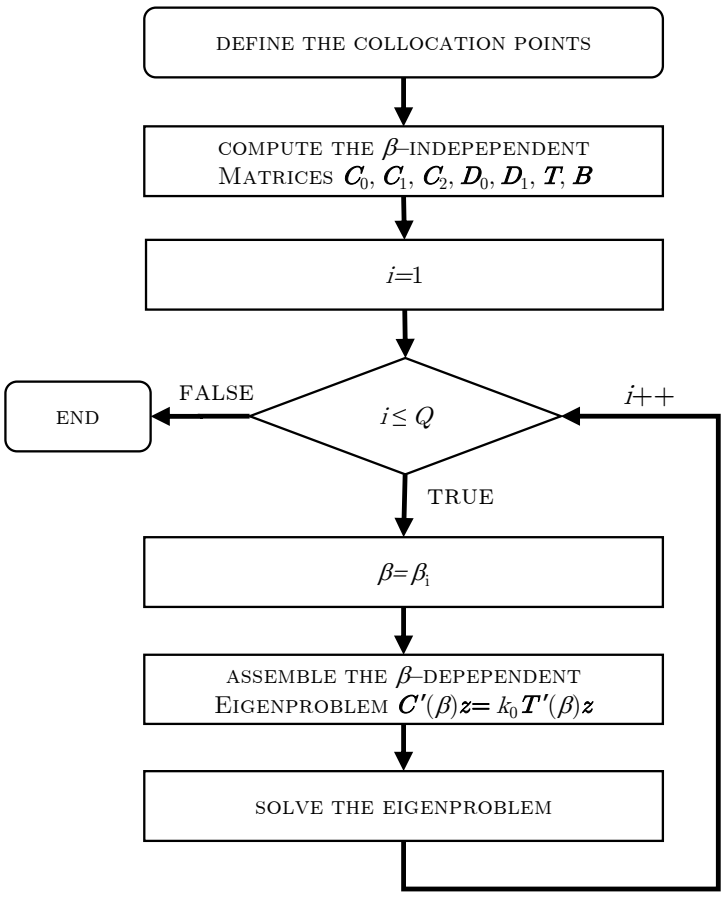

Figure 6.2: © 2019 IEEE–Flowchart of the implemented algorithm.

6.4 Numerical Results

The results shown in this section are obtained without the exploitation of any geometrical symmetry. This last aspect is analyzed in Chap 7.

All the simulations described in the following subsections have been conducted with a fixed value of $\sigma = 1$ in (6.15). This demonstrates that no preconditioning is needed, reducing the computation time.

To validate the efficiency and the accuracy of the VMM the results given by this method have been compared with the theoretical values. When no analytical solution was available, instead, the comparison has been done with the results given by ANSYS HFSS as independent validation.

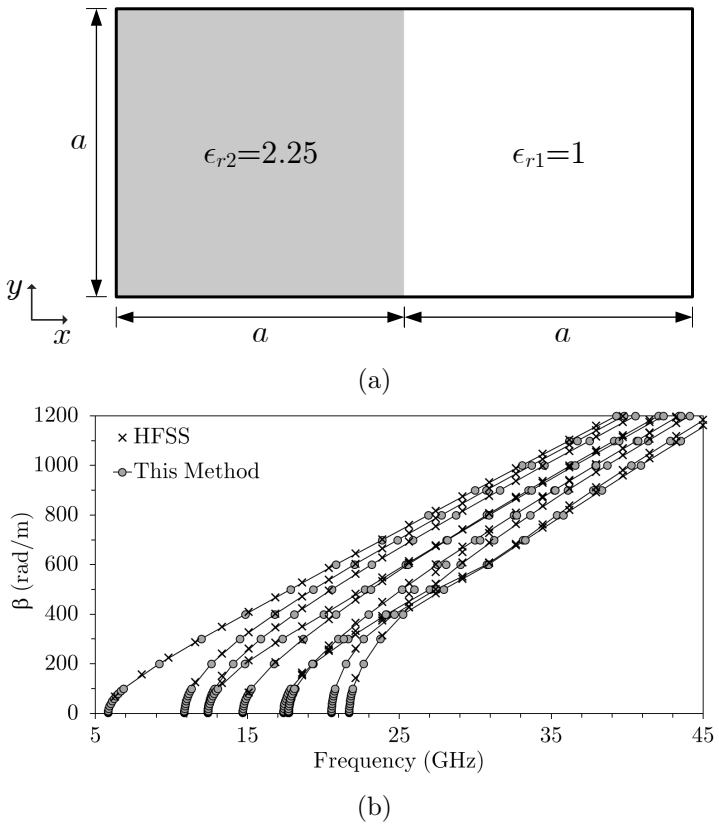

Figure 6.3: © 2019 IEEE– Dielectric Loaded Waveguide: (a) Geometry of the structure ($a = 10$ mm); (b) Dispersion diagram calculated by the variational meshless method (gray circles) compared with the HFSS simulation (black cross).

6.4.1 Dielectric Loaded Waveguide

The first example considered is the half-filled rectangular waveguide shown in Fig. 6.3(a) and analyzed in [8]. In Fig. 6.3(a) all the characteristic dimensions and the material properties are indicated. The VMM was applied to this problem by using $N = 100$ CPs to define the unknowns and, in particular, $L = 70$ ICPs and $M = 30$ BCPs. The simulation lasted 1.2 s to compute both the β-independent matrices and the 26 reported β-steps. The obtained dispersion diagram was compared with that given by ANSYS HFSS after a port-only simulation that lasted 26 s and used 284 triangles on the input port.

This comparison is shown in Fig. 6.3(b). The average discrepancy of the VMM vs HFSS results was in the order of 1%. Thanks to the enforcement

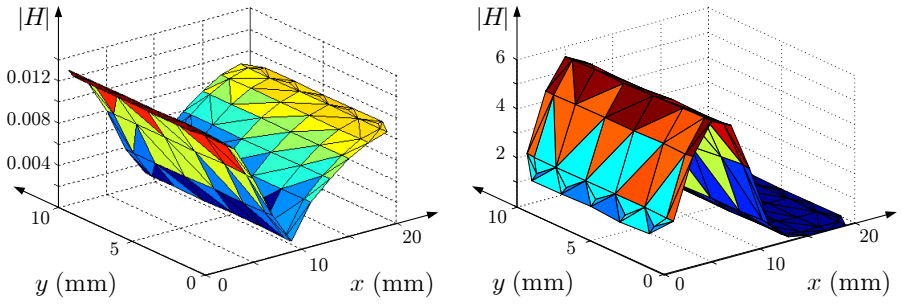

(a) (b)

Figure 6.4: © 2019 IEEE– Behavior of $|\vec{H}|$ (arbitrary units) for the first mode of the Dielectric Loaded Waveguide of Fig. 6.3: (a) $\beta = 5$ rad/m; (b) $\beta = 1200$ rad/m.

Table 6.1: © 2019 IEEE– Relative Error in the Evaluation of the Dispersion Pairs $\{\beta, f\}$ of the First Mode of the Dielectric Loaded Waveguide of Fig. 6.3. The Random Distributions of the CPs of Fig. 6.5 Were Considered.

Propagation constant β (rad/m)	Analytical frequency (GHz)	#CPs = 100 Fig. 6.5(a) $\mathcal{E}(\beta)$ (%)	#CPs = 320 Fig. 6.5(b) $\mathcal{E}(\beta)$ (%)	#CPs = 1040 Fig. 6.5(c) $\mathcal{E}(\beta)$ (%)
0	5.78212	0.4518	0.2919	0.1246
100	6.81088	0.4368	0.2811	0.1273
200	9.14706	0.3937	0.2498	0.1126
300	11.92380	0.3333	0.2072	0.0927
400	14.83090	0.2725	0.1652	0.0728
500	17.79330	0.2218	0.1308	0.0564
600	20.79280	0.1828	0.1051	0.0442
700	23.82170	0.1531	0.0856	0.0350
800	26.87440	0.1300	0.0706	0.0277
900	29.94620	0.1121	0.0592	0.0223
1000	33.03360	0.0978	0.0500	0.0179
1100	36.13360	0.0865	0.0429	0.0145
1200	39.24410	0.0770	0.0370	0.0116

of the DC and BC, no spurious solutions were obtained.

In Fig. 6.4 the graph of $|\vec{H}|$ for the first mode is shown in the case of $\beta = 5$ rad/m and $\beta = 1200$ rad/m. Note that by increasing β and, thus, the frequency, the field gets more concentrated in the region with the higher dielectric constant.

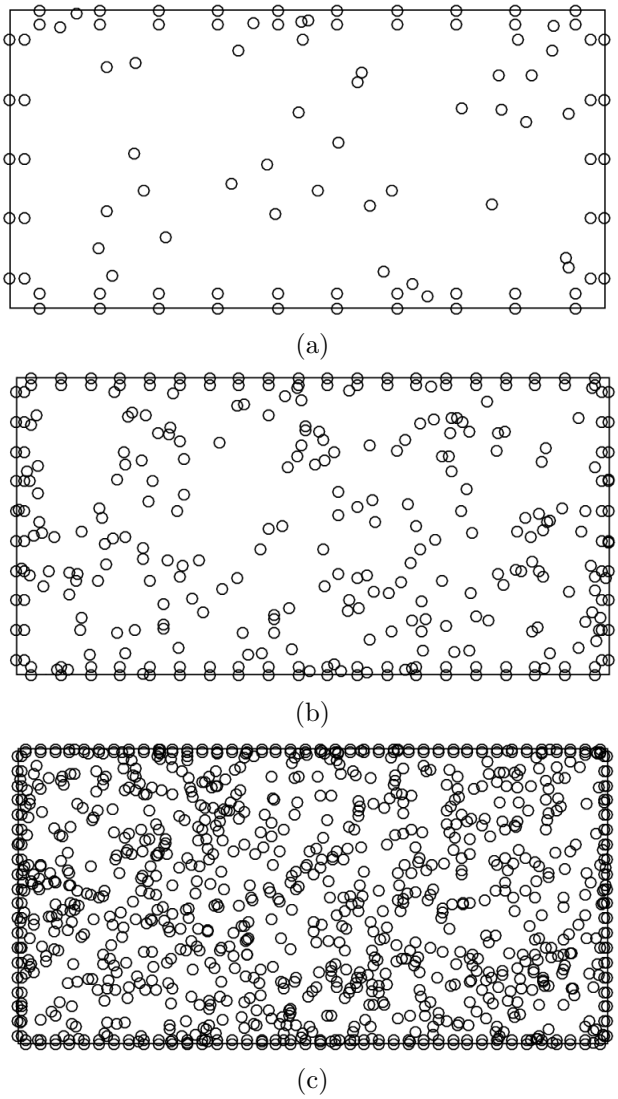

Figure 6.5: © 2019 IEEE– Random distribution of the CPs used for the convergence analysis of the Dielectric Loaded Waveguide: (a) 100 CPs; (b) 320 CPs; (c) 1040 CPs.

As the analytical solution for this structure exists [2], a convergence study was reported in [4]. In particular the frequency correspondent to various values of β (ranging from 0 to 1200 rad/m) were found with the VMM for the first mode.

The simulations were done with 3 different configurations of CPs. In particular, first was analyzed the case with 100 CPs, than with 320, and finally with 1040. In all the three cases the CPs were generated randomly

with a normal distribution inside the domain and regularly on the boundary as shown in Fig. 6.5.

Calling f_{n} the frequency found though the VMM and f_{a} the analytical solution (see [2]), the error is calculated es follows

$$\mathcal{E}(\beta) = \frac{f_{\mathrm{n}}(\beta) - f_{\mathrm{a}}(\beta)}{f_{\mathrm{a}}(\beta)} \tag{6.27}$$

and in Table 6.1 the obtained result is shown.

Note that, even if the randomly generated CPs can sometime spatially overlap, the problem keeps well-conditioned thanks to the use of ξ_i^τ in (6.7) that was proposed in [9].

6.4.2 Shielded Insulated Image Guide

The second example considered is the shielded insulated image waveguide shown in Fig. 6.6(a) and analyzed in [10]. In Fig. 6.6(a) all the characteristic dimensions and the material properties are indicated. The VMM was applied to this problem by using $N = 326$ CPs to define the unknowns and, in particular, $L = 282$ ICPs and $M = 44$ BCPs. The simulation lasted 8.7 s to compute both the β-independent matrices and the 37 reported β-steps. To obtain an independent validation, the resulting dispersion diagram was compared with that given by ANSYS HFSS after a port-only simulation that lasted 147 s and used 696 triangles on the input port.

This comparison is shown in Fig. 6.6(b). The average discrepancy of the VMM vs HFSS results was in the order of 1%. Thanks to the enforcement of the DC and BC, no spurious solutions were obtained.

In Fig. 6.7 the graph of $|\vec{H}|$ for the first mode is shown in the case of $\beta = 5$ rad/m and $\beta = 2000$ rad/m. Note that by increasing β and, thus, the frequency, the field gets more concentrated in the region with the higher dielectric constant.

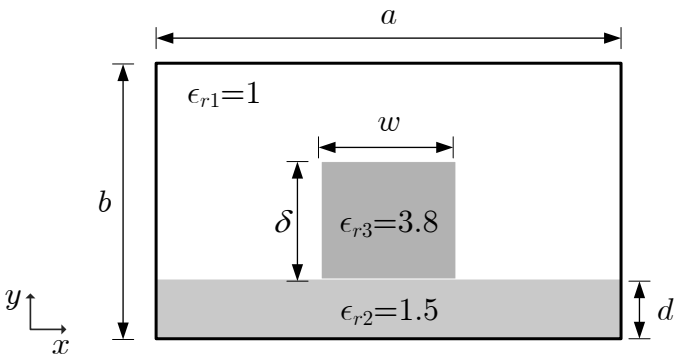

(a)

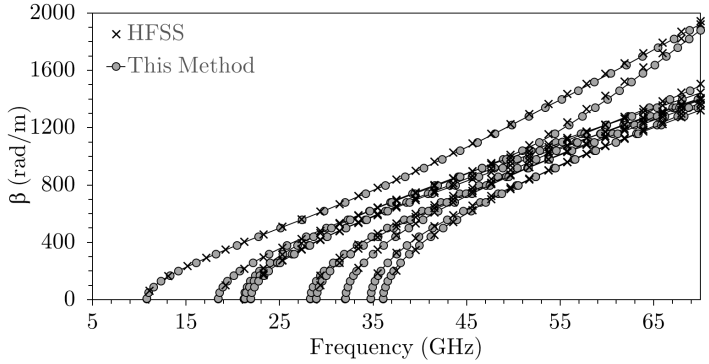

(b)

Figure 6.6: © 2019 IEEE– Shielded Insulated Image Guide: (a) Geometry of the structure ($\delta = 1$ mm, $w = 2.25$ mm, $d = 0.5$ mm, $a = 13.5$ mm, $b = 8$ mm); (b) Dispersion diagram calculated by the variational meshless method (gray circles) compared with the HFSS simulation (black cross).

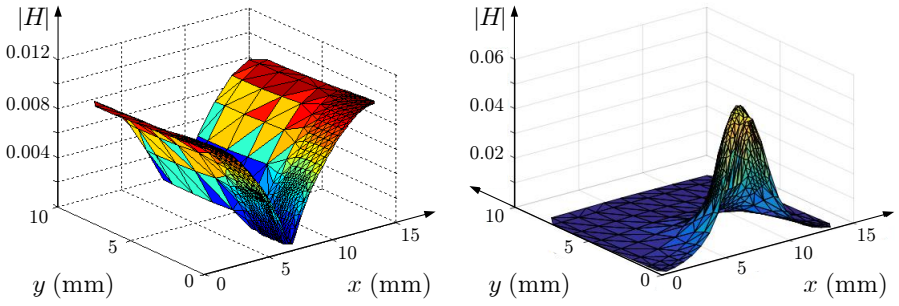

(a) (b)

Figure 6.7: © 2019 IEEE– $|\vec{H}|$ (arbitrary units) for the first mode of the Shielded Insulated Image Guide: (a) $\beta = 5$ rad/m; (b) $\beta = 1200$ rad/m.

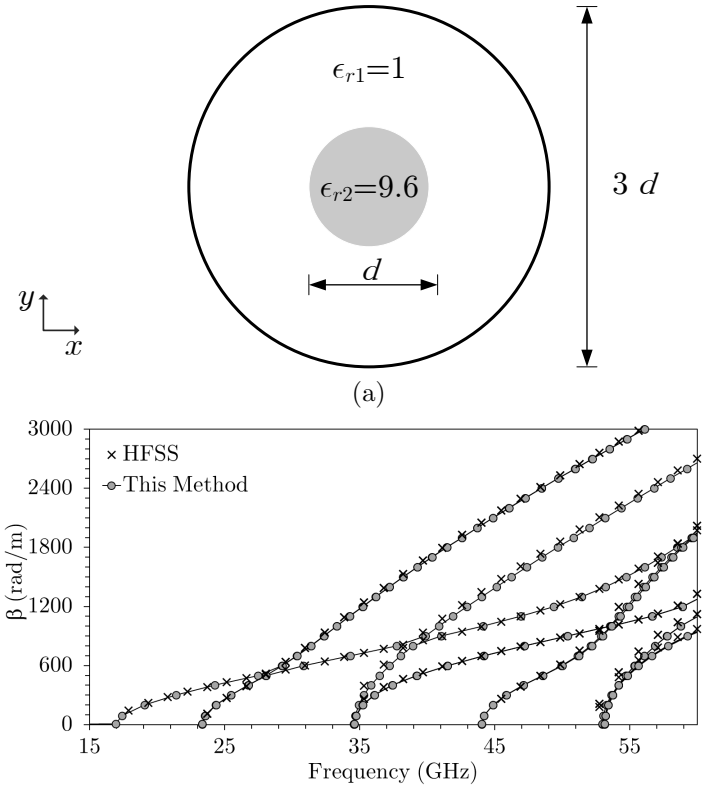

Figure 6.8: © 2019 IEEE– Round Double-Layer Shielded Waveguide: (a) Geometry of the structure (d = 6.35 mm); (b) Dispersion diagram calculated by the variational meshless method (gray circles) compared with the HFSS simulation (black cross).

6.4.3 Round Double-Layer Shielded Waveguide

The third example considered is the round double-layer shielded waveguide shown in Fig. 6.8(a) and analyzed in [11]. In Fig. 6.8(a) all the characteristic dimensions and the material properties are indicated. The VMM was applied to this problem by using $N = 685$ CPs to define the unknowns and, in particular, $L = 640$ ICPs and $M = 45$ BCPs. The simulation lasted 42.3 s to compute both the β-independent matrices and the 32 reported β-steps. The obtained dispersion diagram was compared with that given by ANSYS HFSS after a port-only simulation that lasted 690 s and used 2426 triangles on the input port.

This comparison is shown in Fig. 6.8(b). The average discrepancy of the VMM vs HFSS results was in the order of 1%. Thanks to the enforcement

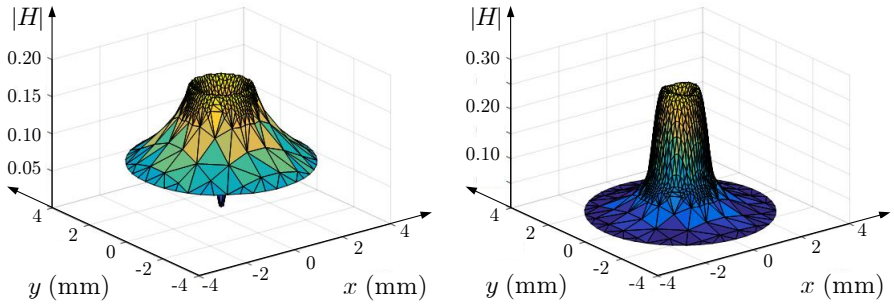

(a) (b)

Figure 6.9: © 2019 IEEE– Behavior of $|\vec{H}|$ (arbitrary units) for the first mode of the Round Double-Layer Shielded Waveguide of Fig. 6.8: (a) $\beta = 5$ rad/m; (b) $\beta = 1500$ rad/m.

Table 6.2: © 2019 IEEE– Relative Error in the Evaluation of the Dispersion Pairs $\{\beta, f\}$ of the First Mode of the Round Double-Layer Shielded Waveguide of Fig. 6.8, Considering 685 CPs.

Propagation constant β (rad/m)	Analytical frequency f (GHz)	Error $\mathcal{E}(\beta)$ (%)
0	16.80500	0.8634
5	16.80650	0.3669
90	17.26530	0.3185
200	18.96420	0.1756
300	21.34080	0.0280
400	24.24910	-0.0994
500	27.48860	-0.1995
900	41.17940	-0.2761
1400	53.09200	-0.1341
1800	58.18670	0.0393

of the DC and BC, no spurious solutions were obtained.

In Fig. 6.9 the graph of $|\vec{H}|$ for the first mode is shown in the case of $\beta = 5$ rad/m and $\beta = 1500$ rad/m. Note that by increasing β and, thus, the frequency, the field gets more concentrated in the region with the higher dielectric constant. As the analytical solution for this structure exists [2], in Table 6.2 the comparison between the VMM and the theory is provided in the evaluation of the frequency correspondent to various values of β ranging form 0 to 1800 rad/m for the first mode.

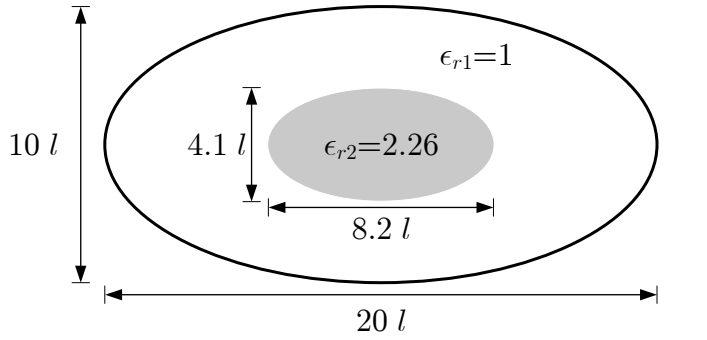

(a)

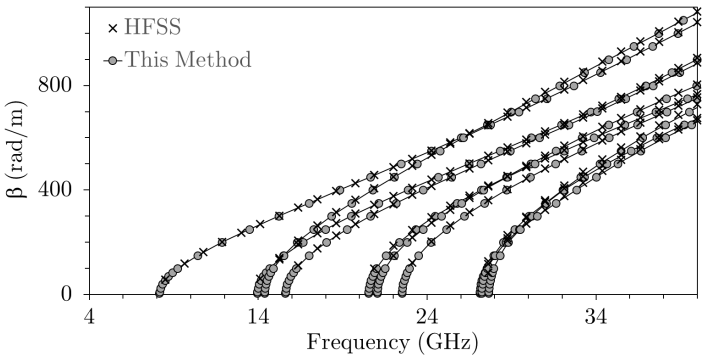

(b)

Figure 6.10: © 2019 IEEE– Elliptic Inhomogeneous Waveguide: (a) Geometry of the structure ($l = 1$ mm); (b) Dispersion diagram calculated by the variational meshless method (gray circles) compared with the HFSS simulation (black cross).

6.4.4 Elliptic Inhomogeneous Waveguide

The fourth example considered is the elliptic inhomogeneous waveguide shown in Fig. 6.10(a) and analyzed in [12]. In Fig. 6.10(a) all the characteristic dimensions and the material properties are indicated. The VMM was applied to this problem by using $N = 336$ CPs to define the unknowns and, in particular, $L = 246$ ICPs and $M = 90$ BCPs. The simulation lasted 7.44 s to compute both the β-independent matrices and the 28 reported β-steps. To obtain an independent validation the obtained dispersion diagram was compared with that given by ANSYS HFSS after a port-only simulation that lasted 112 s and used 502 triangles on the input port.

This comparison is shown in Fig. 6.10(b). The average discrepancy of the VMM vs HFSS results was in the order of 1%. Thanks to the enforcement

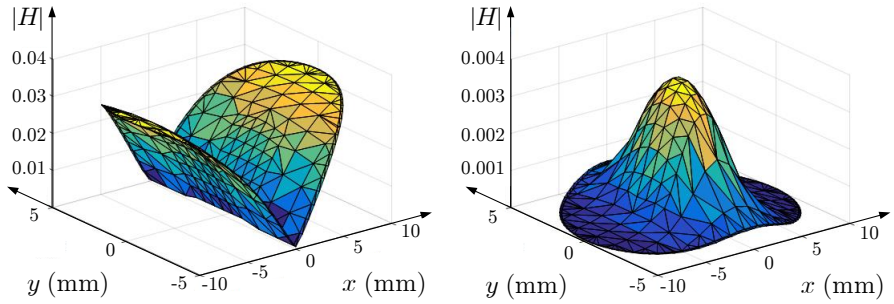

(a) (b)

Figure 6.11: © 2019 IEEE– Behavior of $|\vec{H}|$ (arbitrary units) for the first mode of the Elliptic Inhomogeneous Waveguide of Fig. 6.10: (a) $\beta = 5$ rad/m; (b) $\beta = 800$ rad/m.

of the DC and BC, no spurious solutions were obtained.

In Fig. 6.11 the graph of $|\vec{H}|$ for the first mode is shown in the case of $\beta = 5$ rad/m and $\beta = 800$ rad/m. Note that by increasing β and, thus, the frequency, the field gets more concentrated in the region with the higher dielectric constant.

6.5 Conclusion

In this chapter the VMM has been applied to the evaluation of the dispersion diagram of the modes inside a shielded waveguide filled with an inhomogeneous material. In this case the problem is no longer scalar and a vector representation of the fields is needed. The magnetic field has been used as working variable since this quantity is continuous on the interface between two dielectric materials.

The explicit enforcement of the DC and the BC permits to obtain a spurious-free set of solutions. The resulting eigenproblem is well-conditioned and the accuracy obtainable with the VMM has been investigated with various examples.

Also in this case, the VMM appears a useful technique to compute a high number of modes with a relative limited number of unknowns.

Bibliography

[1] V. Lombardi, M. Bozzi, and L. Perregrini, "A novel variational meshless method with radial basis functions for waveguide eigenvalue problems," *IEEE Trans. Microw. Theory Techn.*, Vol. 66, No. 8, pp. 3714-3723, Aug. 2018

[2] F. R. Harrington, *Time-harmonic electromagnetic fields*, Wiley-IEEE Press, 2001.

[3] J. M. Jin, *The finite element method in electromagnetics*, John Wiley & Sons, 2015.

[4] V. Lombardi, M. Bozzi, and L. Perregrini, "Evaluation of the Dispersion Diagram of Inhomogeneous Waveguides by the Variational Meshless Method," *IEEE Trans. Microw. Theory Techn.*, Vol. 67, No. 6, pp. 2105-2113, June 2019

[5] D. B. Davidson, *Computational Electromagnetics for RF and Microwave Engineering*, Cambridge University Press, 2010.

[6] J,. Demmel and W. Kahan, "Accurate singular values of bidiagonal matrices," *SIAM Journal on Scientific and Statistical Computing*, Vol. 11, No. 5, pp. 873-912, Sep. 1990

[7] J. H. Wilkinson, *The algebraic eigenvalue problem*, Vol. 87, Oxford: Clarendon Press, 1965.

[8] T. Angkaew, M. Matsuhara, and N. Kumagai, "Finite-element analysis of waveguide modes: a novel approach that eliminates spurious modes," *IEEE Trans. Microw. Theory Techn.*, Vol. 35, No. 2, pp. 117-123, Feb. 1987.

[9] V. Lombardi, M. Bozzi, and L. Perregrini, "An improved meshless method for waveguide eigenvalue problems," *IEEE Microw. Compon. Lett.*, Vol. 27, No. 12, pp. 1047–1049, Dec. 2017

[10] V. J. Brankovic, D. V. Krupezevic, and F. Arndt, "An efficient two-dimensional graded mesh finite-difference time-domain algorithm for shielded or open waveguide structures, " *IEEE Trans. Microw. Theory Techn.*, Vol. 40, No. 12, pp. 2272-2277, Mar. 1992.

[11] V. A. Malakhov, V. A. Raevskii, and S. B. Raevskii, " Added solutions of boundary value problems for double-layer guiding structures, " *International Journal of Electromagnetics and Applications*, Vol. 5, No. 2, pp. 114-119., 2012.

[12] S. R. Rengarajan and J. E. Lewis, "Dielectric loaded elliptical waveguides," *IEEE Trans. Microw. Theory Techn.*, Vol. 28, No. 10, pp. 1085-1089, Oct. 1980.

Chapter 7

Exploitation of the Symmetries

7.1 Introduction

In this chapter the theory presented in the Chap. 4 is extend to treat beside the electric wall condition also the magnetic wall condition in some portion of the boundary. This is done in order to exploit the symmetries that the cross-section of the waveguide under study could present. It is well-known, in fact, that one or two symmetries can be present in a 2D topology and that the whole spectrum of the modes inside a waveguide can be found by joining those obtained simulating respectively half or a quarter of the domain [1, 2] by imposing on every symmetry plane first the electric and then the magnetic wall condition. In particular the modes found by imposing the electric wall condition respect to a symmetry plane will be those odd respect to it, while those found by imposing the magnetic wall condition will be those even.

The theory and the results reported in in the following pages were presented in [3], therefore most of this chapter is based on that paper and will reuse extensively the material of that work.

7.2 Theory

Consider the case in which the dispersion diagram has to be evaluated for the modes existing inside the inhomogeneous shielded waveguide with the cross section presented in Fig. 7.1. In the case in which a plane of symmetry exists only half domain can be analyzed. Inside that half, N CPs are defined. among them L are the ICPs inside the domain Ω and $M = N - L$ are the BCPs that lie on $\Gamma = \Gamma_1 \cup \Gamma_2$ where Γ_1 is the portion of the external

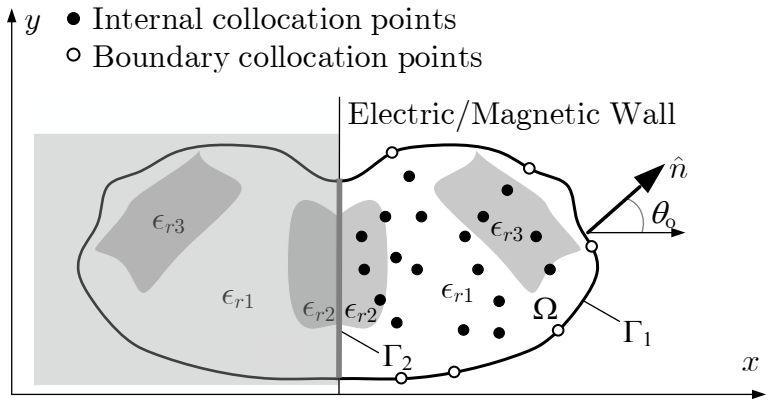

Figure 7.1: © 2019 IEEE– Cross-section of a symmetric rectangular waveguide filled with an inhomogeneous material. The circle represent the collocation points of the radial basis functions.

conductor that belongs to the half domain considered, while Γ_1 is the line of symmetry (see Fig. 7.1).

The magnetic field H inside the domain must satisfy the Helmholtz vector formula, the divergence free and a proper boundary condition. this brings to the following set of equations [2]

$$\nabla \times \left(\frac{1}{\epsilon_r} \nabla \times \vec{H}(x,y,z) \right) - k_0^2 \mu_r \vec{H}(x,y,z) = 0 \quad \text{in } \Omega \tag{7.1}$$

$$\nabla \cdot \vec{H}(x,y,z) = 0 \quad \text{in } \Omega \tag{7.2}$$

$$\hat{n} \cdot \vec{H}(x,y,z) = 0 \quad \text{on } \Gamma_1 \tag{7.3}$$

$$\hat{n} \cdot \vec{H}(x,y,z) = 0 \quad \text{or} \quad \hat{n} \times \vec{H}(x,y,z) = 0 \quad \text{on } \Gamma_2 \tag{7.4}$$

where $k_0 = \omega\sqrt{\mu_0 \epsilon_0}$ is the wavenumber in the vacuum, ω is the angular frequency, μ_0 is the vacuum permeability, ϵ_0 is the vacuum permittivity, and $\hat{n}$ is the outward normal on Γ.

The first or the second BC in (7.4) is enforced on the symmetry plane Γ_2, depending on the fact that an odd symmetry (electric wall) or a even symmetry (magnetic wall) has to be computed.

The vector Helmholtz equation (7.1) has an equivalent variational formulation [1]

$$F(\vec{H}) = \frac{1}{2} \iint_\Omega \left(\frac{1}{\epsilon_r} \nabla \times \vec{H} \cdot \nabla \times \vec{H} - k_0^2 \mu_r \vec{H} \cdot \vec{H} \right) d\Omega \tag{7.5}$$

As in [4] the magnetic field is first expanded in its vector components taking into account the propagation along the z axis. This yields to the following expression

$$\vec{H}(x,y,z) = [\hat{x}H^x(x,y) + \hat{y}H^y(x,y) + j\hat{z}H^z(x,y)]\, e^{-j\beta z} \tag{7.6}$$

Calling the general Cartesian direction τ, with $\tau = x, y, z$, it is possible to define the RBF centered in the i-th CP as $h_i^\tau(x,y)$ and write

$$H^\tau(x,y) = \sum_{i=1}^{N} a_i^\tau h_i^\tau(x,y) = \mathbf{H}^\tau(x,y)\mathbf{a}^\tau \tag{7.7}$$

where $\mathbf{H}^\tau(x,y) = [h_1^\tau(x,y), h_2^\tau(x,y), \ldots, h_N^\tau(x,y)]$ and $\mathbf{a}^\tau = [a_1^\tau, a_2^\tau, \ldots, a_N^\tau]^T$. The problem can be discretized and, after various manipulations reported in [4], this brings to the following matrix eigenproblem

$$\boldsymbol{C'}(\beta)\boldsymbol{z} = k_0^2 \boldsymbol{T'}(\beta)\boldsymbol{z} \tag{7.8}$$

where

$$\begin{aligned} \boldsymbol{C'}(\beta) &= \boldsymbol{E}_B^T \boldsymbol{E}_D^T \boldsymbol{C} \boldsymbol{E}_D \boldsymbol{E}_B \\ \boldsymbol{T'}(\beta) &= \boldsymbol{E}_B^T \boldsymbol{E}_D^T \boldsymbol{T} \boldsymbol{E}_D \boldsymbol{E}_B \end{aligned} \tag{7.9}$$

Once the eigenproblem (7.8) is solved, the original unknowns are calculated (see (7.7)) as

$$\boldsymbol{a} = (\boldsymbol{E}_D \boldsymbol{E}_B)\, \boldsymbol{z} \tag{7.10}$$

To exploit the symmetries the idea is to define the matrix $\boldsymbol{E}_B$ in a different way respect to [4] to take into account a mixed boundary condition which can be magnetic or electric wall condition in different portions of Γ. In particular by applying the MoM procedure on the boundary Γ (i.e., testing only with h_j^z centered on the BCPs) the following matrix equation is obtained

$$\boldsymbol{B}\boldsymbol{a} = \boldsymbol{0} \tag{7.11}$$

where

$$\boldsymbol{B} = \begin{bmatrix} \boldsymbol{B}_{11} & \boldsymbol{B}_{12} & \boldsymbol{0} \\ \boldsymbol{0} & \boldsymbol{0} & \boldsymbol{B}_{23} \end{bmatrix} \tag{7.12}$$

$\mathbf{0}$ is the $M \times N$ null matrix and $\boldsymbol{B}_{\alpha\beta}$ are $(2M) \times N$ matrices, and their expressions are

$$\begin{aligned}
\boldsymbol{B}_{11}(i,j) &= \int_{\Gamma} \kappa_{11}(x_o, y_o) \left[h_j^z(x_o, y_o) h_i^x(x_o, y_o) \right] dl \\
\boldsymbol{B}_{12}(i,j) &= \int_{\Gamma} \kappa_{12}(x_o, y_o) \left[h_j^z(x_o, y_o) h_i^y(x_o, y_o) \right] dl \\
\boldsymbol{B}_{23}(i,j) &= \int_{\Gamma} \kappa_{23}(x_o, y_o) \left[h_j^z(x_o, y_o) h_i^z(x_o, y_o) \right] dl
\end{aligned} \tag{7.13}$$

with $j = L+1, \ldots, N$ and where the functions $\kappa_{\alpha\beta}$ are defined as

$$\begin{aligned}
\kappa_{11}(x_o, y_o) &= \begin{cases} +cos(\theta_o) & \text{if } (x_o, y_o) \in \Gamma_1 \\ -sen(\theta_o) & \text{if } (x_o, y_o) \in \Gamma_2 \end{cases} \\
\kappa_{12}(x_o, y_o) &= \begin{cases} +sen(\theta_o) & \text{if } (x_o, y_o) \in \Gamma_1 \\ +cos(\theta_o) & \text{if } (x_o, y_o) \in \Gamma_2 \end{cases} \\
\kappa_{23}(x_o, y_o) &= \begin{cases} 0 & \text{if } (x_o, y_o) \in \Gamma_1 \\ 1 & \text{if } (x_o, y_o) \in \Gamma_2 \end{cases}
\end{aligned} \tag{7.14}$$

In (7.14) θ_o is the angle between $\hat{n}$ and $\hat{x}$ on the boundary observation point (x_o, y_o) as shown in Fig. 7.1.

Similarly to [4] the unknown vector and $\boldsymbol{E}_B$ is an orthonormal basis for the null space of $\boldsymbol{B}\boldsymbol{E}_D$, obtained from the SVD.

To make considerations about the dimension of the final problem it is possible to take the reasoning to extremes. If on all Γ only the electric wall condition is enforced, the *rank* of $\boldsymbol{B}$ is M and the dimension of $\boldsymbol{E}_B$ is $2N \times (N + L)$. If, instead, $\Gamma_1 = \emptyset$ i.e.all the points of boundary satisfy the magnetic wall condition, the *rank* of $\boldsymbol{B}$ will be $2M$ and the dimension of $\boldsymbol{E}_B$ will be $2N \times (N + L - M)$. this implies that the magnetic wall condition reduces the dimension of the final eigenproblem (7.8) more than the electric wall enforcement by a factor 2.

Finally in the case of Fig. 7.1 the problem size can be reduced by solving two separate problems with about half dimension than the whole one. This can be done by applying in both the cases the electric wall condition on Γ_1 and first the electric and then the magnetic wall condition on the symmetry plane Γ_2. The solutions will be respectively the odd and even modes respect to Γ_2.

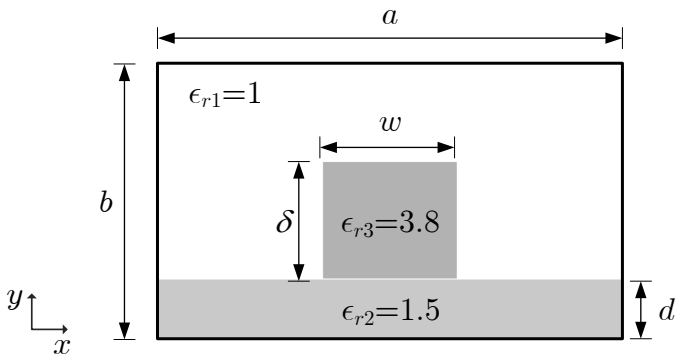

(a)

Figure 7.2: © 2019 IEEE– Geometry of the Shielded Insulated Image Guide ($a = 13.5$ mm, $\delta = 1$ mm, $w = 2.25$ mm, $d = 0.5$ mm, $b = 8$ mm)

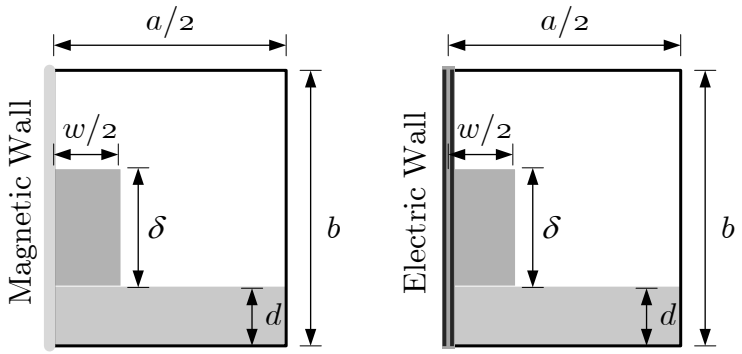

(a) (b)

Figure 7.3: © 2019 IEEE– Geometry considered to compute the modes of the Shielded Insulated Image Guide exploiting symmetries: (a) even respect to x; (b) odd respect to x.

7.3 Numerical Results

To validate the efficiency and the accuracy of the VMM the results obtained by this method have been compared with those given by ANSYS HFSS as independent validation.

7.3.1 Shielded Insulated Image Guide

The first topology analyzed is shown in Fig. 7.2 where the shielded insulated image waveguide reported in [5] is represented. In the figure all the dimensions and the properties of the material are reported.

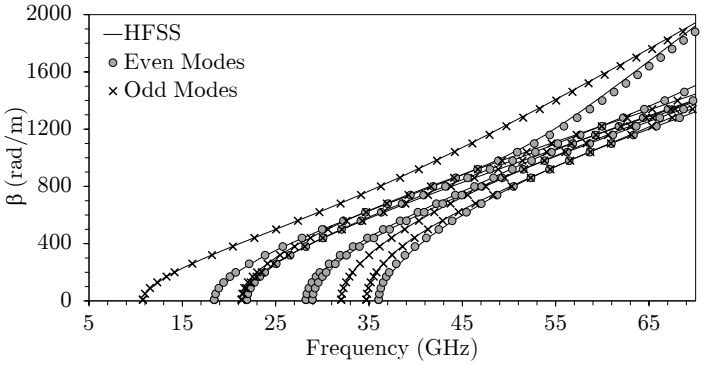

Figure 7.4: © 2019 IEEE– Dispersion diagram of the Shielded Insulated Image Guide calculated by the variational meshless method in the case of magnetic wall (gray circles), in the case of electric wall (black crosses), and by HFSS simulation (continuous line).

At the beginning the whole domain was simulated without considering any symmetry. $N = 326$ CPs were used (i.e., $L = 282$ ICPs and $M = 44$ BCPs). The simulation lasted $t_t = 10.61$ s. In particular $t_i = 2.14$ s were needed to compute the initial matrices and $t_c = 8.21$ s to run all the 37 calculations for different values of β.

The symmetry respect to the xz plane was than exploited, by simulating separately the two cases reported in Fig. 7.3. The two sets of solutions were than joined to obtain the complete spectrum required.

In Table 7.1 the running times t_i, t_c, and t_t are reported for the case of the simulation which does not exploit the symmetries, for both the partial simulations when using the symmetries, and for the total simulation when even and odd modes are evaluated separately.

Note that, the time to compute the initial matrices is not the sum of the t_i of the two partial cases, as the calculations of the initial matrices is in part identical, and can be reused.

Note that when using the symmetries the total simulation time is reduced by a factor of 43%. The obtained results are spurious-free and in agreement with those given by ANSYS HFSS with a port-only simulation with 696 triangles on the input port.

7.3.2 Circular Double-Layer Shielded Waveguide

The second topology analyzed is shown in Fig. 7.5 where the double-layer shielded waveguide, reported in [6], is represented and all the dimensions and the properties of the material are given.

Table 7.1: © 2019 IEEE– Comparison between various simulations of the Shielded Insulated Image Guide to compute 11 modes.

Method	# of unknowns	$\boldsymbol{t_i}$ (s)	$\boldsymbol{t_c}$ (s)	$\boldsymbol{t_t}$ (s)
HFSS no symmetries (Fig. 7.2)	696	—-	——	—-
VMM no symmetries (Fig. 7.2)	326	2.40	8.21	10.61
VMM even [Fig. 7.3(a)]	197	1.16	2.38	3.54
VMM odd [Fig. 7.3(b)]	197	1.17	2.15	3.32
VMM all symmetries together	197	1.49	4.53	6.02

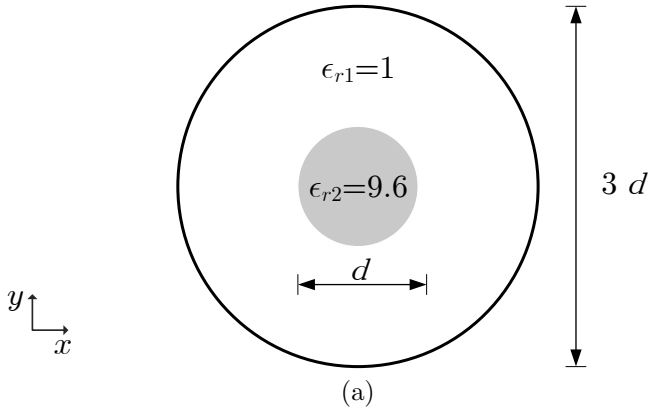

(a)

Figure 7.5: © 2019 IEEE– Geometry of the Circular Double-Layer Shielded Waveguide: ($3\ d = 6.35$ mm)

At the beginning, the whole domain was simulated without considering any symmetry. $N = 685$ CPs were used (i.e., $L = 640$ ICPs and $M = 45$ BCPs). The simulation lasted $t_t = 51.45$ s. In particular $t_i = 9.00$ s were needed to compute the initial matrices and $t_c = 42.46$ s to run all the 32 calculations for different values of β.

The symmetries respect to the xz and yz planes were than exploited, by simulating separately the four cases reported in Fig. 7.6. The four sets of solutions were than joined to obtain the complete spectrum required. In Table 7.2 the running times t_i, t_c, and t_t are reported for the case of the simulation which does not exploit the symmetries, for all the four partial simulations when using the symmetries, and for the total simulation when even and odd modes respect to each plane are evaluated separately.

Note that, the time to compute the initial matrices is not the sum of the t_i of the four partial cases, as the calculations of the initial matrices is in part identical, and can be reused.

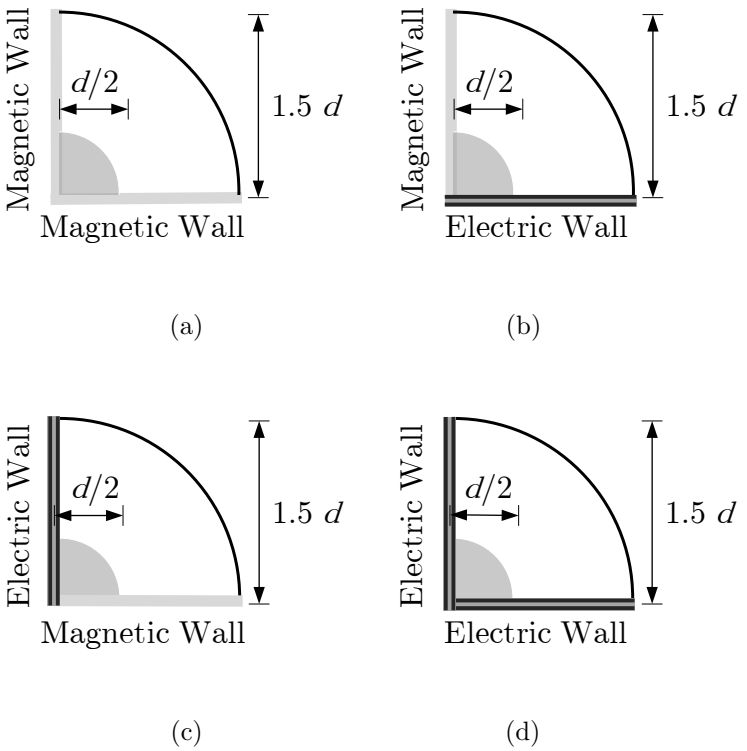

Figure 7.6: © 2019 IEEE– Geometry of the Circular Double-Layer Shielded Waveguide considered to compute the modes exploiting symmetries: (a) even respect to x and even respect to y; (b) even respect to x and odd respect to y; (c) odd respect to x and even respect to y; (d) odd respect to x and odd respect to y.

Note that when using the symmetries the total simulation time is reduced by a factor of 83%. The obtained results are spurious-free and in agreement with those given by ANSYS HFSS with a port-only simulation with 696 triangles on the input port.

7.4 Conclusion

In this chapter the theory of [4] to evaluate the dispersion diagram of an inhomogeneous filled waveguide has been extended to exploit the geometrical symmetries when available. This permits to reduce the memory and time consumption and to improve, thus, the performances of the VMM.

Two examples taken from the literature have been used to validate the

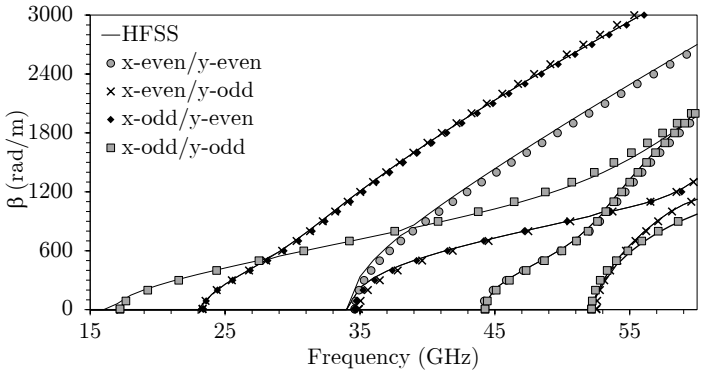

Figure 7.7: © 2019 IEEE– Dispersion diagram of the Round Double-Layer Shielded Waveguide calculated by the variational meshless method in the case of Fig. 7.6 (a) (gray circles), in the case of Fig. 7.6 (b) (black crosses), in the case of Fig. 7.6 (c) (black diamonds), in the case of Fig. 7.6 (d) (gray squares), and by HFSS simulation (continuous line).

Table 7.2: © 2019 IEEE– Comparison between various simulations of the Circular Double-Layer Shielded Waveguide to compute 11 modes.

Method	# of unknowns	$\boldsymbol{t}_i$ (s)	$\boldsymbol{t}_c$ (s)	$\boldsymbol{t}_t$ (s)
HFSS no symmetries (Fig. 7.5)	2450	—-	——	—-
VMM no symmetries (Fig. 7.5)	685	9.00	42.46	51.45
VMM even/even [Fig. 7.6(a)]	194	0.74	1.96	2.71
VMM odd/even [Fig. 7.6(b)]	194	0.81	1.84	2.65
VMM even/odd [Fig. 7.6(c)]	194	0.79	1.75	2.53
VMM odd/odd [Fig. 7.6(d)]	194	0.84	1.68	2.51
VMM all symmetries together	194	1.61	7.23	8.84

method.

Bibliography

[1] J. M. Jin, *The finite element method in electromagnetics*, John Wiley & Sons, 2015.

[2] F. R. Harrington, *Time-harmonic electromagnetic fields*, Wiley-IEEE Press, 2001.

[3] V. Lombardi, M. Bozzi, and L. Perregrini, "Exploitation of Electric/Magnetic Wall Boundary Conditions in the Variational Meshless Methods," *2019 IEEE MTT-S International Conference on Numerical Electromagnetic and Multiphysics Modeling and Optimization (NEMO)*, Boston, 29-31 May 2019

[4] V. Lombardi, M. Bozzi, and L. Perregrini, "Evaluation of the Dispersion Diagram of Inhomogeneous Waveguides by the Variational Meshless Method," *IEEE Trans. Microw. Theory Techn.*, Vol. 67, No. 6, pp. 2105-2113, June 2019

[5] V. J. Brankovic, D. V. Krupezevic, and F. Arndt, "An efficient two-dimensional graded mesh finite-difference time-domain algorithm for shielded or open waveguide structures, " *IEEE Trans. Microw. Theory Techn.*, Vol. 40, No. 12, pp. 2272-2277, Mar. 1992.

[6] V. A. Malakhov, V. A. Raevskii, and S. B. Raevskii, "Added solutions of boundary value problems for double-layer guiding structures, " *International Journal of Electromagnetics and Applications*, Vol. 5, No. 2, pp. 114-119., 2012.

Chapter 8

The Variational Meshless Method for Inhomogeneous Cavities

8.1 Introduction

In the previous chapters, the VMM [1, 2] has been presented and applied to the eigenmode analysis of a general shape shielded waveguide filled with homogeneous or inhomogeneous media.

In both the article an essentially 2D analysis has been done, as the z dependence could be separated and the equations were written on the cross-section that is a surface instead of the whole domain that is a volume.

In this chapter a different problem will be considered and its treatment will need an extension of the theory. It is the evaluation of the resonant modes inside a cavity filled with an inhomogeneous media.

As explained in [3], also in this case, this will require the solution of a vector problem and in particular the Vector Helmholtz equation with a proper BC.

When dealing with this kind of problem it is possible to use the magnetic field or the electric field as working variable. Both approaches are in principle equivalent. In this work the magnetic field is used to define the problem as this vector quantity is continuous inside the regions with inhomogeneous dielectrics.

In this chapter all the theory is presented and some implementation aspects are also discussed.

It will be possible to appreciate as, also in the case of the vector repre-

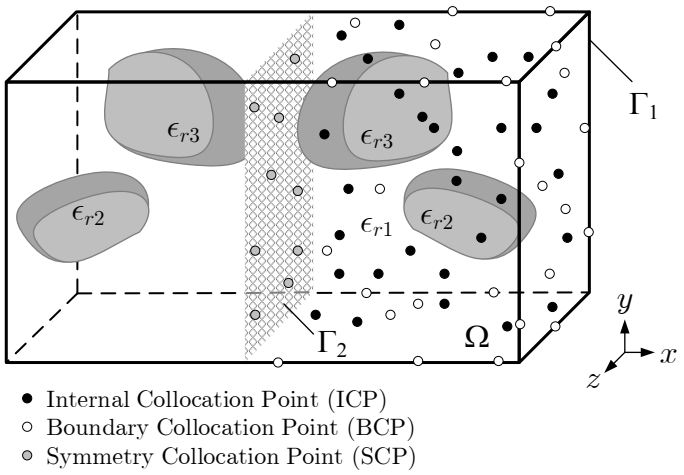

Figure 8.1: © 2019 IEEE, © 2020 IEEE– A generic 3D cavity filled with an inhomogeneous material. Ω represents the volume of the structure, Γ_1 is the external surface where the electric wall condition is enforced, and Γ_2 is a symmetry plane. The circles are the collocation points where the radial basis functions are centered.

sentation of the fields in 3D, the VMM requires a significantly lower number of unknowns than the FEM to reach the same level of accuracy.

Some numerical results will be shown to validate the method and appreciate the level of accuracy and reliability obtained when dealing with these kind of problems. The exploitation of the geometrical symmetries is explicitly presented.

The theory and the results reported in in the following pages were presented in [3, 4], therefore most of this chapter is based on these manuscripts and will reuse extensively the material of these work.

8.2 Theory

8.2.1 Starting Problem

In Fig. 8.1 a generic cavity filled with an inhomogeneous dielectric material is shown. If the electromagnetic field resonating inside this domain has to be computed, the Helmholtz equation in conjunction with the divergence-free condition, and a proper boundary condition must be enforced. This brings

to the following vector system [5]

$$\nabla \times \left(\frac{1}{\epsilon_r} \nabla \times \vec{H}(x,y,z) \right) - k_0^2 \mu_r \vec{H}(x,y,z) = 0 \quad \text{in } \Omega \tag{8.1}$$

$$\nabla \cdot \vec{H}(x,y,z) = 0 \quad \text{in } \Omega \tag{8.2}$$

$$\hat{n} \cdot \vec{H}(x,y,z) = 0 \quad \text{on } \Gamma_1 \tag{8.3}$$

where $k_0 = \omega\sqrt{\mu_0 \epsilon_0}$ is the wavenumber in the vacuum, ω is the angular frequency, μ_0 is the vacuum permeability, ϵ_0 is the vacuum permittivity, Γ_1 is the external boundary of Ω, $\hat{n}$ is the outward normal on Γ_1, and $\vec{H}$ is the magnetic field which can be approximated and, thus, discretized in a similar way than the previous chapters

$$\vec{H}(x,y,z) = \hat{x} H^x(x,y,z) + \hat{y} H^y(x,y,z) + \hat{z} H^z(x,y,z). \tag{8.4}$$

A 3D geometry can present a maximum of 3 symmetry planes. In Fig. 8.1 a case with a symmetry plane Γ_2 is shown as example. As in the case of the 2D problem (see Chap. 7), the exploitation of symmetries can improve the performances of the VMM by reducing the number f unknowns and, thus, the computation time and memory consumption or, in the other hand, increasing the accuracy and the number of modes computed with a fixed number of CPs. This is achieved by simulating one half, one quarter or one eight of the cavity for one, two or three symmetry planes, respectively. In order to do that an additional boundary condition must to be enforced on Γ_2

$$\begin{cases} \hat{n} \cdot \vec{H}(x,y,z) = 0 & \text{on } \Gamma_2^o \quad \text{(odd symmetry)} \\ \hat{n} \times \vec{H}(x,y,z) = 0 & \text{on } \Gamma_2^e \quad \text{(even symmetry)} \end{cases} \tag{8.5}$$

where Γ_2^o is the portion of Γ_2 where the odd symmetry is enforced, which corresponds to an electric wall, whereas where Γ_2^e is the portion of Γ_2 where the even symmetry is enforced, which corresponds to a magnetic wall, and $\hat{n}$ is the normal unit vector on Γ_2. Note that $\Gamma_2 = \Gamma_2^o \cup \Gamma_2^e$. Various problems must be solved to obtain the whole set of modes. In particular if the domain presents n symmetry planes ($n = 1, 2, 3$) , 2^n problems must be evaluated. This permits to consider all the even and odd symmetries that the a mode can present.

Similarly to the cases of the previous chapters, also the vector Helmholtz equation (8.1) has an equivalent variational formulation: [6]

$$F(\vec{H}) = \frac{1}{2} \iiint_\Omega \left(\frac{1}{\epsilon_r} \nabla \times \vec{H} \cdot \nabla \times \vec{H} - k_0^2 \mu_r \vec{H} \cdot \vec{H} \right) dV \tag{8.6}$$

The resonant modes and their wavenumbers can be found by extreminzing this expression. See the next sections.

8.2.2 Discretization of the Variational Problem

To discretize the problem the RBF approximation is used, as done in the previous chapters. In this case the vector magnetic field is decomposed as in (8.4). On each CP a RBF is defined. In particular, there are N CPs and, between them, there are L ICPs, M BCPs, and S symmetry collocation points (SCPs) that lie on Γ_2 ($S = S^o + S^e$, where S^o and S^e is the number of SBPs lying on Γ_2^o and Γ_2^e, respectively), as shown in Fig. 8.1. Each component of the field is discretized as follows

$$H^\tau(x,y,z) = \sum_{i=1}^{N} a_i^\tau h_i^\tau(x,y,z) \tag{8.7}$$

where h_i^τ is a RBFs and a_i^τ is the corresponding unknown coefficient.

The Gaussian RBFs are used as in the case of the 2D structures, but now also the z dependence must be included in the RBFs definition

$$h_i^\tau(x,y,z) = e^{-c_i\left[(x-x_i)^2+(y-y_i)^2+(z-z_i)^2\right]} \tag{8.8}$$

where (x_i, y_i, z_i) is the position of the i-th CP and the shape parameter c_i is defined as in [9]

$$c_i = \frac{\xi_i^\tau}{\sigma h^2} \tag{8.9}$$

where ξ_i is a scalar value generated randomly within a normal distribution in the interval $(0, 1)$ for each CP, and σ is a parameter typically selected by using preconditioning algorithms like the leave-one-out cross validation (LOOCV) [8]. As will be shown in Sec. 8.3, this step can be avoided by setting $\sigma = 1$. In (8.9), h is the average distance which can be computed in a similar way than in the 2D case [7] but, this time, on the volume of Ω:

$$h = \frac{V_\Omega^{1/3}}{N^{1/3} - 1} \tag{8.10}$$

V_Ω is the volume of Ω. By substituting (8.4), (8.7), and (8.8) in (8.6), the following matrix equation is obtained

$$F(\boldsymbol{a}) = \frac{1}{2}\left[\boldsymbol{a}^T\boldsymbol{C}\boldsymbol{a} - k^2\boldsymbol{a}^T\boldsymbol{T}\boldsymbol{a}\right] \tag{8.11}$$

where the unknown vector $\boldsymbol{a}$ is defined as

$$\boldsymbol{a} = [a_1^x, a_2^x, \ldots, a_N^x, a_1^y, a_2^y, \ldots, a_N^y, a_1^z, a_2^z, \ldots, a_N^z]^T \tag{8.12}$$

and the following matrices have been introduced

$$\boldsymbol{C} = \begin{bmatrix} \boldsymbol{C}_{11} & \boldsymbol{C}_{12} & \boldsymbol{C}_{13} \\ \boldsymbol{C}_{12}^T & \boldsymbol{C}_{22} & \boldsymbol{C}_{23} \\ \boldsymbol{C}_{13}^T & \boldsymbol{C}_{23}^T & \boldsymbol{C}_{33} \end{bmatrix} \quad \boldsymbol{T} = \begin{bmatrix} \boldsymbol{T}_{11} & \boldsymbol{0} & \boldsymbol{0} \\ \boldsymbol{0} & \boldsymbol{T}_{22} & \boldsymbol{0} \\ \boldsymbol{0} & \boldsymbol{0} & \boldsymbol{T}_{33} \end{bmatrix} \tag{8.13}$$

The sub-matrices $\boldsymbol{C}_{\alpha\beta}$ and $\boldsymbol{T}_{\alpha\beta}$ are $N \times N$ and their entries are

$$\boldsymbol{C}_{11}(j,i) = +\iiint_\Omega \frac{1}{\epsilon_r} \left(\frac{\partial h_j^x}{\partial z} \frac{\partial h_i^x}{\partial z} + \frac{\partial h_j^x}{\partial y} \frac{\partial h_i^x}{\partial y} \right) dV \tag{8.14}$$

$$\boldsymbol{C}_{22}(j,i) = +\iiint_\Omega \frac{1}{\epsilon_r} \left(\frac{\partial h_j^y}{\partial x} \frac{\partial h_i^y}{\partial x} + \frac{\partial h_j^y}{\partial z} \frac{\partial h_i^y}{\partial z} \right) dV \tag{8.15}$$

$$\boldsymbol{C}_{33}(j,i) = +\iiint_\Omega \frac{1}{\epsilon_r} \left(\frac{\partial h_j^z}{\partial x} \frac{\partial h_i^z}{\partial x} + \frac{\partial h_j^z}{\partial y} \frac{\partial h_i^z}{\partial y} \right) dV \tag{8.16}$$

$$\boldsymbol{C}_{12}(j,i) = -\iiint_\Omega \frac{1}{\epsilon_r} \frac{\partial h_j^x}{\partial y} \frac{\partial h_i^y}{\partial x} \, dV \tag{8.17}$$

$$\boldsymbol{C}_{13}(j,i) = -\iiint_\Omega \frac{1}{\epsilon_r} \frac{\partial h_j^x}{\partial z} \frac{\partial h_i^z}{\partial x} \, dV \tag{8.18}$$

$$\boldsymbol{C}_{23}(j,i) = -\iiint_\Omega \frac{1}{\epsilon_r} \frac{\partial h_j^z}{\partial y} \frac{\partial h_i^y}{\partial z} \, dV \tag{8.19}$$

$$\boldsymbol{T}_{11}(j,i) = +\iiint_\Omega \mu_r h_j^x \, h_i^x \, dV \tag{8.20}$$

$$\boldsymbol{T}_{22}(j,i) = +\iiint_\Omega \mu_r h_j^y \, h_i^y \, dV \tag{8.21}$$

$$\boldsymbol{T}_{33}(j,i) = +\iiint_\Omega \mu_r h_j^z \, h_i^z \, dV \tag{8.22}$$

The Gaussian RBFs (8.8) are C^∞ and their derivatives can be analytically derived as follows

$$\frac{\partial h_i^\tau(x,y,z)}{\partial x} = -2c_i(x - x_i) \, h_i^\tau(x,y,z) \tag{8.23}$$

$$\frac{\partial h_i^\tau(x,y,z)}{\partial y} = -2c_i(y - y_i) \, h_i^\tau(x,y,z) \tag{8.24}$$

$$\frac{\partial h_i^\tau(x,y,z)}{\partial z} = -2c_i(z - z_i) \, h_i^\tau(x,y,z) \tag{8.25}$$

8.2.3 Discretization of the Divergence Condition

Substituting (8.4), (8.7), and (8.8) into 8.2) the following matrix expression is obtained

$$\nabla \cdot \vec{H} = \sum_{i=1}^{N} a_i^x \frac{\partial h_i^x}{\partial x} + \sum_{i=1}^{N} a_i^y \frac{\partial h_i^y}{\partial x} + \sum_{i=1}^{N} a_i^z \frac{\partial h_i^z}{\partial z} = 0 \tag{8.26}$$

By applying the Method of Moments (MoM) and by using N RBFs h_j as test functions, the following matrix expression is obtained

$$\boldsymbol{Da} = \boldsymbol{0} \tag{8.27}$$

which can be partitioned as

$$\boldsymbol{D} = \begin{bmatrix} \boldsymbol{D}_{11} & \boldsymbol{D}_{12} & \boldsymbol{D}_{13} \end{bmatrix} \tag{8.28}$$

and the $\boldsymbol{D}_{\alpha\beta}$ are all $N \times N$ matrices with the following entries

$$\boldsymbol{D}_{11}(j,i) = \iiint_{\Omega} h_j \, \frac{\partial h_i^x}{\partial x} \, dV \tag{8.29}$$

$$\boldsymbol{D}_{12}(j,i) = \iiint_{\Omega} h_j \, \frac{\partial h_i^y}{\partial y} \, dV \tag{8.30}$$

$$\boldsymbol{D}_{13}(j,i) = \iiint_{\Omega} h_j \, \frac{\partial h_i^z}{\partial z} \, dV \tag{8.31}$$

Note that matrix $\boldsymbol{D}$ has dimension $N \times 3N$ and, thus, has a *nullity* of $2N$. In (8.29)-(8.31) the derivative are computed using (8.23)-(8.25).

8.2.4 Discretization of the Boundary and the Symmetry Conditions

The considered problem requires the enforcement of the electric wall condition (8.3) on the boundary Γ_1 (see Fig. 8.1). The performances of the presented algorithm can, anyway, take advantage on the exploitation of symmetries in the case these are present in the domain under evaluation. In particular, a 3D geometry can present n orthogonal planes of symmetry ($n = 1, 2, 3$). The problem can, thus, be analyzed by computing the solutions of all the 2^n eigenvalue problems arising from all the combinations of even and odd symmetries. These 2^n problems are, in any case, more simple to evaluate as their size will be approximately $1/2^n$. Recalling that the the solution of the eigenvalue problem is proportional to the cube of the dimension

of the matrices, it is possible appreciate the benefits in various situations. During the design of microwave components this subdivision of the whole problem (with various ones smaller in size) can be really useful also in the case in which only some classes of modes are needed.

When only odd symmetries are considered, the BCs on Γ_1 and Γ_2 are all of the same type (electric wall condition). In the other cases the magnetic wall condition must be imposed on the portions of Γ_2 where the even symmetry is considered. In these cases a mixed BC must be enforced on the subdomain under study (electric wall on $\Gamma_1 \cup \Gamma_2^o$ and magnetic wall on Γ_2^e). By applying the Method of Moments (MoM) and by using, as test functions, a set of $(M + S)$ RBFs h_j centered on the BCPs and SCPs, the following matrix expression is obtained

$$\boldsymbol{B}\boldsymbol{a} = \boldsymbol{0} \tag{8.32}$$

where $\boldsymbol{B}$ can be partitioned as

$$\boldsymbol{B} = \begin{bmatrix} \boldsymbol{B}_{1x} & \boldsymbol{B}_{1y} & \boldsymbol{B}_{1z} \\ \boldsymbol{B}_{2x} & \boldsymbol{B}_{2y} & \boldsymbol{B}_{2z} \end{bmatrix} \tag{8.33}$$

$\boldsymbol{0}$ is the null matrix of dimension $2(M+S) \times 1$, while the $\boldsymbol{B}_{\alpha\tau}$ matrices have dimension $(M + S) \times N$ and are defined as follows

$$\boldsymbol{B}_{1\tau}(j,i) = \iint_{\Gamma_1 \cup \Gamma_2^o} \hat{n} \cdot \hat{\tau}\ h_i^\tau h_j\, dS + \iint_{\Gamma_2^e} \hat{t} \cdot \hat{\tau}\ h_i^\tau h_j\, dS \tag{8.34}$$

$$\boldsymbol{B}_{2\tau}(j,i) = \iint_{\Gamma_2^e} (\hat{t} \times \hat{n}) \cdot \hat{\tau}\ h_i^\tau h_j\, dS \tag{8.35}$$

where $\hat{n}$ is the normal unit vector, $\hat{t}$ is an arbitrary unit vector orthogonal to $\hat{n}$ (i.e., $\hat{t} \times \hat{n} = 0$), while the symbol $\hat{\tau}$ stands for the unit vector along x, y, or z (i.e., $\hat{\tau} = \hat{x}, \hat{y}, \hat{z}$).

8.2.5 Final Problem

Beside the equation (8.11), the DC and BC must be imposed. This reduces the degrees of freedom associated to the vector $\boldsymbol{a}$.

Equation (8.27) states that the vector $\boldsymbol{a}$ can be written as

$$\boldsymbol{a} = \boldsymbol{E}_D \boldsymbol{x} \tag{8.36}$$

where $\boldsymbol{x}$ is a $2N \times 1$ vector and $\boldsymbol{E}_D$ is an orthonormal basis for the null space of $\boldsymbol{D}$ and is obtained from the SVD. Its dimension is $3N \times 2N$.

Introducing (8.36) into (8.32) the the following relation is obtained

$$\boldsymbol{B}\boldsymbol{E}_D\boldsymbol{x} = \boldsymbol{0} \tag{8.37}$$

and thus

$$\boldsymbol{x} = \boldsymbol{E}_B\boldsymbol{z} \tag{8.38}$$

where $\boldsymbol{z}$ is an unknown vector and $\boldsymbol{E}_B$ is an orthonormal basis for the null space of $\boldsymbol{B}\boldsymbol{E}_D$, obtained similarly to the previous step.

Substituting (8.38) and (8.36) into (8.11) and extremizing the resulting expression (by deriving respect to $\boldsymbol{z}$), the following eigensystem is obtained

$$\boldsymbol{C'}\boldsymbol{z} = k_0^2\boldsymbol{T'}\boldsymbol{z} \tag{8.39}$$

in which the mass and stiffness matrices are

$$\begin{aligned} \boldsymbol{C'} &= \boldsymbol{E}_B^T\boldsymbol{E}_D^T\boldsymbol{C}\boldsymbol{E}_D\boldsymbol{E}_B \\ \boldsymbol{T'} &= \boldsymbol{E}_B^T\boldsymbol{E}_D^T\boldsymbol{T}\boldsymbol{E}_D\boldsymbol{E}_B \end{aligned} \tag{8.40}$$

The solution of (8.39) permits to find the vector $\boldsymbol{z}$ and, thus, the starting unknown through the following change of base

$$\boldsymbol{a} = (\boldsymbol{E}_D\boldsymbol{E}_B)\,\boldsymbol{z} \tag{8.41}$$

Note that the matrices $\boldsymbol{C'}$ and $\boldsymbol{T'}$ are both real and symmetric.

8.3 Numerical Results

All the simulations described in the following subsections have been conducted with a fixed value of $\sigma = 1$ in (8.9). This demonstrates that no preconditioning is needed, reducing the computation time.

To validate the efficiency and the accuracy of the VMM the results given by this method have been compared with the theoretical values. When no analytical solution was available, instead, the comparison has been done with the results given by ANSYS HFSS as independent validation. All the solutions reported were spurious free thanks to (8.27) and (8.32).

8.3.1 Empty Rectangular Cavity

The first example considered is the rectangular hollow cavity of Fig. 8.2. This is a useful test bench for the VMM since its analytical solution is well-known in the literature [9]. Various cases have been simulated to test the exploitation of the symmetries. In the following the results achieved are listed.

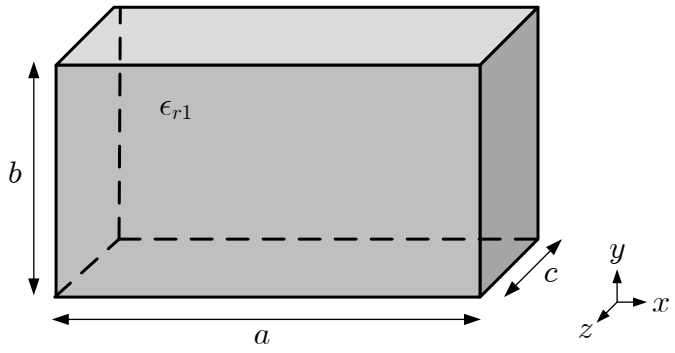

Figure 8.2: © 2019 IEEE, © 2020 IEEE– Geometry of the empty rectangular cavity ($a = 10$ mm, $b = 7.5$ mm, and $c = 5$ mm, $\epsilon_{r1} = 1$).

- First of all, the whole domain has been considered with 932 CPs. The simulation lasted 47.3 s to evaluate 500 modes. Those obtained with an accuracy better than 0.5% were 289, while those calculated with a precision better than 1% were 370. Fig. 8.3(a) shows the results achieved.
- Than the symmetry respect to the $x-$axis has been taken into account. This reduced the size of the problem to one half by computing two cases. 492 CPs were considered. The simulation lasted 10.32 s to evaluate 500 modes. Those obtained with an accuracy better than 0.5% were 286, while those calculated with a precision better than 1% were 347. Fig. 8.3(b) shows the results achieved.
- Afterward the symmetries respect to the $x-$ and $z-$ axis have been taken into account. This reduced the size of the problem to one quarter by computing four cases. 322 CPs were considered. The simulation lasted 3.62 s to evaluate 500 modes. Those obtained with an accuracy better than 0.5% were 259, while those calculated with a precision better than 1% were 329. Fig. 8.3(c) shows the results achieved.
- Than the symmetries respect to the $x-$, $y-$, and $z-$axis have been taken into account. This reduced the size of the problem to one eighth by computing eight cases. 260 CPs were considered. The simulation lasted 3.34 s to evaluate 500 modes. Those obtained with an accuracy better than 0.5% were 302, while those calculated with a precision better than 1% were 393. Fig. 8.3(d) shows the results achieved.
- The last case considered is the exploitation of the symmetries respect to the $x-$, $y-$, and $z-$axis but with 764 CPs. The simulation lasted 52.6

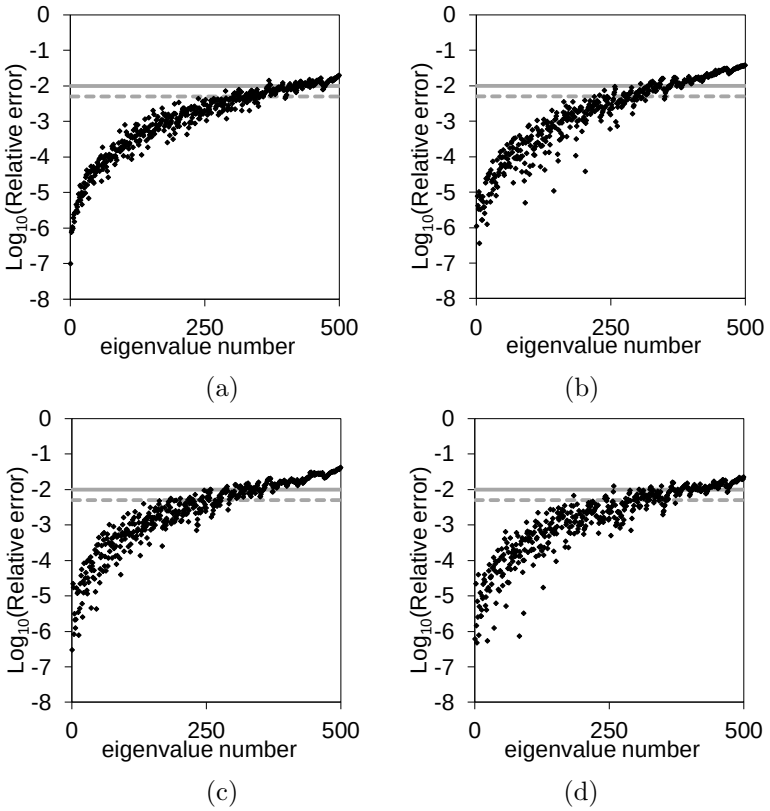

Figure 8.3: © 2019 IEEE, © 2020 IEEE– Error in the calculation of resonance frequencies of the empty rectangular cavity (dashed and solid gray line corresponds to 0.5% and 1%, respectively). (a) Without exploiting symmetries, 289 CPs; (b) Exploiting the $x-$axis symmetry, 184 CPs; (c) Exploiting the $x-$ and $z-$axis symmetries, 308 CPs; (d) Exploiting the $x-$, $y-$, and $z-$axis symmetries, 260 CPs.

s. 1440 modes were computed with a precision better than 0.5%, while 1924 were obtained with a precision better than 1%. Fig. 8.4 shows the results achieved. As can be seen there is, respect to the first case, a significant improvement on the number of the calculated modes with a similar computation time.

All these results are summarized in Table 8.1 where it can be appreciated the two possible applications of the exploitation of the symmetries. Comparing the first with the fourth line, it can be seen that it is possible to obtain the same level of accuracy by reducing the calculation time by 93%. Dually, comparing the first and the fifth line, it can be noted that the number of modes calculated increases by a factor of 500%.

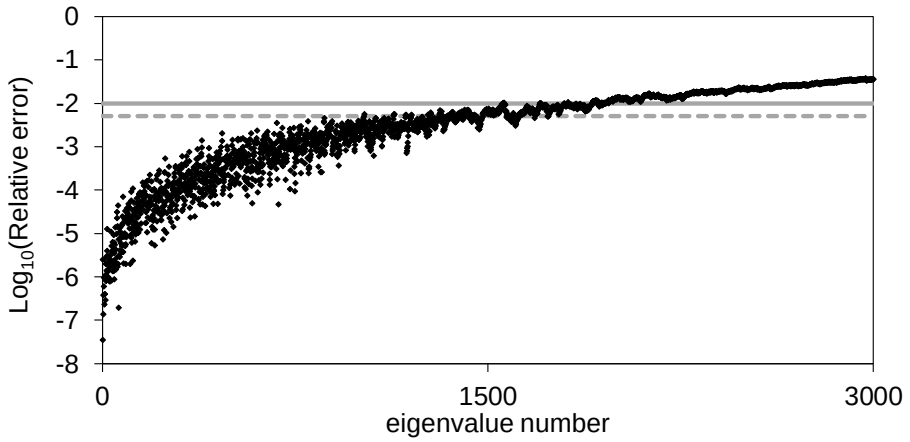

Figure 8.4: © 2019 IEEE, © 2020 IEEE– Simulation of a eight of the domain in Fig. 8.2, taking into account the symmetry respect to $x-$, $y-$, and $z-$axis and using 764 CPs (dashed and solid gray line corresponds to 0.5% and 1%, respectively).

Table 8.1: Summary of the Simulations of the Empty Rectangular Cavity.

Symmetries	#CPs	CPU time	#modes error<0.5%	#modes error<1%	Figure
none	932	47.30 s	289	370	Fig. 8.3(a)
x-axis	492	10.32 s	286	347	Fig. 8.3(b)
x-,z-axis	322	3.62 s	259	329	Fig. 8.3(c)
x-,y-,z-axis	260	3.34 s	302	393	Fig. 8.3(d)
x-,y-,z-axis	764	52.60 s	1440	1924	Fig. 8.4

8.3.2 Air-filled circular cylindrical cavity

The second example considered is the cylindrical hollow cavity of Fig. 8.5. This is another useful test bench for the VMM as, also in this case, the analytical solution is available [9]. Two cases have been simulated to test the exploitation of the symmetries. In the following the results achieved are listed.

- First of all, the whole domain has been considered with 585 CPs. The simulation lasted 17.1 s to evaluate 500 modes. Those obtained with an accuracy better than 0.5% were 199, while those calculated with a precision better than 1% were 239. Fig. 8.6 shows the results achieved.
- The second case considered is the exploitation of the symmetries respect to the $x-$, $y-$, and $z-$axis by using 680 CPs. The simulation lasted

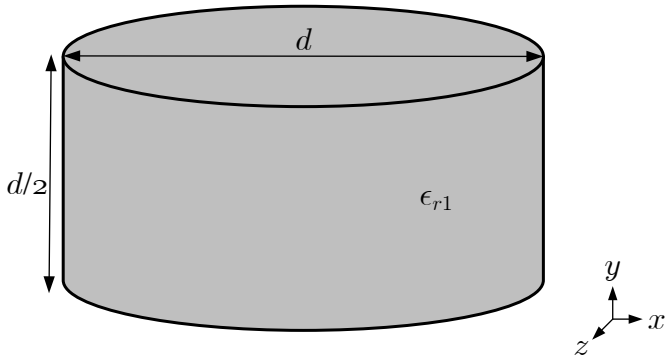

Figure 8.5: Geometry of the Air-filled circular cylindrical cavity ($d = 10$ mm, $\epsilon_{r1} = 1$).

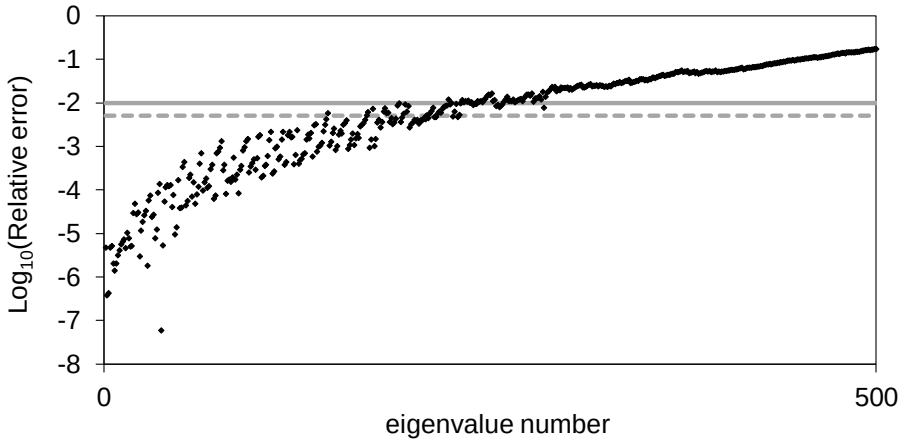

Figure 8.6: © 2019 IEEE, © 2020 IEEE– Simulation of the case in Fig. 8.5, using 585 CPs (dashed and solid gray line corresponds to 0.5% and 1%, respectively).

45.0 s. 995 modes were computed with a precision better than 0.5%, while 1342 were obtained with a precision better than 1%. 8.7 shows the results achieved. As can be seen there is, respect to the first case, a significant improvement on the number of the calculated modes.

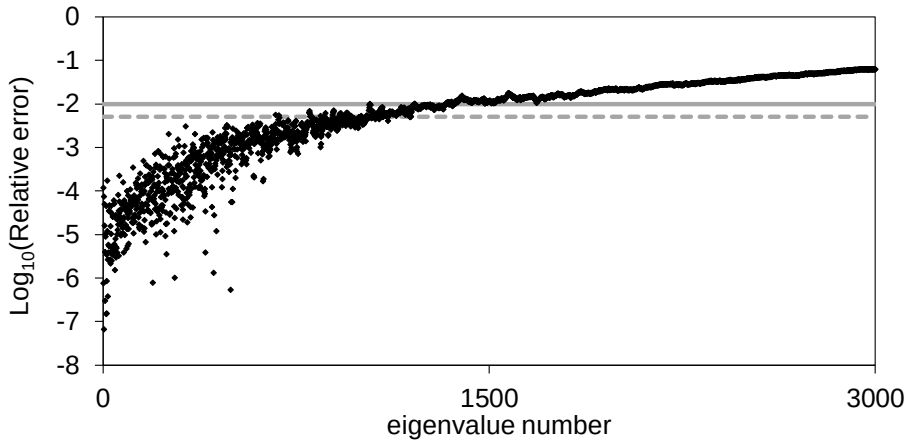

Figure 8.7: © 2019 IEEE, © 2020 IEEE– Simulation of the case in Fig. 8.5, exploiting the symmetry respect to $x-$, $y-$, and $z-$axis and using 585 CPs (dashed and solid gray line corresponds to 0.5% and 1%, respectively).

8.3.3 Half-Filled Rectangular Cavity

The third examples taken into account is the half filled rectangular cavity shown in Fig. 8.8(a). This structure is analyzed in [6].

The simulation has first been run without exploiting the symmetries and required 33.48 s to compute 200 modes. The number of CPs used was 812.

The comparison between the obtained result and that given by ANSYS HFSS is shown in Fig. 8.8(b) for the first 20 modes with the black line. The HFSS simulation was an eigenmode analysis with 15311 tetrahedra.

Afterward the symmetries respect to the $y-$ and $z-$axis have been exploited and the number of CPs considered was 332. The simulation lasted, in this way, approximately 4 s to obtain about the same accuracy than the previous case. This can be appreciated in Fig. 8.8(b) (gray line).

Also in this case there is the analytical solution. In Table 8.2 the comparison between the analytical formula, the VMM, and HFSS is given.

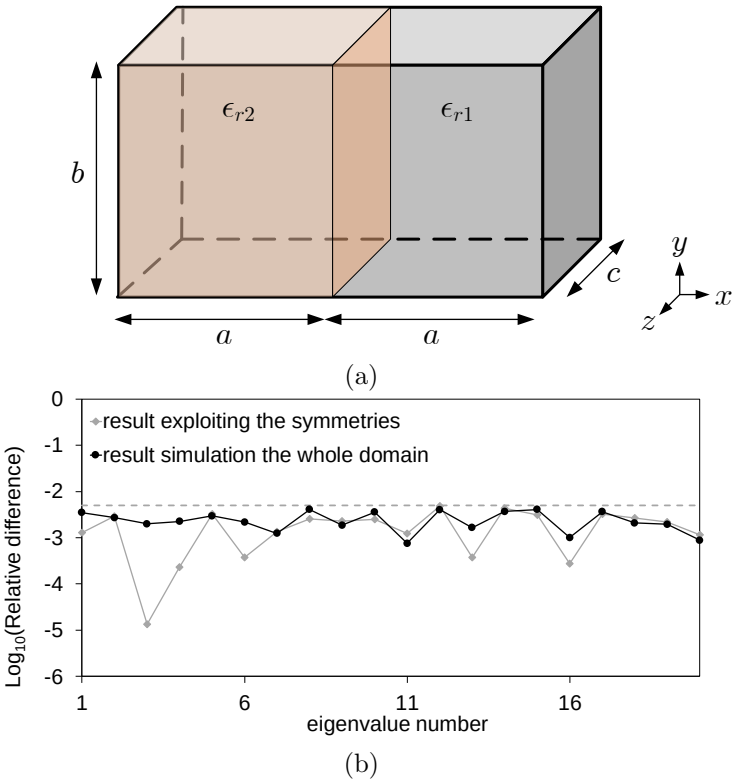

Figure 8.8: © 2019 IEEE, © 2020 IEEE– Half-filled rectangular cavity: (a) Geometry of the domain ($a = 5$ mm, $b = 1$ mm, $c = 10$ mm, $\epsilon_{r1} = 1$, $\epsilon_{r2} = 2$); (b) Relative difference between the VMM and the results given by ANSYS HFSS on the first 20 modes (black line: VMM analysis without symmetries; gray line VMM analysis exploiting symmetries).

Table 8.2: © 2019 IEEE, © 2020 IEEE– Error in the calculation of the first six modes of the half-filled rectangular cavity.

Mode	Analytical	Meshless Method		HFSS	
	k_0 (cm^{-1})	k_0 (cm^{-1})	error %	k_0 (cm^{-1})	error %
TE^z_{101}	3.538	3.5399	0.05	3.5354	0.07
TE^z_{201}	5.445	5.4572	0.22	5.4413	0.07
TE^z_{102}	5.935	5.9939	0.99	5.9938	0.99
TE^z_{301}	7.503	7.4997	0.04	7.498	0.07
TE^z_{202}	7.633	7.6526	0.26	7.6279	0.07
TE^z_{103}	8.096	8.0932	0.03	8.0902	0.07

8.4 Conclusion

In this chapter the VMM has been extended to deal with the 3D problem of finding the resonance modes inside a cavity filled with inhomogeneous material. In this case the theory has been presented in conjunction with the exploitation of symmetries to improve the performances of the method reducing the computation time and the memory consumption to obtain a certain level of accuracy or, similarly, to improve the accuracy keeping the computational cost constant.

The theory has been validated through the comparison with analytical formulas when possible or HFSS as independent validation.

Also in the case of finding the 3D resonant modes the VMM permits to evaluate an high number of modes with a relative low number of unknowns.

Bibliography

[1] V. Lombardi, M. Bozzi, and L. Perregrini, "A novel variational meshless method with radial basis functions for waveguide eigenvalue problems," *IEEE Trans. Microw. Theory Techn.*, Vol. 66, No. 8, pp. 3714-3723, Aug. 2018

[2] V. Lombardi, M. Bozzi, and L. Perregrini, "Evaluation of the Dispersion Diagram of Inhomogeneous Waveguides by the Variational Meshless Method," *IEEE Trans. Microw. Theory Techn.*, Vol. 67, No. 6, pp. 2105-2113, June 2019

[3] V. Lombardi, M. Bozzi, and L. Perregrini, "Analysis of Inhomogeneous Rectangular Cavities Using the Variational Meshless Method," *8th European Microwave Conference (EuMC2019)*, 4, Paris, France, 1-3 Oct. 2019.

[4] V. Lombardi, M. Bozzi, and L. Perregrini, "Exploiting Symmetries in the Variational Meshless Method for 3D Inhomogeneous Cavities," *IEEE Trans. Microw. Theory Techn.*, (ACCEPTED)

[5] F. R. Harrington, *Time-harmonic electromagnetic fields*, Wiley-IEEE Press, 2001.

[6] J. M. Jin, *The finite element method in electromagnetics*, John Wiley & Sons, 2015.

[7] T. Kaufmann, C. Engström, C. Fumeaux, and R. Vahldieck, "Eigenvalue analysis and longtime stability of resonant structures for the meshless radial point interpolation method in time domain," *IEEE Trans. Microw. Theory Techn.*, Vol. 58, No. 12, pp. 3399–3408, Dec. 2010.

[8] M. Mongillo, "Choosing basis functions and shape parameters for radial basis function methods," *SIAM Undergraduate Research Online*, Vol. 4, pp. 190–209, 2011.

[9] F. R. Harrington, *Time-harmonic electromagnetic fields*, Wiley-IEEE Press, 2001.

Chapter 9

Conclusion

In this manuscript, the Variational Meshless Method (VMM) has been presented. It consists in the employment of the meshless method based on the RBF in conjunction with the variational technique.

This tool permits to simulate various kind of electromagnetic problems such as

- the 2D scalar problem of finding the eigenmodes inside an hollow waveguide shielded by a perfect conductor
- the 2D vector problem of finding the dispersion diagram of the modes inside an inhomogeneous waveguide shielded by a perfect conductor.
- the 3D vector problem of finding the resonant modes inside an inhomogeneous cavity shielded by a perfect conductor.

The VMM has been proposed and then generalized step by step to handle all these cases showing every time the ability to calculate an high number of modes with a relatively low number of unknowns.

In Chap.4 an authomatic refinement technique has been adopted that permits to improve the accuracy of the solution by increasing the number of the CPs without effects on the conditioning of the problem.

All the theory has been validated through various examples by comparing the results of the VMM with the theory when possible or with HFSS in the other cases.

In Chap. 5 the VMM has been used in conjunction with the mode matching technique. This is useful in the optimization process when a re-simulation of the whole structure could be too much time consuming.

Possible extensions of the VMM are:

- calculating the scattering parameters S also in the case in which a connection port is considered on the boundary of a 3D cavity. This would permit the simulation of more general microwave circuits (e.g. not in line circuits),
- considering more general boundary conditions (e.g. absorbing or resistive boundary conditions).

The presented manuscript is based on the published works listed in Appendix A.

Appendix A

Publications

In the following an updated list of the publications achieved during this PhD activity together with the honors & awards received is given.

A.1 Journals

[J1] V. Lombardi, M. Bozzi, and L. Perregrini, "An improved meshless method for waveguide eigenvalue problems," *IEEE Microw. Compon. Lett.*, Vol. 27, No. 12, pp. 1047-1049, Dec. 2017

[J2] V. Lombardi, M. Bozzi, and L. Perregrini, "A novel variational meshless method with radial basis functions for waveguide eigenvalue problems," *IEEE Trans. Microw. Theory Techn.*, Vol. 66, No. 8, pp. 3714-3723, Aug. 2018.

[J3] V. Lombardi, M. Bozzi and L. Perregrini, "Evaluation of the Dispersion Diagram of Inhomogeneous Waveguides by the Variational Meshless Method ," *IEEE Trans. Microw. Theory Techn*, vol. 67, no. 6, pp. 2105-2113, Jun. 2019.

[J4] V. Lombardi, M. Bozzi, and L. Perregrini, "Mode Matching Analysis of Waveguide Components Exploiting the Variational Meshless Method," *IEEE Microw. Compon. Lett.*, Vol. 29, No. 10, pp. 631-633, Oct. 2019

[J5] V. Lombardi, M. Bozzi, and L. Perregrini, "Exploiting Symmetries in the Variational Meshless Method for 3D Inhomogeneous Cavities," *IEEE Trans. Microw. Theory Techn* , (ACCEPTED)

A.2 Conferences

[C1] V. Lombardi, M. Bozzi, and L. Perregrini, "Meshless Methods applied to Electromagnetic Eigenproblems," *2018 XXXII riunione Nazionale di Elettromagnetismo(RINEM)*, Cagliari, 2018, pp. 1-4.

[C2] V. Lombardi, M. Bozzi, and L. Perregrini, "Analysis of Inhomogeneous Rectangular Waveguides by the Variational Meshless Method," *48th European Microwave Conference (EuMC2018)*, Madrid, Spain, 23-28 Sep. 2018.

[C3] V. Lombardi, M. Bozzi, and L. Perregrini, "Vector Formulation of the Meshless Variational Method for Inhomogeneous Rectangular Waveguides," *2018 IEEE MTT-S International Conference on Numerical Electromagnetic and Multiphysics Modeling and Optimization (NEMO)*, Reykjavik, 2018, pp. 1-3.

[C4] V. Lombardi, M. Bozzi, and L. Perregrini, "Analysis of Dielectric Waveguides With the Variational Meshless Method," *1th European Microwave Conference (EuMCE2019)*, Prague, Czech Rep., 13-15 May 2019.

[C5] V. Lombardi, M. Bozzi, and L. Perregrini, "Exploitation of Electric/Magnetic Wall Boundary Conditions in the Variational Meshless Methods," *2019 IEEE MTT-S International Conference on Numerical Electromagnetic and Multiphysics Modeling and Optimization (NEMO)*, Boston, 29-31 May 2019.

[C6] V. Lombardi, M. Bozzi, L. Perregrini, "The Variational Meshless Method: Theory and Applications," *2019 GTTi-SIEm Conference*, Pavia, 2019, pp. 1-4.

[C7] V. Lombardi, M. Bozzi, and L. Perregrini, "Variational Meshless Method: Exploiting the RBFs in Electromagnetic Problems," *2019 Dolomites Research Week on Approximation 2019 (DRWA19)*, Canazei, Sep. 2019.

[C8] V. Lombardi, M. Bozzi, and L. Perregrini, "Analysis of Inhomogeneous Rectangular Cavities Using the Variational Meshless Method," *48th European Microwave Conference (EuMC2019)*, Paris, France, 29 Sep.-4 Oct. 2019.

[C9] L. Perregrini, V. Lombardi, and M. Bozzi, "The Variational Meshless Method: an Overview of the Theory and Applications," *2019 IEEE Asia-Pacific Microwave Conference (APMC) (invited)*, Singapore, Singapore, 10-13 Dec. 2019.

A.3 Honors & Awards

[H1] Chair of the oral session: "Advanced Numerical Techniques for Microwave Circuits ans Scattering Problems," *1th European Microwave Conference (EuMCE2019)*, Prague, Czech Rep., 13-15 May 2019.

[H2] Young Scientists Contest Sponsored by GAAS - FIRST PRIZE honor issuer: *1th European Microwave Conference (EuMCE2019)*, Prague, Czech Rep., 13-15 May 2019.

[H3] BEST WORK FROM A PHD STUDENT - honor issuer: *SIEM Conference*, Pavia, 26-28 June 2019.

Acknowledgements

Nei ringraziamenti di una Tesi, le prime righe sono solitamente dedicate ai Professori che ti hanno seguito. Nel mio caso questo assume un significato particolare. Molti, infatti, conoscendo le tappe professionali della mia vita, potrebbero esser spinti da curiosità a rivolgermi la seguente domanda "Cosa ti è saltato in mente quando hai deciso di fare un Dottorato a 33 anni?!?!". Lasciatemi dire che, a volte, la vita delle persone prende un cammino diverso da quello che avrebbero intrapreso. Poter tornare indietro è un lusso che non sempre ci si può permettere. Perchè ciò avvenga, è necessario incontrare le persone giuste che credono in te al punto da stimolarti a rimetterti in gioco anche quando questo appare singolare... *persone verso le quali sempre proverai un senso di gratitudine (non formale, ma sostanziale) e che legherai per questo ad alcuni dei ricordi piú intensi e vivi della tua esistenza.*

- Grazie Luca per tutto e per le bellissime serate passate a scrivere gli articoli con passione e dedizione!

- Grazie Maurizio!

Ovviamente ringrazio la donna paziente che a pochi mesi dal diventare madre si è sentita dire "Dolcezza, e se provassi a fare il Dottorato?". Lei mi ha dato tutto il supporto di cui avevo bisogno e con lei ho condiviso e sto condividendo le due gioie piú belle della mia vita.

- Grazie Angela!

Ringrazio i miei genitori, mia sorella, Gigi ed Elio per aver creduto in me e/o contribuito in maniera indiretta a questo risultato.

- Grazie!

Ringrazio tutti i dottorandi del laboratorio di Microonde e Marco che hanno condiviso con me le giornate e i pranzi durante questi tre anni.

- Grazie Ragazzi!